



Fermi National Accelerator Laboratory

FERMILAB-PUB-90/75-T

MAD/PH/562

April 1990

*Z Boson Pair Production via Vector Boson Scattering and
the Search for the Higgs Boson at Hadron Supercolliders*

U. Baur

Physics Department, University of Wisconsin

Madison, WI 53706, USA

and

E. W. N. Glover

Fermi National Accelerator Laboratory

P. O. Box 500, Batavia, IL 60510, USA



ABSTRACT

We present the results of a complete perturbative calculation of Z boson pair production via the $\mathcal{O}(\alpha_W^4)$ electroweak process, $qq \rightarrow qqZZ$, and the $\mathcal{O}(\alpha_s^2\alpha_W^2)$ mixed QCD-electroweak processes, $gg \rightarrow q\bar{q}ZZ$, $qg \rightarrow qgZZ$, $q\bar{q} \rightarrow ggZZ$ and $qq \rightarrow qqZZ$ at supercollider energies. Compact analytic expressions for the helicity amplitudes for all contributing diagrams, including the subsequent decay of the Z boson into massless fermions and all interference effects, are given. Detailed results for the event characteristics and the jet activity in electroweak $qq \rightarrow qqZZ$ events are presented for the full range of invariant masses of the Z pair, m_{ZZ} , as well as in the Higgs boson resonance region, $m_{ZZ} = m_H \pm \Gamma_H$, where we compare the results of the exact calculation with the effective W approximation, and the approximation where only s -channel Higgs resonance diagrams are taken into account. We also compute the background resulting from the mixed QCD-electroweak $ZZ + 2$ jet processes at large jet transverse momenta in the resonance region and suggest techniques to suppress this background. Cross sections for Higgs boson production in the ZZ channel and the continuum ZZ background, in association with up to 2 jets, are given. We find that jet identification in the forward rapidity region, $|\eta_j| > 2.5$, may considerably facilitate the detection of a heavy Higgs Boson with $m_H \sim \mathcal{O}(1 \text{ TeV})$ at the LHC and SSC.

1. Introduction

The standard model of electroweak interactions (SM) predicts the existence of a neutral Higgs scalar of unspecified mass. The discovery of the Higgs boson would provide a crucial test for the SM and the search for it is therefore an important goal for experiments at present and future accelerators. Current data from LEP experiments¹⁾ and low energy experiments²⁾ exclude a Higgs boson with mass $m_H < \mathcal{O}(24 \text{ GeV})$.

Search strategies depend on the mass of the Higgs boson. Experiments at LEP will ultimately be sensitive to Higgs boson masses up to $\mathcal{O}(50 \text{ GeV})$ in $Z \rightarrow H\mu^+\mu^-$.³⁾ At LEP200 one can search for a Higgs boson with $m_H \lesssim 80 \text{ GeV}$ via the process $e^+e^- \rightarrow ZH$.⁴⁾ For larger values of m_H , it is proposed to search for the Higgs boson at hadron supercolliders such as the LHC (pp collisions at $\sqrt{s} = 16 \text{ TeV}$) or the SSC (pp collisions at $\sqrt{s} = 40 \text{ TeV}$). In the region $m_H < 2M_Z$, where M_Z is the Z boson mass, the $H \rightarrow b\bar{b}$ signal is overwhelmed by the QCD background at hadron colliders and only rare decays, such as $H \rightarrow \gamma\gamma$ or $H \rightarrow Z\gamma$,⁵⁾ offer some hope to discover the Higgs boson in this mass range. If $m_H > 2M_Z$, the dominant decay modes are $H \rightarrow ZZ$, $H \rightarrow W^+W^-$ and $H \rightarrow t\bar{t}$. The $t\bar{t}$ and W^+W^- final states are again plagued by large backgrounds, however, the “gold plated” decay mode $H \rightarrow ZZ \rightarrow \ell^+\ell^-\ell'^+\ell'^-$ ($\ell, \ell' = e, \mu$) offers a good chance to find the Higgs boson.

The dominant production mechanism for Higgs bosons in the ZZ channel at hadron colliders are gluon fusion,^{6–8)}

$$gg \rightarrow H \rightarrow ZZ, \quad (1.1)$$

where the gluons couple through a top quark loop to the Higgs boson, and vector boson fusion,^{9,10)}

$$qq \rightarrow qqH \rightarrow qqZZ, \quad (1.2)$$

where the initial quarks (or antiquarks) each radiate a W or Z boson which then annihilate to produce a Higgs boson. The two processes are topologically different,

since, in lowest order, the Higgs bosons produced from gluon fusion have small transverse momentum, p_T , while those from vector boson fusion have $p_T \sim \mathcal{O}(M_W)$ balanced by two small angle jets. The cross section of the gluon fusion process (1.1) depends strongly on the unknown top quark mass, m_t , which, according to present data, must be larger than about 80 GeV.¹¹⁾ For $m_t > 80$ GeV the gluon fusion process dominates for $m_H \lesssim 500$ GeV at the SSC, while, for larger values of m_H , the vector boson fusion process (1.2) becomes a potentially important source for Higgs bosons.

It is clear that if this process is to provide a probe for the Higgs sector of the SM, the predictions for its cross section and all contributing backgrounds must be as accurate as possible. So far, most calculations of Higgs boson production via vector boson fusion (1.2) have relied on one or more approximations. For example, the effective W approximation,⁹⁾ which is analogous to the Weizsäcker-Williams approximation used for photon-photon scattering. In this approximation, the vector bosons radiated from the initial state quarks are treated as on-shell “partons”, while the quarks scatter at very small angles. The approximation neglects the finite p_T of the scattered quarks and of the Higgs boson which, in general, is not small. Important quantities characterizing events resulting from Higgs boson production via vector boson fusion, such as the transverse momentum and the rapidity of the jets or the p_T of the final state Z pair, cannot be calculated in the framework of the effective W approximation.

A second common approximation is to retain only the s -channel Higgs pole diagram calculated in the unitary gauge.^{12–16)} The matrix element for this diagram can easily be calculated and a full study of the characteristics of Higgs boson events can be carried out.^{12–14)} However, this approximation is only valid in the idealized case where the Higgs boson can be treated as a stable on-shell particle. Since the Higgs width, Γ_H , grows like m_H^3/M_W^2 for $m_H > 2M_W$, this is only the case for relatively light Higgs bosons where production via gluon fusion is far more important than vector boson fusion. For heavy Higgs bosons off-shell effects become progressively more and more important. Furthermore, the Higgs pole diagram alone exhibits a ‘bad’ high energy behaviour, eventually violating unitarity, and seriously overestimates the cross section at large m_{ZZ} . Good high energy behaviour

is only restored in a complete calculation of $qq \rightarrow qqZZ$, including all non-resonant diagrams which lead to the same final state.¹⁷⁾

The two small angle jets in $qq \rightarrow qqH \rightarrow qqZZ$ may in fact be helpful in identifying Higgs boson events.^{12,13)} If these jets are detected, $ZZjj$ production via mixed QCD-electroweak processes constitutes an irreducible physics background which needs to be understood if one wants to tag the jets in Higgs bosons events at hadron supercolliders. Although the matrix elements for $ZZjj$ production in hadronic collisions have recently been calculated,¹⁸⁾ no comparison with Higgs boson production via vector boson fusion has been performed.

In this paper, we present detailed results of a complete perturbative calculation of the process (1.2), including all non-resonant diagrams which lead to a $qqZZ$ final state, and of the mixed QCD-electroweak background processes,

$$gg \rightarrow q\bar{q}ZZ, \quad qg \rightarrow qqZZ, \quad q\bar{q} \rightarrow ggZZ, \quad (1.3)$$

and,

$$qq \rightarrow qqZZ. \quad (1.4)$$

Using helicity amplitude techniques, we present analytic expressions for the matrix elements of (1.2) – (1.4), including the decay of the Z bosons into massless fermion-antifermion final states (Section 2). Our matrix elements are therefore especially convenient when properties of, and correlations amongst, final state decay products are of interest.

We then apply the matrix elements to a detailed study of the process (1.2) (Section 3). Results are presented for ZZ pair and individual Z boson distributions, and for quantities characterizing the jet activity in $qq \rightarrow qqH \rightarrow qqZZ$ events. In particular, we shall study the contribution of the non-resonant diagrams to these quantities. We shall also perform a comparison with the effective W approximation (wherever possible), and the s -channel Higgs pole approximation. Numerical results of a calculation of the ZZ invariant mass spectrum including the minimal set of non-resonant $qq \rightarrow qqZZ$ diagrams required for gauge invariance have been reported in Ref. 19. Effects resulting from photon exchange graphs and from the interference

between W and Z or γ exchange graphs have been neglected there. Our calculation contains all diagrams contributing to (1.2).

In Section 4, we compute the background to $pp \rightarrow ZZjj$ resulting from the mixed QCD-electroweak processes in the large jet p_T region and suggest techniques to suppress this background. Interference effects between the $qq \rightarrow qqH \rightarrow qqZZ$ matrix elements and the amplitudes for the processes listed in (1.3) and (1.4) are fully incorporated in our calculation. We also give the cross sections for Higgs boson production in the $H \rightarrow ZZ$ channel and the continuum ZZ background, in association with up to 2 jets, and comment on possible backgrounds arising from double parton scattering and event pile-up. We find that jet identification in the forward rapidity region, $|\eta_j| > 2.5$, may considerably facilitate the detection of a heavy Higgs boson with $m_H \sim \mathcal{O}(1 \text{ TeV})$ at hadron supercolliders. Finally, in Section 5, we shall summarize our results.

2. Matrix Elements

In this section, we present the helicity amplitudes for the production of Z boson pairs accompanied by two jets. There are only two independent subprocesses,

$$qq \rightarrow qqZZ, \tag{2.1}$$

and,

$$gg \rightarrow q\bar{q}ZZ. \tag{2.2}$$

All other subprocesses, *e.g.* $q\bar{q} \rightarrow q\bar{q}ZZ$, $qg \rightarrow qgZZ$ etc., are related to these by crossing symmetry. The four quark subprocess (2.1) receives contributions from W , Z , γ and gluon exchange leading to as many as 126 Feynman diagrams in the unitary gauge for the scattering of identical quarks, while 30 diagrams contribute to the gluon induced process (2.2). To compute the full matrix elements squared directly is a formidable task, and, since the number of contributing Feynman diagrams depends on the flavours of the quarks involved, is not one to be recommended. A more efficient approach is to use spinor techniques to compute helicity amplitudes

for each Feynman diagram which may then be numerically summed and squared to obtain the full squared matrix elements. This is particularly convenient since helicity amplitudes for many Feynman diagrams may be obtained by permutations of only a few basic functions. Furthermore, all interference effects are automatically evaluated.

To compute the helicity amplitudes, we use the improved CALKUL method of Ref. 20 in which all matrix elements are expressed in terms of the spinor products,

$$s_{ij} = \bar{u}_+(p_i)u_-(p_j) = -s_{ji}, \quad (2.3)$$

and,

$$t_{ij} = \bar{u}_-(p_i)u_+(p_j) = s_{ji}^*. \quad (2.4)$$

Here $u_{\pm}(p_i)$ denotes the positive (negative)-helicity spinor of a massless fermion with momentum p_i . Because the fermions are taken to be massless, u -spinors and v -spinors are identical. Since we are interested in the numerical evaluation of helicity amplitudes, an explicit form of s_{ij} is needed. A convenient choice is,²⁰⁾

$$s_{ij} = (p_i^y + ip_i^z)\sqrt{\frac{p_j^0 - p_j^x}{p_i^0 - p_i^x}} - (p_j^y + ip_j^z)\sqrt{\frac{p_i^0 - p_i^x}{p_j^0 - p_j^x}}, \quad (2.5)$$

where,

$$p_i^\mu = (p_i^0, p_i^x, p_i^y, p_i^z),$$

and similarly for p_j^μ . The connection with the usual dot product notation is made by taking the absolute square of s_{ij} ,

$$|s_{ij}|^2 = 2 p_i \cdot p_j. \quad (2.6)$$

The polarisation vector for massless spin-1 bosons is given by,

$$\epsilon_\lambda^\mu = N_k \bar{u}_\lambda(k)\gamma^\mu u_\lambda(q), \quad (2.7)$$

with,

$$N_k = \frac{1}{\sqrt{4k \cdot q}}, \quad (2.8)$$

and where k^μ is the vector boson momentum and λ its helicity. The auxiliary vec-

tor, q^μ , is any lightlike vector which is not collinear to k^μ . Different choices for q^μ are related to each other by gauge transformations on the vector boson polarisation vector. Specific choices for q^μ can lead to somewhat simpler expressions, however, leaving the choice of q^μ free has two advantages. Firstly, it leads to a greater permutation symmetry in the basic helicity amplitudes, and secondly, it provides an additional numerical check: the helicity amplitudes should be invariant under different choices of q^μ . Finally, in this method, massive vector bosons automatically decay into massless fermion-antifermion pairs, further increasing permutation symmetry and allowing the properties of final state particles to be studied.

The generic process we are interested in is,

$$f_1(p_1, i_1, \lambda_1) + f_2(p_2, i_2, \lambda_2) \rightarrow f_3(p_3, i_3, \lambda_3) + f_4(p_4, i_4, \lambda_4) + Z_1 + Z_2, \quad (2.9)$$

followed by,

$$Z_1 \rightarrow \bar{f}_a(p_a, i_a, \lambda_a) + f_b(p_b, i_b, \lambda_b), \quad (2.10)$$

and,

$$Z_2 \rightarrow \bar{f}_c(p_c, i_c, \lambda_c) + f_d(p_d, i_d, \lambda_d). \quad (2.11)$$

Here $f_i(p_i, i_i, \lambda_i)$ represents a massless parton of type (flavour) f_i , with momentum p_i , colour i_i and helicity λ_i . For convenience, we define all momenta to be outgoing,

$$\sum_{i=1,2,3,4,a,b,c,d} b_i p_i = 0, \quad (2.12)$$

where

$$b_i = \begin{cases} +1 & \text{if } p_i \text{ is outgoing,} \\ -1 & \text{if } p_i \text{ is incoming.} \end{cases} \quad (2.13)$$

By including the coefficients b_i in the helicity amplitudes, all possible crossings are automatically accounted for.

2.1 $qq \rightarrow qqZZ$ AMPLITUDES

We start with the helicity amplitudes for the four quark process (2.1). The six topologically distinct Feynman diagrams that contribute are shown in Fig. 1. All other contributing diagrams can be obtained from Fig. 1 either by permutations of momenta or by different choices for the exchanged vector bosons V_i .

The squared matrix elements for the scattering of distinguishable quarks is given by,

$$\left| \mathcal{M}^{f_1 f_2 f_3 f_4}(1, 2, 3, 4) \right|^2 = \left| D_{ab}^Z \right|^2 \left| D_{cd}^Z \right|^2 \sum_{\lambda_i = \pm} \left| \mathcal{M}_{\lambda_1 \lambda_2 \lambda_3 \lambda_4 \lambda_a \lambda_c}^{f_1 f_2 f_3 f_4}(1, 2, 3, 4) \right|^2, \quad (2.14)$$

while that for the scattering of identical quarks is,

$$\begin{aligned} \left| \mathcal{M}^{f_1 f_1 f_1 f_1}(1, 2, 3, 4) \right|^2 &= \left| D_{ab}^Z \right|^2 \left| D_{cd}^Z \right|^2 \times \\ &\sum_{\lambda_i = \pm} \left| \mathcal{M}_{\lambda_1 \lambda_2 \lambda_3 \lambda_4 \lambda_a \lambda_c}^{f_1 f_1 f_1 f_1}(1, 2, 3, 4) - \mathcal{M}_{\lambda_1 \lambda_2 \lambda_4 \lambda_3 \lambda_a \lambda_c}^{f_1 f_1 f_1 f_1}(1, 2, 4, 3) \right|^2. \end{aligned} \quad (2.15)$$

The vector boson propagator for boson V with mass M_V and width Γ_V is,

$$D_{ij}^V = \frac{1}{(b_i p_i + b_j p_j)^2 - M_V^2 + i\Gamma_V M_V}. \quad (2.16)$$

When considering the production of on-shell Z bosons, the full width should be set equal to the partial width for the $Z \rightarrow \bar{a}b$ and $Z \rightarrow \bar{c}d$ decays, so that the full width is saturated and therefore gives the cross section for Z boson production multiplied by unit branching ratio. The full helicity amplitude is obtained by summing the subamplitudes over both the exchanged vector bosons V_i and the diagram topologies i ,

$$\mathcal{M}_{\lambda_1 \lambda_2 \lambda_3 \lambda_4 \lambda_a \lambda_c}^{f_1 f_2 f_3 f_4}(1, 2, 3, 4) = \delta_{\lambda_1 \lambda_3} \delta_{\lambda_2 \lambda_4} \mathcal{M}_{\lambda_1 \lambda_2 \lambda_a \lambda_c}^{f_1 f_2 f_3 f_4}(1, 2, 3, 4), \quad (2.17)$$

with

$$\mathcal{M}_{\lambda_1 \lambda_2 \lambda_a \lambda_c}^{f_1 f_2 f_3 f_4}(1, 2, 3, 4) = \sum_{V_i} \mathcal{M}_{\lambda_1 \lambda_2 \lambda_a \lambda_c}^{V_i}(1, 2, 3, 4), \quad (2.18)$$

and

$$\mathcal{M}_{\lambda_1 \lambda_2 \lambda_a \lambda_c}^{V_i}(1, 2, 3, 4) = \sum_i \mathcal{M}_{\lambda_1 \lambda_2 \lambda_a \lambda_c}^{iV_i}(1, 2, 3, 4) . \quad (2.19)$$

Later, we shall be more explicit as to how to perform these process dependent sums, however, for the moment, we shall proceed directly to the definition of the subamplitudes.

The subamplitude for the sum of all twelve diagrams of the type of Fig. 1a for the exchange of a given vector boson, V , where $V = \gamma, Z, W$ or g , is,

$$\begin{aligned} \mathcal{M}_{\lambda_1 \lambda_2 \lambda_a \lambda_c}^{1V}(1, 2, 3, 4) = & D_{13}^V \sum_{\{1, a, c\}} \mathcal{C}_{\lambda_2; \lambda_1 \lambda_a \lambda_c}^{1V}(f_i, f_j) \mathcal{A}_{\lambda_2; \lambda_1 \lambda_a \lambda_c}^1(2; 1, a, c) \\ & + D_{24}^V \sum_{\{2, a, c\}} \mathcal{C}_{\lambda_1; \lambda_2 \lambda_a \lambda_c}^{1V}(f_i, f_j) \mathcal{A}_{\lambda_1; \lambda_2 \lambda_a \lambda_c}^1(1; 2, a, c) . \end{aligned} \quad (2.20)$$

The coupling function $\mathcal{C}_{\lambda_2; \lambda_1 \lambda_a \lambda_c}^{1V}$ contains all coupling and other vector boson dependent factors, while all of the spinor product information is stored in the basic helicity subamplitude $\mathcal{A}_{\lambda_2; \lambda_1 \lambda_a \lambda_c}^1$. The six permutations, $\{1, a, c\}$, correspond to the quark, f_2 , emitting V , Z_1 and Z_2 in a different sequence. For example, the order $Z_1 V Z_2$ is obtained by the exchanges,

$$\lambda_1 \leftrightarrow \lambda_a, \quad (1 \leftrightarrow a) \quad \text{and} \quad (3 \leftrightarrow b),$$

where $(x \leftrightarrow y)$ implies $b_x \leftrightarrow b_y$, $p_x \leftrightarrow p_y$ and $f_x \leftrightarrow f_y$. Similarly, the second set of six permutations is obtained by the exchanges,

$$\lambda_1 \leftrightarrow \lambda_2, \quad (1 \leftrightarrow 2) \quad \text{and} \quad (3 \leftrightarrow 4).$$

The coupling function is,

$$\mathcal{C}_{\lambda_2; \lambda_1 \lambda_a \lambda_c}^{1V}(f_i, f_j) = c_{\lambda_a}^{Zf_a} c_{\lambda_c}^{Zf_c} c_{\lambda_1}^{Vf_1} c_{\lambda_2}^{Vf_2} c_{\lambda_2}^{Zf_i} c_{\lambda_2}^{Zf_j} , \quad (2.21)$$

where c_{λ}^{Vf} is the λ -handed coupling of fermion f with the vector boson V . In the standard model, the couplings of a fermion with electric charge q_f and weak isospin

T_3^f are given by,

$$\begin{aligned}
c_-^{\gamma f} &= c_+^{\gamma f} = eq_f, \\
c_-^{Zf} &= g_Z(T_3^f - q_f \sin^2 \theta_W); \quad c_+^{Zf} = -g_Z q_f \sin^2 \theta_W, \\
c_-^{Wf} &= \frac{1}{\sqrt{2}} g_W; \quad c_+^{Wf} = 0,
\end{aligned} \tag{2.22}$$

where θ_W is the Weinberg angle. Furthermore, if the fermion is coloured,

$$c_-^{gf} = c_+^{gf} = g_s. \tag{2.23}$$

The coupling constants are defined by,

$$\begin{aligned}
e^2 &= 4\pi\alpha, \\
g_s^2 &= 4\pi\alpha_s,
\end{aligned} \tag{2.24}$$

evaluated at the appropriate scale Q^2 and

$$\begin{aligned}
g_W &= \frac{e}{\sin \theta_W}, \\
g_Z &= \frac{g_W}{\cos \theta_W}.
\end{aligned} \tag{2.25}$$

When the exchanged vector boson V is flavour changing, the fermion flavours f_i and f_j are determined by the order of emission of the vector bosons from f_2 . For example, in Fig. 1a, $f_2 \neq f_i = f_j = f_4$ for W exchange, while, in the case of photon, Z or gluon exchange, $f_2 = f_i = f_j = f_4$.

All of the basic helicity subamplitudes for this diagram may be obtained from one function,

$$\mathcal{A}_{+;+++}^1(2; 1, a, c) = 8P_{123}P_{4cd} s_{4d}s_{21}^* \langle b|4+d|c \rangle \langle 3|1+2|a \rangle, \tag{2.26}$$

where P_{ijk} is the fermion propagator carrying momentum $b_i p_i + b_j p_j + b_k p_k$,

$$P_{ijk} = \frac{1}{(b_i p_i + b_j p_j + b_k p_k)^2}. \tag{2.27}$$

Furthermore, we have used the notation,

$$\begin{aligned}
\langle i|j+k|l\rangle &= \bar{u}_+(p_i)(b_j \not{p}_j + b_k \not{p}_k) u_+(p_l) \\
&= b_j s_{ji} s_{jl}^* + b_k s_{ki} s_{kl}^* \\
&= \langle l|j+k|i\rangle^* .
\end{aligned} \tag{2.28}$$

Since the decay current, $\bar{u}_{\lambda_i}(p_i)\gamma^\mu u_{\lambda_i}(p_j) = \bar{u}_{-\lambda_i}(p_j)\gamma^\mu u_{-\lambda_i}(p_i)$, exchanging p_i, p_j is equivalent to reversing helicity λ_i , so that the subamplitudes with λ_1, λ_a or λ_c negative are given by simple permutations of momenta,

$$\mathcal{A}_{\lambda_2; -\lambda_1 \lambda_a \lambda_c}^1(2; 1, a, c) = \mathcal{A}_{\lambda_2; \lambda_1 \lambda_a \lambda_c}^1(2; 3, a, c) , \tag{2.29a}$$

$$\mathcal{A}_{\lambda_2; \lambda_1 -\lambda_a \lambda_c}^1(2; 1, a, c) = \mathcal{A}_{\lambda_2; \lambda_1 \lambda_a \lambda_c}^1(2; 1, b, c) , \tag{2.29b}$$

and,

$$\mathcal{A}_{\lambda_2; \lambda_1 \lambda_a -\lambda_c}^1(2; 1, a, c) = \mathcal{A}_{\lambda_2; \lambda_1 \lambda_a \lambda_c}^1(2; 1, a, d) , \tag{2.29c}$$

where, for example, $\mathcal{A}_{\lambda_2; \lambda_1 \lambda_a \lambda_c}^1(2; 3, a, c)$ is obtained from $\mathcal{A}_{\lambda_2; \lambda_1 \lambda_a \lambda_c}^1(2; 1, a, c)$ by the exchange $(1 \leftrightarrow 3)$. Finally, the subamplitudes with λ_2 negative are obtained through the parity relation,

$$\mathcal{A}_{-\lambda_2; -\lambda_1 -\lambda_a -\lambda_c}^1(2; 1, a, c) = \mathcal{A}_{\lambda_2; \lambda_1 \lambda_a \lambda_c}^{1*}(2; 1, a, c) . \tag{2.30}$$

This diagram topology, which contributes as many as 84 times (W, Z, γ and gluon exchange and identical quarks), is thus reduced to the numerical evaluation of one complex function with permuted arguments, weighted according the coupling strengths of the exchanged bosons.

Similarly, the subamplitudes for the eight diagrams with the topology shown in Fig. 1b where $V = \gamma, Z, W$ or g , are given by,

$$\mathcal{M}_{\lambda_1 \lambda_2 \lambda_a \lambda_c}^{2V}(1, 2, 3, 4) = D_{13ab}^V \widetilde{\mathcal{M}}_{\lambda_1 \lambda_2 \lambda_a \lambda_c}^{2V}(1, 2, 3, 4) + D_{24ab}^V \widetilde{\mathcal{M}}_{\lambda_2 \lambda_1 \lambda_a \lambda_c}^{2V}(2, 1, 4, 3) \tag{2.31}$$

where D_{ijkl}^V is a straightforward generalisation of Eq. (2.16) and,

$$\begin{aligned}
\widetilde{\mathcal{M}}_{\lambda_1 \lambda_2 \lambda_a \lambda_c}^{2V}(1, 2, 3, 4) = & \mathcal{C}_{\lambda_2 \lambda_1; \lambda_a \lambda_c}^{2V}(f_4, f_3) \mathcal{A}_{\lambda_2 \lambda_1; \lambda_a \lambda_c}^2(2; 1, a, c) \\
& - \mathcal{C}_{\lambda_2 \lambda_1; \lambda_a \lambda_c}^{2V}(f_4, f_1) \mathcal{A}_{\lambda_2 - \lambda_1; \lambda_a \lambda_c}^2(2; 3, a, c) \\
& - \mathcal{C}_{\lambda_2 \lambda_1; \lambda_a \lambda_c}^{2V}(f_2, f_3) \mathcal{A}_{-\lambda_2 \lambda_1; \lambda_a \lambda_c}^2(4; 1, a, c) \\
& + \mathcal{C}_{\lambda_2 \lambda_1; \lambda_a \lambda_c}^{2V}(f_2, f_1) \mathcal{A}_{-\lambda_2 - \lambda_1; \lambda_a \lambda_c}^2(4; 3, a, c) .
\end{aligned} \tag{2.32}$$

The coupling function for Fig. 1b is,

$$\mathcal{C}_{\lambda_2; \lambda_1 \lambda_a \lambda_c}^{2V}(f_i, f_j) = c_{\lambda_a}^{Z f_a} c_{\lambda_c}^{Z f_c} c_{\lambda_1}^{V f_1} c_{\lambda_2}^{V f_2} c_{\lambda_1}^{Z f_i} c_{\lambda_2}^{Z f_j} . \tag{2.33}$$

In this case, there are two independent basic helicity subamplitudes,

$$\begin{aligned}
\mathcal{A}_{++; ++}^2(2; 1, a, c) = & 8P_{3ab}P_{4cd} s_{4d}s_{21}^*s_{3b} \left\{ b_4 s_{4c}^* \langle 4|3+b|a \rangle + b_d s_{dc}^* \langle d|3+b|a \rangle \right\} \\
& - \frac{4}{M_V^2} s_{4d}s_{3b}s_{2c}^*s_{1a}^* ,
\end{aligned} \tag{2.34}$$

$$\begin{aligned}
\mathcal{A}_{+-; ++}^2(2; 1, a, c) = & 8P_{3ab}P_{4cd} s_{4d}s_{3a}^* \langle 1|4+d|c \rangle \langle b|3+a|2 \rangle \\
& - \frac{4}{M_V^2} s_{4d}s_{1b}s_{3a}^*s_{2c}^* .
\end{aligned} \tag{2.35}$$

The last term in each of these expressions is generated by the $k^\mu k^\nu / M_V^2$ piece of the V propagator when V is massive, and does not contribute when $V = \gamma, g$. Since the fermions that V couples to are not on-shell, this term does not vanish diagram by diagram. However, for $V = Z$, once the appropriate combination of diagrams of this topology is taken (Eq. (2.32)), these terms do vanish.

The subamplitudes for other helicities are related by the usual line reversal and parity relations,

$$\mathcal{A}_{\lambda_2 \lambda_1; -\lambda_a \lambda_c}^2(2; 1, a, c) = \mathcal{A}_{\lambda_2 \lambda_1; \lambda_a \lambda_c}^2(2; 1, b, c) , \tag{2.36a}$$

$$\mathcal{A}_{\lambda_2 \lambda_1; \lambda_a - \lambda_c}^2(2; 1, a, c) = \mathcal{A}_{\lambda_2 \lambda_1; \lambda_a \lambda_c}^2(2; 1, a, d) , \quad (2.36b)$$

and,

$$\mathcal{A}_{-\lambda_2 - \lambda_1; -\lambda_a - \lambda_c}^2(2; 1, a, c) = \mathcal{A}_{\lambda_2 \lambda_1; \lambda_a \lambda_c}^{2*}(2; 1, a, c) . \quad (2.36c)$$

The Higgs boson contributes to diagrams with the topology shown in Fig. 1c. Depending on the exchanged vector bosons, V_1 and V_2 , where $V_1, V_2 = W, Z$, as many as 3 diagrams may contribute,

$$\mathcal{M}_{\lambda_1 \lambda_2 \lambda_a \lambda_c}^{3V_1 V_2}(1, 2, 3, 4) = D_{13}^{V_1} D_{24}^{V_2} \widetilde{\mathcal{M}}_{\lambda_1 \lambda_2 \lambda_a \lambda_c}^{3V_1 V_2}(1, 2, 3, 4) \quad (2.37)$$

with

$$\begin{aligned} \widetilde{\mathcal{M}}_{\lambda_1 \lambda_2 \lambda_a \lambda_c}^{3V_1 V_2}(1, 2, 3, 4) = & D_{13cd}^H \mathcal{C}_{\lambda_2; \lambda_1 \lambda_a \lambda_c}^{3V_1 V_2}(V_1 Z, V_2 Z) \mathcal{A}_{\lambda_2; \lambda_1 \lambda_a \lambda_c}^3(2; 1, a, c) \\ & + D_{ab13}^H \mathcal{C}_{\lambda_2; \lambda_1 \lambda_a \lambda_c}^{3V_1 V_2}(V_1 Z, V_2 Z) \mathcal{A}_{\lambda_2; \lambda_a \lambda_c \lambda_1}^3(2; a, c, 1) \\ & + D_{cdab}^H \mathcal{C}_{\lambda_2; \lambda_1 \lambda_a \lambda_c}^{3V_1 V_2}(V_1 V_2, Z Z) \mathcal{A}_{\lambda_2; \lambda_c \lambda_1 \lambda_a}^3(2; c, 1, a) . \end{aligned} \quad (2.38)$$

The coupling function depends on the coupling between the Higgs boson and two vector bosons,

$$\mathcal{C}_{\lambda_2; \lambda_1 \lambda_a \lambda_c}^{3V_1 V_2}(V_i V_j, V_k V_l) = c_{\lambda_a}^{Z f_a} c_{\lambda_c}^{Z f_c} c_{\lambda_1}^{V_1 f_1} c_{\lambda_2}^{V_2 f_2} g^{V_i V_j H} g^{V_k V_l H} , \quad (2.39)$$

where

$$g^{V_i V_j H} = \begin{cases} g_Z M_Z & \text{if } V_i = V_j = Z, \\ g_W M_W & \text{if } V_i = V_j = W, \\ 0 & \text{if } V_i \neq V_j. \end{cases} \quad (2.40)$$

There is only one independent basic helicity subamplitude,

$$\mathcal{A}_{+; +++}^3(2; 1, a, c) = 4s_{4b}s_{2a}^*s_{3d}s_{1c}^* , \quad (2.41)$$

from which the subamplitudes with negative helicities are obtained through relations analogous to Eqs. (2.29) and (2.30).

The three topologies discussed so far are the only ones that contribute in the case of γ , Z or gluon exchange. However, when W exchange occurs, three additional topologies containing triple and quartic vector boson couplings also contribute. The subamplitudes for the eight diagrams of the topology shown in Fig. 1d are given by,

$$\mathcal{M}_{\lambda_1 \lambda_2 \lambda_a \lambda_c}^{4V_1 V_2}(1, 2, 3, 4) = \sum_{\{a,c\}} \sum_{\{1,2\}} D_{13}^{V_1} D_{13ab}^{V_2} \widetilde{\mathcal{M}}_{\lambda_1 \lambda_2 \lambda_a \lambda_c}^{4V_1 V_2}(1, 2, 3, 4) \quad (2.42)$$

with

$$\begin{aligned} \widetilde{\mathcal{M}}_{\lambda_1 \lambda_2 \lambda_a \lambda_c}^{4V_1 V_2}(1, 2, 3, 4) = & \mathcal{C}_{\lambda_2; \lambda_1 \lambda_a \lambda_c}^{4V_1 V_2}(f_4) \mathcal{A}_{\lambda_2; \lambda_1 \lambda_a \lambda_c}^4(2; 1, a, c) \\ & - \mathcal{C}_{\lambda_2; \lambda_1 \lambda_a \lambda_c}^{4V_1 V_2}(f_2) \mathcal{A}_{\lambda_2; \lambda_1 \lambda_a \lambda_c}^{4*}(4; 3, b, d). \end{aligned} \quad (2.43)$$

In this case, there is a sum both over the permutations obtained by exchanging the fermion lines containing f_1 and f_2 ,

$$\lambda_1 \leftrightarrow \lambda_2, \quad (1 \leftrightarrow 2) \quad \text{and} \quad (3 \leftrightarrow 4),$$

and over the exchanges of the two Z bosons,

$$\lambda_a \leftrightarrow \lambda_c, \quad (a \leftrightarrow c) \quad \text{and} \quad (b \leftrightarrow d),$$

yielding all eight diagrams. The coupling function depends on the triple vector boson coupling which we write as a difference of two left-handed couplings of fermions with the Z boson (thus specifying the case $V_1 = V_2 = W$),

$$\mathcal{C}_{\lambda_2; \lambda_1 \lambda_a \lambda_c}^{4V_1 V_2}(f_i) = c_{\lambda_a}^{Z f_a} c_{\lambda_c}^{Z f_c} c_{\lambda_1}^{V_1 f_1} c_{\lambda_2}^{V_2 f_2} c_{\lambda_2}^{Z f_i} \left(c_-^{Z f_1} - c_-^{Z f_3} \right). \quad (2.44)$$

Once again, there is only one independent basic helicity subamplitude which is antisymmetric under the exchanges $(1 \leftrightarrow a)$ and $(3 \leftrightarrow b)$ due to the antisymmetric

nature of the triple gauge boson vertex,

$$\mathcal{A}_{+;+++}^4(2; 1, a, c) = \tilde{\mathcal{A}}_{+;+++}^4(1, a) - \tilde{\mathcal{A}}_{+;+++}^4(a, 1) , \quad (2.45)$$

where

$$\begin{aligned} \tilde{\mathcal{A}}_{+;+++}^4(1, a) = & 8P_{4cd}s_{4d}s_{21}^* \langle b|1+3|a \rangle \langle 3|4+d|c \rangle \\ & - 4P_{4cd}s_{4d}s_{3b}s_{1a}^* \{ b_1s_{21}^* \langle 1|4+d|c \rangle + b_3s_{23}^* \langle 3|4+d|c \rangle \} \\ & - \frac{8}{M_V^2} b_1b_3(p_1 \cdot p_3)s_{4d}s_{3b}s_{2c}^*s_{1a}^* . \end{aligned} \quad (2.46)$$

As before, the subamplitudes with negative helicities are easily obtained through relations analogous to Eqs. (2.29) and (2.30).

The triple gauge boson vertex occurs twice in diagrams with the topology shown in Fig. 1e. The two contributing diagrams are obtained by exchanging the two Z bosons, yielding the subamplitude,

$$\mathcal{M}_{\lambda_1\lambda_2\lambda_a\lambda_c}^{5V_1V_2V_3}(1, 2, 3, 4) = D_{13}^{V_1}D_{24}^{V_2} \sum_{\{a,c\}} D_{13cd}^{V_3} \mathcal{C}_{\lambda_2;\lambda_1\lambda_a\lambda_c}^{5V_1V_2V_3} \mathcal{A}_{\lambda_2;\lambda_1\lambda_a\lambda_c}^5(2; 1, a, c) , \quad (2.47)$$

where

$$\mathcal{C}_{\lambda_2;\lambda_1\lambda_a\lambda_c}^{5V_1V_2V_3} = c_{\lambda_a}^{Zf_a} c_{\lambda_c}^{Zf_c} c_{\lambda_1}^{V_1f_1} c_{\lambda_2}^{V_2f_2} g^{V_1V_3Z} g^{V_2V_3Z} . \quad (2.48)$$

The standard model triple gauge boson coupling is given by,

$$g^{V_iV_jZ} = \begin{cases} g_Z \cos^2 \theta_W & \text{if } V_i = V_j = W, \\ 0 & \text{if } V_i \neq V_j. \end{cases} \quad (2.49)$$

As in the diagrams of Fig. 1d, the structure of the triple gauge boson vertex is

manifest in the basic subamplitude,

$$\begin{aligned} \mathcal{A}_{+;+++}^5(2; 1, a, c) = & \tilde{\mathcal{A}}_{+;+++}^5(2, 1, a, c) - \tilde{\mathcal{A}}_{+;+++}^5(a, 1, 2, c) \\ & + \tilde{\mathcal{A}}_{+;+++}^5(1, 2, c, a) - \tilde{\mathcal{A}}_{+;+++}^5(c, 2, 1, a) , \end{aligned} \quad (2.50)$$

where

$$\begin{aligned} \tilde{\mathcal{A}}_{+;+++}^5(2, 1, a, c) = & -8s_{4b}s_{2a}^*\langle d|2+4|c\rangle\langle 3|a+b|1\rangle - 8s_{4d}s_{2c}^*\langle b|2+4|a\rangle\langle 3|c+d|1\rangle \\ & - 4s_{4b}s_{3d}s_{2a}^*s_{1c}^* \left\{ (p_{V_c} \cdot p_{V_2}) + \frac{p_{V_c}^2 p_{V_2}^2}{M_V^2} \right\} . \end{aligned} \quad (2.51)$$

Here, we have also used the obvious notation,

$$p_{V_c} = b_c p_c + b_d p_d, \quad p_{V_2} = b_2 p_2 + b_4 p_4 .$$

Once again, the subamplitudes with negative helicities are easily obtained through relations analogous to Eqs. (2.29) and (2.30).

Finally, the four gauge boson vertex contributes in Fig. 1f,

$$\mathcal{M}_{\lambda_1 \lambda_2 \lambda_a \lambda_c}^{6V_1 V_2}(1, 2, 3, 4) = D_{13}^{V_1} D_{24}^{V_2} \mathcal{C}_{\lambda_2; \lambda_1 \lambda_a \lambda_c}^{6V_1 V_2} \mathcal{A}_{\lambda_2; \lambda_1 \lambda_a \lambda_c}^6(2; 1, a, c) , \quad (2.52)$$

where

$$\mathcal{C}_{\lambda_2; \lambda_1 \lambda_a \lambda_c}^{6V_1 V_2} = c_{\lambda_a}^{Zf_a} c_{\lambda_c}^{Zf_c} c_{\lambda_1}^{V_1 f_1} c_{\lambda_2}^{V_2 f_2} g^{V_1 V_2 Z Z} . \quad (2.53)$$

The standard model quartic gauge boson coupling is given by,

$$g^{V_i V_j Z Z} = \begin{cases} g_W^2 \cos^2 \theta_W & \text{if } V_i = V_j = W, \\ 0 & \text{if } V_i \neq V_j, \end{cases} \quad (2.54)$$

and

$$\mathcal{A}_{+;+++}^6(2; 1, a, c) = 8s_{bd}s_{ac}^*s_{43}s_{21}^* - 4s_{4b}s_{2a}^*s_{3d}s_{1c}^* - 4s_{4d}s_{2c}^*s_{3b}s_{1a}^* . \quad (2.55)$$

The negative helicity subamplitudes are again obtained from the line-reversal and parity relations, Eqs. (2.29) and (2.30).

We can now construct the subamplitudes of (2.19) for the exchange of a vector boson summed over the contributing diagrams. In the case of photon or gluon exchange, $V = \gamma$ or g , only the subamplitudes (2.20) and (2.31) contribute,

$$\mathcal{M}_{\lambda_1 \lambda_2 \lambda_a \lambda_c}^V(1, 2, 3, 4) = \mathcal{M}_{\lambda_1 \lambda_2 \lambda_a \lambda_c}^{1V}(1, 2, 3, 4) + \mathcal{M}_{\lambda_1 \lambda_2 \lambda_a \lambda_c}^{2V}(1, 2, 3, 4) , \quad (2.56)$$

while for Z boson exchange, there is also a contribution from the Higgs boson (2.37),

$$\begin{aligned} \mathcal{M}_{\lambda_1 \lambda_2 \lambda_a \lambda_c}^Z(1, 2, 3, 4) = & \mathcal{M}_{\lambda_1 \lambda_2 \lambda_a \lambda_c}^{1Z}(1, 2, 3, 4) + \mathcal{M}_{\lambda_1 \lambda_2 \lambda_a \lambda_c}^{2Z}(1, 2, 3, 4) \\ & + \mathcal{M}_{\lambda_1 \lambda_2 \lambda_a \lambda_c}^{3ZZ}(1, 2, 3, 4) . \end{aligned} \quad (2.57)$$

All six subamplitudes contribute in the case of W exchange,

$$\begin{aligned} \mathcal{M}_{\lambda_1 \lambda_2 \lambda_a \lambda_c}^W(1, 2, 3, 4) = & \mathcal{M}_{\lambda_1 \lambda_2 \lambda_a \lambda_c}^{1W}(1, 2, 3, 4) + \mathcal{M}_{\lambda_1 \lambda_2 \lambda_a \lambda_c}^{2W}(1, 2, 3, 4) \\ & + \mathcal{M}_{\lambda_1 \lambda_2 \lambda_a \lambda_c}^{3WW}(1, 2, 3, 4) + \mathcal{M}_{\lambda_1 \lambda_2 \lambda_a \lambda_c}^{4WW}(1, 2, 3, 4) \\ & + \mathcal{M}_{\lambda_1 \lambda_2 \lambda_a \lambda_c}^{5WWW}(1, 2, 3, 4) + \mathcal{M}_{\lambda_1 \lambda_2 \lambda_a \lambda_c}^{6WW}(1, 2, 3, 4). \end{aligned} \quad (2.58)$$

Finally, we can build the full helicity amplitude for the scattering of different quark flavour combinations (2.18). First of all, when all four quarks are of different flavour, only W exchange can contribute,

$$\mathcal{M}_{\lambda_1 \lambda_2 \lambda_a \lambda_c}^{f_1 f_2 f_3 f_4}(1, 2, 3, 4) = \delta_{i_1 i_3} \delta_{i_2 i_4} V_{f_1 f_3} V_{f_2 f_4} \mathcal{M}_{\lambda_1 \lambda_2 \lambda_a \lambda_c}^W(1, 2, 3, 4) , \quad (2.59)$$

where $V_{f_i f_j}$ is the KM mixing matrix element for the coupling of the W boson with fermions f_i and f_j . The delta functions on the quark colours make the colour structure explicit.

If there are two flavours of quarks in the process, $f_1 = f_3$ and $f_2 = f_4$, then either colour singlets or octets may be exchanged leading to the following subam-

plitude,

$$\begin{aligned}
\mathcal{M}_{\lambda_1 \lambda_2 \lambda_a \lambda_c}^{f_1 f_2 f_1 f_2}(1, 2, 3, 4) = & \delta_{i_1 i_3} \delta_{i_2 i_4} \mathcal{M}_{\lambda_1 \lambda_2 \lambda_a \lambda_c}^\gamma(1, 2, 3, 4) \\
& + \delta_{i_1 i_3} \delta_{i_2 i_4} \mathcal{M}_{\lambda_1 \lambda_2 \lambda_a \lambda_c}^Z(1, 2, 3, 4) \\
& + T_{i_1 i_3}^a T_{i_2 i_4}^a \mathcal{M}_{\lambda_1 \lambda_2 \lambda_a \lambda_c}^g(1, 2, 3, 4) \\
& - \delta_{i_1 i_4} \delta_{i_2 i_3} V_{f_1 f_2}^2 \mathcal{M}_{\lambda_1 \lambda_2 \lambda_a \lambda_c}^W(1, 2, 4, 3) ,
\end{aligned} \tag{2.60}$$

where $T_{i,i}^a$ is an $SU(3)$ colour matrix. Provided $f_1 \neq f_2$, there is an electroweak-QCD interference between the W and gluon exchange terms, but not between $\gamma(Z)$ and gluon exchange. Furthermore, there is a colour suppressed interference between W and $\gamma(Z)$ exchange.

Finally, when $f_1 = f_2$, there is no contribution from W exchange. In this case, a new electroweak-QCD interference is generated between the gluon exchange of $\mathcal{M}(1, 2, 3, 4)$ and the $\gamma(Z)$ exchange of $\mathcal{M}(1, 2, 4, 3)$ in Eq. (2.15) and vice versa. This can be clearly seen in the full colour interference structure of the squared matrix elements when all four colour structures contribute,

$$\begin{aligned}
|\mathcal{M}|^2 = & |A \delta_{i_1 i_3} \delta_{i_2 i_4} + B \delta_{i_1 i_4} \delta_{i_2 i_3} + C T_{i_1 i_3}^a T_{i_2 i_4}^a + D T_{i_1 i_4}^a T_{i_2 i_3}^a|^2 \\
= & 9|A|^2 + 9|B|^2 + 2|C|^2 + 2|D|^2 \\
& + 3(AB^* + A^*B) - \frac{2}{3}(CD^* + C^*D) + 4(AD^* + A^*D + BC^* + B^*C) .
\end{aligned} \tag{2.61}$$

2.2 $gg \rightarrow q\bar{q}ZZ$ AMPLITUDES

We now turn to the two gluon-two quark process (2.2). In the notation of (2.9), we have,

$$f_1 = g_1, \quad f_2 = g_2, \quad i_1 = a_1, \quad i_2 = a_2 \quad \text{and} \quad f_4 = \bar{f}_3 ,$$

where a_i is a colour index in the adjoint representation. As mentioned earlier, to describe the polarisation vector of massless vector bosons in the improved CALKUL

method, it is necessary to introduce an auxiliary vector. We choose these vectors to be momenta p_i associated with g_1 and p_j associated with g_2 . To maintain permutation symmetry, we also introduce the ‘directions’, b_i and b_j where, since the auxiliary vectors are not physical,

$$b_i = b_j = 0.$$

There are now five pairs of momenta,

$$(p_1, p_i), (p_2, p_j), (p_3, p_4), (p_a, p_b) \text{ and } (p_c, p_d),$$

rather than the four of Section 2.1. In particular, p_3 and p_4 are now paired together rather than with p_1 and p_2 .

The squared matrix elements are given by,

$$|\mathcal{M}^{ggq\bar{q}}(1, 2, 3, 4)|^2 = |N_i|^2 |N_j|^2 |D_{ab}^Z|^2 |D_{cd}^Z|^2 \sum_{\lambda_i = \pm} |\mathcal{M}_{\lambda_1 \lambda_2 \lambda_3 \lambda_4 \lambda_a \lambda_c}^{ggq\bar{q}}(1, 2, 3, 4)|^2. \quad (2.62)$$

N_i and N_j are the normalisations of the vector boson polarisations given in (2.8). The full helicity amplitude can be divided according to the two colour structures,

$$\begin{aligned} \mathcal{M}_{\lambda_1 \lambda_2 \lambda_3 \lambda_4 \lambda_a \lambda_c}^{ggq\bar{q}}(1, 2, 3, 4) = \delta_{\lambda_3 \lambda_4} \Big\{ (T^{a_1} T^{a_2})_{i_3 i_4} \mathcal{M}_{\lambda_1 \lambda_2 \lambda_3 \lambda_a \lambda_c}(1, 2, 3) \\ + (T^{a_2} T^{a_1})_{i_3 i_4} \mathcal{M}_{\lambda_2 \lambda_1 \lambda_3 \lambda_a \lambda_c}(2, 1, 3) \Big\}, \end{aligned} \quad (2.63)$$

so that,

$$\begin{aligned} |\mathcal{M}_{\lambda_1 \lambda_2 \lambda_3 \lambda_4 \lambda_a \lambda_c}^{ggq\bar{q}}(1, 2, 3, 4)|^2 = \frac{16}{3} \Big\{ |\mathcal{M}_{\lambda_1 \lambda_2 \lambda_3 \lambda_a \lambda_c}(1, 2, 3)|^2 + |\mathcal{M}_{\lambda_2 \lambda_1 \lambda_3 \lambda_a \lambda_c}(2, 1, 3)|^2 \Big\} \\ - \frac{2}{3} \Big\{ \mathcal{M}_{\lambda_1 \lambda_2 \lambda_3 \lambda_a \lambda_c}(1, 2, 3) \mathcal{M}_{\lambda_2 \lambda_1 \lambda_3 \lambda_a \lambda_c}^*(2, 1, 3) \\ + \mathcal{M}_{\lambda_1 \lambda_2 \lambda_3 \lambda_a \lambda_c}^*(1, 2, 3) \mathcal{M}_{\lambda_2 \lambda_1 \lambda_3 \lambda_a \lambda_c}(2, 1, 3) \Big\}, \end{aligned} \quad (2.64)$$

and where the subamplitudes are again obtained by summing over the contributing

diagram topologies shown in Fig. 2,

$$\mathcal{M}_{\lambda_1 \lambda_2 \lambda_3 \lambda_a \lambda_c}(1, 2, 3) = C_{\lambda_1 \lambda_2 \lambda_3 \lambda_a \lambda_c} \sum_i \mathcal{M}_{\lambda_1 \lambda_2 \lambda_3 \lambda_a \lambda_c}^i(1, 2, 3) . \quad (2.65)$$

In this case the coupling function is common to all topologies and is given by,

$$C_{\lambda_1 \lambda_2 \lambda_3 \lambda_a \lambda_c} = g_s^2 c_{\lambda_a}^{Zf_a} c_{\lambda_c}^{Zf_c} \left(c_{\lambda_3}^{Zf_3} \right)^2 . \quad (2.66)$$

In all, there are 30 diagrams in the unitary gauge, however, not all of them contribute to each colour structure. Of the 24 diagrams with the topology shown in Fig. 2a, only twelve have the colour structure $(T^{a_1} T^{a_2})_{i_3 i_4}$ so that,

$$\mathcal{M}_{\lambda_1 \lambda_2 \lambda_3 \lambda_a \lambda_c}^1(1, 2, 3) = \sum_{\{1, 2, a, c\}} \mathcal{A}_{\lambda_3; \lambda_1 \lambda_2 \lambda_a \lambda_c}^1(3; 1, 2, a, c) , \quad (2.67)$$

where the sum is over all permutations which maintain the order of 1 and 2. In other words, all diagrams where gluon 1 is emitted from the fermion line before gluon 2. The basic helicity subamplitude for this diagram is,

$$\begin{aligned} \mathcal{A}_{+;++++}^1(3; 1, 2, a, c) &= -16 P_{42j} P_{42jcd} P_{31i} s_{42} s_{3i}^* \\ &\langle d|4+2|j \rangle \langle b|4+2+j+d|c \rangle \langle 1|3+i|a \rangle , \end{aligned} \quad (2.68)$$

where $P_{i\dots j}$ and $\langle i|j+\dots+k|l \rangle$ are straightforward generalisations of (2.27) and (2.28) respectively. The 31 helicity amplitudes with at least one helicity negative are obtained by a combination of line reversal,

$$\mathcal{A}_{\lambda_3; -\lambda_1 \lambda_2 \lambda_a \lambda_c}^1(3; 1, 2, a, c) = \mathcal{A}_{\lambda_3; \lambda_1 \lambda_2 \lambda_a \lambda_c}^1(3; i, 2, a, c) , \quad (2.69a)$$

$$\mathcal{A}_{\lambda_3; \lambda_1 -\lambda_2 \lambda_a \lambda_c}^1(3; 1, 2, a, c) = \mathcal{A}_{\lambda_3; \lambda_1 \lambda_2 \lambda_a \lambda_c}^1(3; 1, j, a, c) , \quad (2.69b)$$

$$\mathcal{A}_{\lambda_3; \lambda_1 \lambda_2 -\lambda_a \lambda_c}^1(3; 1, 2, a, c) = \mathcal{A}_{\lambda_3; \lambda_1 \lambda_2 \lambda_a \lambda_c}^1(3; 1, 2, b, c) , \quad (2.69c)$$

$$\mathcal{A}_{\lambda_3; \lambda_1 \lambda_2 \lambda_a -\lambda_c}^1(3; 1, 2, a, c) = \mathcal{A}_{\lambda_3; \lambda_1 \lambda_2 \lambda_a \lambda_c}^1(3; 1, 2, a, d) , \quad (2.69d)$$

and parity,

$$\mathcal{A}_{-\lambda_3; \lambda_1 \lambda_2 \lambda_a \lambda_c}^1(3; 1, 2, a, c) = \mathcal{A}_{\lambda_3; \lambda_1 \lambda_2 \lambda_a \lambda_c}^{1*}(3; i, j, b, d) . \quad (2.69e)$$

The second topology, shown in Fig. 2b, contributes twice,

$$\mathcal{M}_{\lambda_1 \lambda_2 \lambda_3 \lambda_a \lambda_c}^2(1, 2, 3) = \sum_{\{a, c\}} \mathcal{A}_{\lambda_3; \lambda_1 \lambda_2 \lambda_a \lambda_c}^2(3; 1, 2, a, c) , \quad (2.70)$$

Because of the triple gluon vertex, the basic subamplitude is antisymmetric under exchanges of the two gluons,

$$\mathcal{A}_{\lambda_3; \lambda_1 \lambda_2 \lambda_a \lambda_c}^2(3; 1, 2, a, c) = \tilde{\mathcal{A}}_{\lambda_3; \lambda_1 \lambda_2 \lambda_a \lambda_c}^2(3; 1, 2, a, c) - \tilde{\mathcal{A}}_{\lambda_3; \lambda_1 \lambda_2 \lambda_a \lambda_c}^2(3; 2, 1, a, c) , \quad (2.71)$$

with

$$\begin{aligned} \tilde{\mathcal{A}}_{+; +++++}^2(3; 1, 2, a, c) = & 8P_{4cd}P_{3ab}P_{12ij} s_{4d}s_{3a}^* \left\{ 2\langle 2|4+d|c\rangle\langle b|3+a|j\rangle\langle 1|2+j|i\rangle \right. \\ & \left. - s_{21}s_{ji}^*(b_2\langle b|3+a|2\rangle\langle 2|4+d|c\rangle + b_j\langle b|3+a|j\rangle\langle j|4+d|c\rangle) \right\} . \end{aligned} \quad (2.72)$$

The amplitudes for the other helicities are obtained as in (2.69).

Finally, the third topology (Fig. 2c) contributes four times,

$$\mathcal{M}_{\lambda_1 \lambda_2 \lambda_3 \lambda_a \lambda_c}^3(1, 2, 3) = \sum_{\{a, c\}} \mathcal{A}_{\lambda_3; \lambda_1 \lambda_2 \lambda_a \lambda_c}^3(3; 1, 2, a, c) + \mathcal{A}_{\lambda_3; \lambda_1 \lambda_2 \lambda_a \lambda_c}^{3*}(4; i, j, b, d) . \quad (2.73)$$

where the subamplitude is also antisymmetric with respect to the two gluons,

$$\mathcal{A}_{\lambda_3; \lambda_1 \lambda_2 \lambda_a \lambda_c}^3(3; 1, 2, a, c) = \tilde{\mathcal{A}}_{\lambda_3; \lambda_1 \lambda_2 \lambda_a \lambda_c}^3(3; 1, 2, a, c) - \tilde{\mathcal{A}}_{\lambda_3; \lambda_1 \lambda_2 \lambda_a \lambda_c}^3(3; 2, 1, a, c) . \quad (2.74)$$

The basic subamplitude for positive helicities is,

$$\begin{aligned} \tilde{\mathcal{A}}_{+; +++++}^3(3; 1, 2, a, c) = & -8P_{4cd}P_{31i2j}P_{12ij} s_{4d}\langle b|4+d|c\rangle \\ & \left\{ 2s_{j3}^*\langle 1|2+j|i\rangle\langle 2|3+1+i+j|a\rangle + s_{21}s_{ji}^*(b_j s_{3j}^*\langle j|3+1+i|a\rangle + b_2 s_{32}^*\langle 2|3+1+i|a\rangle) \right\} , \end{aligned} \quad (2.75)$$

while the negative helicity amplitudes are again obtained through (2.69).

2.3 CROSS SECTIONS

In the previous sections, we have presented expressions for the summed and squared matrix elements for the scattering of quarks (2.1). In practice, however, all possible crossed processes contribute with matrix elements related by simple permutations of arguments,

$$\begin{aligned}
f_1 f_2 \rightarrow f_3 f_4 Z Z & \quad ; \quad |\mathcal{M}^{f_1 f_2 f_3 f_4}(1, 2, 3, 4)|^2, \\
\bar{f}_3 \bar{f}_4 \rightarrow \bar{f}_1 \bar{f}_2 Z Z & \quad ; \quad |\mathcal{M}^{f_1 f_2 f_3 f_4}(3, 4, 1, 2)|^2, \\
f_1 \bar{f}_4 \rightarrow f_3 \bar{f}_2 Z Z & \quad ; \quad |\mathcal{M}^{f_1 f_2 f_3 f_4}(1, 4, 3, 2)|^2, \\
\bar{f}_3 f_2 \rightarrow \bar{f}_1 f_4 Z Z & \quad ; \quad |\mathcal{M}^{f_1 f_2 f_3 f_4}(3, 2, 1, 4)|^2, \\
f_1 \bar{f}_3 \rightarrow \bar{f}_2 f_4 Z Z & \quad ; \quad |\mathcal{M}^{f_1 f_2 f_3 f_4}(1, 3, 2, 4)|^2, \\
\bar{f}_4 f_2 \rightarrow f_3 \bar{f}_1 Z Z & \quad ; \quad |\mathcal{M}^{f_1 f_2 f_3 f_4}(4, 2, 3, 1)|^2.
\end{aligned} \tag{2.76}$$

In these permutations, the coefficients b_i must be adjusted so that the relations (2.12) and (2.13) are maintained. This is achieved by flipping the sign of b_i when particle i moves from the initial state to the final state or vice versa.

Similarly, the matrix elements for the crossed processes for the mixed QCD-electroweak process (2.2) are given by,

$$\begin{aligned}
gg \rightarrow \bar{q} q Z Z & \quad ; \quad |\mathcal{M}^{ggq\bar{q}}(1, 2, 3, 4)|^2, \\
g\bar{q} \rightarrow \bar{q} g Z Z & \quad ; \quad |\mathcal{M}^{ggq\bar{q}}(1, 4, 3, 2)|^2, \\
gq \rightarrow gq Z Z & \quad ; \quad |\mathcal{M}^{ggq\bar{q}}(1, 3, 2, 4)|^2, \\
\bar{q}g \rightarrow \bar{q}g Z Z & \quad ; \quad |\mathcal{M}^{ggq\bar{q}}(4, 2, 3, 1)|^2, \\
qg \rightarrow gq Z Z & \quad ; \quad |\mathcal{M}^{ggq\bar{q}}(3, 2, 1, 4)|^2, \\
\bar{q}q \rightarrow gg Z Z & \quad ; \quad |\mathcal{M}^{ggq\bar{q}}(4, 3, 1, 2)|^2.
\end{aligned} \tag{2.77}$$

Once the summed matrix elements are known, the parton level differential cross section is given by,

$$d\hat{\sigma} = \frac{1}{2\hat{s}} \frac{1}{4} C_F I_F \frac{1}{2} |\mathcal{M}|^2 d\text{Lips}(6), \quad (2.78)$$

where C_F is a colour averaging factor which depends on the partons in the initial state, and which is equal to $\frac{1}{9}$ for qq , $q\bar{q}$, $\bar{q}q$ or $\bar{q}\bar{q}$ scattering, $\frac{1}{24}$ for gq , $g\bar{q}$, qg or $\bar{q}g$ scattering and $\frac{1}{64}$ for gg scattering. The factor $\frac{1}{2}$ represents the statistical factor for two Z bosons in the final state, while I_F is the additional statistical factor for identical partons equal to $\frac{1}{2}$ if there are either identical quarks or identical antiquarks or two gluons in the final state. The other factors are due to the initial flux, spin averaging and phase space. For the six particle phase space, $d\text{Lips}(6)$, we use the standard Particle Data Group convention.²¹⁾

Finally, we obtain the full hadronic cross section by integrating over the parton distribution functions,

$$d\sigma(pp \rightarrow ZZX) = dx_1 dx_2 f_{f_1/p}(x_1, Q^2) f_{f_2/p}(x_2, Q^2) d\hat{\sigma}. \quad (2.79)$$

2.4 GAUGE INVARIANCE

We have made several checks on the helicity amplitudes presented in Sections 2.1 and 2.2. First of all, we have checked that each helicity amplitude is invariant under gauge transformations of the polarisation vector of either Z boson in the limit that the Z boson is massless. This is done by noting that the decay current for a Z boson with momentum $b_a p_a + b_b p_b$ (and consequently mass $2b_a b_b p_a \cdot p_b$) is proportional to p_a^μ when $p_a = p_b$,

$$\bar{u}_\lambda(p_a) \gamma^\mu u(p_a) \propto p_a^\mu.$$

Therefore, choosing $p_a = p_b$ (and setting $b_b = 0$) is equivalent to testing gauge invariance. In this limit, the diagrams of Fig. 1c no longer contribute and each helicity amplitude should vanish.

In the case of neutral boson exchange, this only tests the groups of diagrams (2.20) and (2.31) since the topologies of Fig. 1a and Fig. 1b are then separately gauge invariant. For W exchange, however, this is a much more powerful test since only the sum of all diagram topologies is gauge invariant.

Secondly, we checked that the helicity amplitudes for the processes containing gluons (a) are invariant under different choices of the auxiliary vectors p_i and p_j in the polarisation vectors of the gluons, and (b) satisfy gauge invariance of the gluon by vanishing when either of the auxiliary vectors is chosen to be the gluon momentum.

These tests, however, only check the helicity amplitudes. We have checked the full program for $pp \rightarrow ZZX$ against the numerical results of Ref. 18 and Ref. 19 using the appropriate input parameters. Within the accuracy of the Monte Carlo integration (approximately $\pm 5\%$) the results agree.

3. Higgs Boson Signals in $qq \rightarrow qqZZ$

3.1 PRELIMINARIES

Using the helicity amplitudes presented in the last section, we can now compute the cross section for the process (1.2), including all non-resonant diagrams. The channel where both Z bosons decay into charged lepton pairs is potentially the cleanest for Higgs boson detection at hadron supercolliders. In this case the Z boson momenta can be fully reconstructed and one can treat the Z bosons as final state particles rather than their leptonic decay products. Furthermore, we make the simplification of treating the final state Z bosons in the narrow width approximation, while still keeping the full width dependence of the exchanged vector boson propagators. Since finite width effects are expected to be small, we shall ignore them in the following.

We shall focus on two extreme values of the Higgs boson mass. Firstly, $m_H = 500$ GeV, where the Higgs boson width is small ($\Gamma_H = 62$ GeV), and where a clear resonance is expected. Secondly, we shall consider a very heavy Higgs boson, $m_H = 1$ TeV. In this case, the width of the Higgs is so large, $\Gamma_H = 503$ GeV,

that it is **not** clear whether or not an observable resonance structure exists. Since, as we will **show**, the $qq \rightarrow qqZZ$ contribution becomes relatively more important with increasing m_H , these two representative Higgs boson masses span the region between ‘light’ Higgs bosons, where production is dominated by gluon fusion, and ‘heavy’ Higgs bosons, where the electroweak sector becomes strongly interacting.

To simulate detector response, we shall impose a rapidity cut of,

$$|y_Z| < 2.5 , \quad (3.1)$$

on the **outgoing** Z bosons and a separation cut on the jets in the rapidity-azimuthal-angle plane of,

$$\Delta R_{jj} > 0.7 , \quad (3.2)$$

where

$$\Delta R = [(\Delta\phi)^2 + (\Delta y)^2]^{1/2} . \quad (3.3)$$

Note that for $qq \rightarrow qqZZ$ via electroweak interactions, a p_T cut on the outgoing jets is **not** necessary in order to obtain a finite tree level cross section, and only when mixed QCD-electroweak diagrams are included (Section 4), does a finite jet transverse momentum cut need to be imposed to avoid singularities.

On the other hand, the ΔR_{jj} cut is necessary to achieve a finite cross section, due to the collinear singularity introduced by photon bremsstrahlung diagrams which are incorporated in our calculation. The effect of the jet-jet separation cut is demonstrated in Fig. 3, where we show the jet-jet invariant mass distribution, $d\sigma/dm_{jj}$, in $qq \rightarrow qqZZ$ for pp collisions at $\sqrt{s} = 40$ TeV for a Higgs boson mass of $m_H = 1$ TeV. Very similar results are obtained for different values of m_H . The solid curve represents the contribution from $Z + \gamma$ exchange diagrams, while the dashed line shows the cross section resulting from W exchange graphs. The W and Z resonance peaks, corresponding to $W^\pm ZZ$ and ZZZ production where the W or one of the Z bosons decays hadronically, are clearly visible. Although the W exchange cross section rapidly falls for $m_{jj} < 20$ GeV, the m_{jj} distribution resulting from $Z + \gamma$ exchange graphs rises at small jet-jet invariant masses due to the collinear

singularity present in the photon exchange diagrams. For $m_{jj} < 20$ GeV, the cross section is totally dominated by the divergent photon exchange graphs. The ΔR_{jj} cut (3.2) regulates the singularity and sharply cuts off $d\sigma/dm_{jj}$ for jet-jet masses smaller than 5 GeV.

The SM parameters used in Fig. 3 and all subsequent figures and tables are $m_t = 120$ GeV, $\alpha = \alpha(M_Z) = 1/128$, $M_Z = 91.1$ GeV, $\sin^2 \theta_W = 0.23$ and $M_W = M_Z \cos \theta_W = 80$ GeV. These values are consistent with recent measurements at SLC,²²⁾ LEP,²³⁾ and the Tevatron.²⁴⁾ We use the parton distribution functions of Duke and Owens, set I²⁵⁾ with momentum scale $Q^2 = \hat{s}/4$, where \hat{s} is the parton center of mass energy squared.

3.2 ZZ PAIR AND INDIVIDUAL Z BOSON DISTRIBUTIONS

The most obvious strategy to search for the Higgs boson in the $H \rightarrow ZZ \rightarrow \ell^+ \ell^- \ell'^+ \ell'^-$ channel, is to look for a resonance structure in the invariant mass spectrum, $d\sigma/dm_{ZZ}$, of the Z boson pair in the inclusive reaction, $pp \rightarrow ZZ + X$. In Fig. 4, we show the m_{ZZ} distribution for $qq \rightarrow qqZZ$ summed over all possible combinations of quarks and antiquarks at the LHC and SSC for two different Higgs boson masses, $m_H = 0.5$ TeV and $m_H = 1$ TeV. The solid curve shows the total cross section, while the dashed line represents the contribution from Z and photon exchange graphs. It is clear that the cross section is dominated by the W exchange diagrams, with Z boson and photon exchange contributing at most 25% to the cross section. The reason for the dominance of the W exchange diagrams lies with the much larger couplings of the W with the quarks within the proton.

From Fig. 4, one also observes that the Higgs resonance structure is much more pronounced in the $Z + \gamma$ exchange graphs than in the total cross section. This is particularly obvious if the Higgs boson mass is large (see Figs. 4b and 4d) where, although the resonance is clearly visible in $Z + \gamma$ exchange for $m_H = 1$ TeV, it is diluted to a shoulder in the total m_{ZZ} distribution. The source of this effect are the diagrams shown in Fig. 1d – 1f, which contribute only to W boson exchange. They include nonabelian vertices between 3 or 4 electroweak vector bosons and produce a much harder m_{ZZ} spectrum than the other non-resonant graphs.

W and $Z + \gamma$ exchange diagrams tend to interfere destructively. The magnitude of the interference terms, however, is about two orders of magnitude smaller than the contribution of the $Z + \gamma$ exchange diagrams. The reason that the interference effects are small lies with the fact that the momenta of the final state quarks must be crossed to have interference between diagrams with intermediate W 's and intermediate Z 's and photons (see Eqs. (2.60) and (2.61)). The largest contributions arise when there is a small momentum transfer between the initial and final state quark. This is not, in general, simultaneously true for W exchange and $Z + \gamma$ exchange due to the crossed momenta, and thus the interference terms are suppressed.¹⁹⁾

In Fig. 4, we also compare the results of the full calculation with the approximation where only s -channel Higgs pole diagrams are taken into account (dotted line), and with the effective W approximation in the resonance region $m_H - \Gamma_H < m_{ZZ} < m_H + \Gamma_H$ (dash-dotted line). The observed Z pair invariant mass distribution in the s -channel approximation can be easily understood from the behaviour of its amplitude, \mathcal{A}_s , with m_{ZZ} ,

$$\mathcal{A}_s \sim m_{ZZ}^4 \frac{1}{m_{ZZ}^2 - m_H^2 + im_H \Gamma_H} . \quad (3.4)$$

At energies below m_H , \mathcal{A}_s is small and the non-resonant amplitudes dominate the total result. Close to the Higgs mass, \mathcal{A}_s is the most significant amplitude and, provided that m_H is not too large, the s -channel pole approximation describes the m_{ZZ} distribution reasonably well for $m_H - \Gamma_H < m_{ZZ} < 1$ TeV, although the Higgs peak is somewhat underestimated. This is illustrated in Figs. 4a and 4c for $m_H = 0.5$ TeV.

For larger values of m_{ZZ} , \mathcal{A}_s grows like m_{ZZ}^2 , thus violating unitarity. Good high energy behaviour is only obtained when all other diagrams are included in the calculation.¹⁷⁾ The s -channel Higgs pole approximation therefore seriously overestimates the cross section in the high m_{ZZ} region. For a heavy Higgs boson, this implies that the s -channel pole approximation is not useful. As shown in Figs. 4b and 4d for a Higgs boson with 1 TeV mass, the s -channel pole approximation underestimates $d\sigma/dm_{ZZ}$ for $m_{ZZ} < m_H$, and significantly overestimates the cross

section for practically all m_{ZZ} values greater than m_H . We also observe that the Z pair invariant mass distribution in the s -channel pole approximation peaks at a value somewhat larger than m_H . To avoid anomalous effects due to the unitarity violating behaviour, from now on, we will restrict the invariant mass range for which we compare the results of the exact calculation with the s -channel pole approximation to the resonance region, $m_H - \Gamma_H < m_{ZZ} < m_H + \Gamma_H$.

In contrast to the amplitude of the s -channel Higgs pole approximation, the amplitude of the effective W approximation exhibits a good high energy behaviour, provided that all $ZZ \rightarrow ZZ$ and $WW \rightarrow ZZ$ diagrams are taken into account. The gauge boson distribution functions, $f_{\lambda,V}^q(x)$, which describe the probability that a quark q dissociates into a gauge boson $V = W, Z$, with helicity $\lambda = 0, \pm 1$, and momentum fraction x , have been derived by several groups.^{9,26–32} The different calculations agree in the leading order contributions to $f_{\lambda,V}^q(x)$, although the non-leading terms depend on the details of the approximation used. In the following, we shall use the form of Ref. 29,

$$\begin{aligned} f_{0,V}^q(x) &= \frac{1}{8\pi^2} \left[\left(c_+^{Vq} \right)^2 + \left(c_-^{Vq} \right)^2 \right] \frac{1-x}{x} \frac{Q^2}{Q^2 + M_V^2(1-x)} , \\ f_{\pm,V}^q(x) &= \frac{1}{16\pi^2 x} \left[\left(c_{\mp}^{Vq} \right)^2 + (1-x)^2 \left(c_{\pm}^{Vq} \right)^2 \right] \\ &\quad \left\{ \log \left[\frac{Q^2 + M_V^2(1-x)}{M_V^2(1-x)} \right] - \frac{Q^2}{Q^2 + M_V^2(1-x)} \right\} , \end{aligned} \quad (3.5)$$

where $V = W, Z$ and c_{\pm}^{Vf} is given in (2.22). Q^2 represents the characteristic energy scale of the process.

Due to the logarithmic factor in $f_{\pm,V}^q(x)$, contributions to the cross section originating from transversely polarised gauge bosons depend considerably on the Q^2 value chosen. This is illustrated in Fig. 5, where we show the ZZ invariant mass spectrum for a Higgs boson with mass $m_H = 0.5$ TeV produced in pp collisions at $\sqrt{s} = 40$ TeV for two values of Q^2 . Both Z bosons are required to have rapidity $|y_Z| < 2.5$. The contributions when either both vector bosons are longitudinally polarised (LL) or when at least one is transversely polarised (TT+TL) are shown

separately. The solid curves correspond to $Q^2 = m_{ZZ}^2$,³³⁾ while the dotted lines represent the result for $Q^2 = m_{ZZ}^2/4$. It is clear that the predicted m_{ZZ} distribution resulting from the exchange of transversely polarised vector bosons is much more sensitive to the choice of Q^2 than when only longitudinally polarized vector bosons are exchanged.

Since the Higgs boson couples predominantly to longitudinal W and Z bosons, the Higgs resonance peak is only visible when both intermediate vector bosons are longitudinally polarized. In the resonance region, $m_H - \Gamma_H < m_{ZZ} < m_H + \Gamma_H$, the contribution from the longitudinal gauge bosons dominates, whereas away from the peak, transverse intermediate states are responsible for the major part of the cross section. The effective W approximation clearly does not yield a reliable prediction for $d\sigma/dm_{ZZ}$ outside the resonance region. In the following, we therefore restrict the invariant mass range for which we compare the results of the effective W approximation and the exact calculation to the region $m_H - \Gamma_H < m_{ZZ} < m_H + \Gamma_H$, and take only the contribution originating from two longitudinal intermediate bosons into account. We also choose $Q^2 = m_{ZZ}^2/4$.

From Fig. 4, we see that the Z boson pair invariant mass distribution obtained with the effective W approximation is in very good agreement with the result of the exact calculation in the resonance region. Only at the lower limit of the considered mass range for the 1 TeV Higgs boson does a significant discrepancy arise which is due to the importance of non-resonant diagrams.

As mentioned in the Introduction, the vector boson fusion process (1.2) is expected to be an important source for Higgs bosons when m_H is large. In Fig. 6, we compare the Z boson pair invariant mass spectrum from $qq \rightarrow qqZZ$ (solid line) and $gg \rightarrow ZZ$ (dash-dotted line), and the $q\bar{q} \rightarrow ZZ$ background (dotted line) for $m_H = 1$ TeV and $m_t = 120$ GeV at both the LHC and the SSC. For the $gg \rightarrow ZZ$ amplitudes, we used the analytic expressions given in Ref. 8 which include all contributions from the non-resonant box graphs and the interference terms with the $gg \rightarrow H \rightarrow ZZ$ triangle diagram. The cross section of the gluon fusion process in the resonance region depends significantly on the top quark mass. One observes that the $q\bar{q} \rightarrow ZZ$ background at the LHC (Fig. 6a) is relatively

more important than at the SSC (Fig. 6b). The signal to background ratio can be improved somewhat by either a more stringent Z boson rapidity cut of $|y_Z| < 1.5$, or by imposing a transverse momentum cut $p_{TZ} > \frac{1}{4} m_{ZZ}$ ^{8,15)} on the Z bosons. In both cases, however, a nonnegligible part of the signal is lost. By imposing a more stringent rapidity cut, the $gg \rightarrow ZZ$ signal is reduced by about a factor 2, while the $qq \rightarrow qqZZ$ cross section is only slightly affected. The p_{TZ} cut, on the other hand, reduces the vector boson fusion signal significantly but leaves the $gg \rightarrow ZZ$ signal almost unchanged.

From Fig. 6, one also observes that the m_{ZZ} spectrum from $gg \rightarrow ZZ$ and $q\bar{q} \rightarrow ZZ$ drops much faster than the invariant mass distribution from $qq \rightarrow qqZZ$. For m_{ZZ} values larger than 1 TeV, vector boson fusion dominates over the gluon fusion process, while the cross sections of the $qq \rightarrow qqZZ$ and $q\bar{q} \rightarrow ZZ$ processes are similar. The flatness of the Z boson pair invariant mass spectrum in $qq \rightarrow qqZZ$ can be traced to the diagrams shown in Fig. 1c – 1f. Due to the propagators of the intermediate vector bosons, these diagrams are enhanced by $\log(\hat{s}/M_V^2)$ factors over the graphs describing $q\bar{q}$, $gg \rightarrow ZZ$, thus leading to a significantly harder m_{ZZ} distribution.

To discriminate between the vector boson fusion process (1.2) and $q\bar{q}$, $gg \rightarrow ZZ$, one can try to make use of the different topology of the processes. In lowest order, the Z boson pair in quark-antiquark annihilation and gluon fusion is produced with a small transverse momentum. In contrast, the vector boson fusion mechanism produces Z boson pairs with sizeable p_T . This follows from the behaviour of the propagator of the exchanged W 's or Z 's. The propagator is roughly $(p_{TV}^2 + M_V^2)^{-1}$ where p_{TV} is the transverse momentum of the exchanged vector boson, ($V = W, Z$), relative to the incident direction. The exchanged bosons therefore have a transverse momentum, $p_{TV} \sim \mathcal{O}(M_W)$, which is then reflected in the transverse momentum of the final state Z boson pair.

Fig. 7 shows the p_{TZZ} distribution for $m_H = 1$ TeV at the SSC integrated both over the full range of m_{ZZ} (solid line) and when the Z boson pair invariant mass is restricted to the resonance region, $m_H - \Gamma_H < m_{ZZ} < m_H + \Gamma_H$ (dashed curve). As expected, both distributions peak at $p_{TZZ} \approx M_W$. For comparison, we also show

the Z boson pair transverse momentum spectrum for the Higgs pole approximation in the resonance region (dotted line). One observes that for small values of p_{TZZ} , Higgs pole diagrams dominate in the resonance region. For large values of p_{TZZ} , however, the transverse momentum distribution of the Higgs pole approximation drops much faster than that resulting from the exact calculation. In this region, non-resonant diagrams are the dominant source of high p_T Z boson pairs. A finite Z pair transverse momentum cut to reduce the $q\bar{q} \rightarrow ZZ$ background will, therefore, also diminish the contribution of the Higgs pole diagrams in the vector boson fusion process.

In Fig. 7, we also show the approximate analytical form from the Higgs pole diagram derived in Ref. 12 (dash-dotted line),

$$\frac{d\sigma}{dp_{TZZ}} = \frac{2z}{p_{TZZ}} N F(z) , \quad (3.6)$$

where,

$$F(z) = \frac{2z^2 - 4z}{(z^2 + 4z)^2} + 16z \frac{1 + z}{(z^2 + 4z)^{5/2}} \operatorname{arctanh} \left[\left(1 + \frac{4}{z} \right)^{-1/2} \right] , \quad (3.7)$$

and,

$$z = \frac{\sqrt{s}}{\sqrt{s} - m_H} \frac{p_{TZZ}^2}{M_W^2} . \quad (3.8)$$

The normalisation N is such that the analytic form reproduces the total cross section for the Higgs pole approximation. This approximation is expected to break down for $p_{TZZ} \gg M_W$ due to terms neglected in the derivation of $F(z)$.¹²⁾ Fig. 7 shows that this is indeed the case: for $p_{TZZ} > 200$ GeV the approximate form seriously overestimates the exact result obtained from the Higgs pole diagrams. However, at small p_{TZZ} the approximation fits the dotted line reasonably well, as expected.

Another way to improve the Higgs boson signal in $qq \rightarrow qqZZ$ might be to look at the transverse momentum distributions of the individual Z bosons. Since the Higgs boson decays isotropically in its center of mass frame, one expects to observe

a Jacobian peak at $p_{TZ} \approx \frac{1}{2} \sqrt{m_H^2 - M_Z^2}$. For large Higgs boson masses, however, the Jacobian peak is substantially smeared out by finite width effects. In Fig. 8, we show the p_{TZ}^{Hi} and p_{TZ}^{Lo} distributions for $m_H = 0.5$ TeV at the SSC, where,

$$p_{TZ}^{Hi} = \max\{p_{TZ_1}, p_{TZ_2}\} , \quad p_{TZ}^{Lo} = \min\{p_{TZ_1}, p_{TZ_2}\} , \quad (3.9)$$

are the maximum and minimum transverse momenta of the Z bosons.

The Jacobian peak is quite obscured by the non-resonant diagrams if m_{ZZ} is integrated over its full range (solid line) and only shows up clearly when the Z boson pair invariant mass is restricted to the resonance region (short-dashed curve). Near the peak, at $p_{TZ}^{Hi}, p_{TZ}^{Lo} \approx \frac{1}{2} m_H$, the major part of the cross section originates from s-channel Higgs exchange diagrams. This is clearly shown by the dotted line which shows the transverse momentum spectrum in the Higgs pole approximation in the resonance region. It is also clear that the Higgs pole approximation does not faithfully describe the shape of the p_T distribution at smaller p_{TZ} .

It is also interesting to examine the p_{TZ} distributions for the exact calculation in the same m_{ZZ} range when no Higgs boson resonance is present. The Higgs boson may then be either heavier, $m_H \gg m_{ZZ}$, or lighter, $m_H \ll m_{ZZ}$, than the range of m_{ZZ} we are considering. In the heavy m_H region, the exact matrix elements mimic the ‘bad’ high energy behaviour of the Higgs pole approximation and violate unitarity.³⁴⁾ However, in the small m_H limit, the cancellation of the unitarity violating behaviour between the Higgs and non-Higgs graphs is complete, and the result is well behaved. We therefore define the perturbative ‘no-resonance’ approximation to be the exact matrix elements evaluated with small m_H , which corresponds to a weakly interacting electroweak sector. In practice, the precise value of m_H is unimportant provided $m_H \ll m_{ZZ}$. The ‘no-resonance’ approximation is shown as a long-dashed line in Fig. 8. In this case, of course, only non-resonant diagrams contribute and no Jacobian peak is observed.

In Fig. 8, we also show the p_{TZ}^{Hi} and p_{TZ}^{Lo} distributions for the effective W approximation in the resonance region (dash-dotted line). Since the Z pair transverse momentum is neglected in the effective W approximation, p_{TZ}^{Hi} and p_{TZ}^{Lo} coincide,

and the effective W approximation is unable to describe the high p_{TZ} tail correctly. Furthermore, due to the transverse motion of the Z pair, the Jacobian peak of the $p_{TZ}^{H^i}$ ($p_{TZ}^{L^o}$) distribution in the full calculation occurs at somewhat higher (lower) values of p_T than in the effective W approximation.

Since the Higgs boson decays isotropically in its center of mass frame, one expects that s -channel Higgs boson diagrams contribute the major part of the cross section for small Z boson rapidities. Fig. 9, where we show the $d\sigma/d|y_Z^{H^i}|$ distribution for $m_H = 1$ TeV at the SSC, clearly demonstrates this. $y_Z^{H^i}$ is the higher of the two Z boson rapidities, defined analogously to (3.9). As in Fig. 8, we show the distributions for the exact result integrated both over all m_{ZZ} (solid) and the resonance region (short-dashed), s -channel Higgs exchange (dots), effective W approximation (dash-dotted) and the perturbative ‘no-resonance’ approximation (long-dashed). In contrast to the transverse momentum distribution of the Z bosons, the effective W approximation describes the $|y_Z^{H^i}|$ spectrum rather well, particularly for small rapidities. This explains the rather better agreement of the effective W approximation with the exact result for smaller rapidity cuts on the Z bosons.³⁵⁾ As shown by the ‘no-resonance’ curve, non-resonant diagrams contribute most at large rapidities.

A rather unmistakable signal for a heavy Higgs boson is the angular distribution, $d\sigma/d\cos\theta^*$, of the charged leptons in $H \rightarrow ZZ \rightarrow \ell^+\ell^-\ell'^+\ell'^-$, where θ^* is the polar angle of the charged lepton with respect to the Z direction, determined in the Z boson rest frame.³⁶⁾ Heavy Higgs bosons decay predominantly into longitudinally polarized Z bosons, which, since the Z boson coupling to charged leptons is almost purely axial vector, leads to a distinctive $\sin^2\theta^*$ angular distribution. Transversely polarized Z bosons, however, produce a $\frac{1}{2}(1 + \cos^2\theta^*)$ distribution.

Fig. 10 shows the normalised $\cos\theta^*$ distribution, $(1/\sigma) \cdot (d\sigma/d\cos\theta^*)$, for $m_H = 0.5$ TeV at the SSC. It is clear that s -channel Higgs exchange diagrams result in a typical $\sin^2\theta^*$ distribution (dotted line). The dominance of the Higgs pole diagrams in the resonance region is reflected by the dashed curve, which shows the $\cos\theta^*$ distribution obtained from the full calculation with the Z boson pair invariant mass integrated between $m_H \pm \Gamma_H$. For $m_H = 0.5$ TeV, the cross section in the

resonance region is so large that the $\sin^2 \theta^*$ shape is still evident even when m_{ZZ} is integrated over its full range (solid line). The effect on the $\cos \theta^*$ distribution induced by the Higgs resonance can be seen by comparing the ‘no-resonance’ (dash-dotted) with the exact result in the resonance region (dashed). As expected, the ‘no-resonance’ approximation, which should contain relatively few longitudinally polarised Z bosons, is much flatter.

3.3 JET ACTIVITY

We have seen in Section 3.2 that the Z boson pair in $qq \rightarrow qqZZ$ has a typical transverse momentum, $p_{TZZ} \sim \mathcal{O}(M_W)$, which is balanced by the transverse momentum of the two final state quark jets. In Fig. 11, we show the exact p_{Tj}^{Hi} and p_{Tj}^{Lo} distributions for $m_H = 1$ TeV at the SSC integrated both over the full range of m_{ZZ} (solid line) and when m_{ZZ} is restricted to the resonance region (dashed curve). p_{Tj}^{Hi} (p_{Tj}^{Lo}) is the higher (lower) jet transverse momentum defined analogously to (3.9).

For comparison, we also show the jet transverse momentum distributions for the Higgs pole approximation in the resonance region (dotted line). As in the p_{TZZ} distribution, one observes that s -channel diagrams dominate in the resonance region for small p_{Tj}^{Hi} and p_{Tj}^{Lo} values. A significant fraction of $qq \rightarrow qqH \rightarrow qqZZ$ events is seen to have at least one jet with a p_T exceeding 50 GeV (Fig. 11a). However, at larger p_{Tj} the Higgs pole approximation grossly underestimates the cross section, especially in the p_{Tj}^{Lo} distribution. In this region, non-resonant diagrams are the dominant source of $ZZjj$ events. This is clearly shown by the perturbative ‘no-resonance’ approximation (dash-dotted curve) which (almost) coincides with the exact result in the resonance region (dashed curve) for $(p_{Tj}^{Hi} > 400 \text{ GeV})$ $p_{Tj}^{Lo} > 400 \text{ GeV}$. A jet p_T cut, which would help to reduce the $q\bar{q} \rightarrow ZZ$ background, will therefore tend to diminish the contribution of the Higgs resonance.

It is interesting to note that the contribution from $Z + \gamma$ exchange diagrams to the cross section falls steeply with increasing jet transverse momentum, while the interference terms between W and $Z + \gamma$ exchange gain importance. For very large values of p_{Tj} , the interference terms have a similar size to the contribution from Z and photon exchange. This can be easily understood by recalling that

s -channel Higgs pole diagrams, for which the p_{Tj} distributions drop much faster than for the W exchange dominated total cross section, play a more important role for diagrams with intermediate Z bosons and photons than for W exchange graphs (see Fig. 4). The relative importance of the interference effects becomes clear by noting that the momenta of the final state quarks must be crossed to have interference effects. Interference terms are therefore most important when the momentum transfer between initial and final state quarks is large, *i.e.* at large values of p_{Tj} .

More insight into the characteristics of the jets in $qq \rightarrow qqZZ$ events can be obtained from the jet pseudorapidity distributions, $d\sigma/d|\eta_j^{Hi}|$ and $d\sigma/d|\eta_j^{Lo}|$, which are shown in Fig. 12 for $m_H = 1$ TeV at the SSC. One observes that the exact result integrated over the full m_{ZZ} range (solid line) peaks at a value of about 3.5 in the $|\eta_j^{Hi}|$ distribution, while $|\eta_j^{Lo}|$ assumes its maximum at zero. These values change if m_{ZZ} is restricted to the resonance region (dashed line). The most dramatic change occurs in $|\eta_j^{Lo}|$, which now exhibits a dip at zero and peaks at a pseudorapidity around 2.5. At large values of $|\eta_j|$, the contribution of the s -channel Higgs pole diagrams (dotted line) dominates, whereas for small pseudorapidities non-resonant diagrams account for the major part of the cross section. This is illustrated by the dash-dotted line which shows the $|\eta_j^{Hi}|$ and $|\eta_j^{Lo}|$ distribution in the same m_{ZZ} region for the perturbative ‘no-resonance’ approximation where non-resonant diagrams dominate. A large fraction of events is seen to have at least one jet with $|\eta_j| > 2.5$.

The structure observed in the jet pseudorapidity distributions is also reflected in the jet-jet separation ΔR_{jj} . Fig. 13 displays the ΔR_{jj} spectrum for $m_H = 1$ TeV at the SSC. Since the two jets are generally emitted back-to-back in azimuth, $\Delta\phi \approx \pi$, and with rather different pseudorapidities, ΔR_{jj} peaks at large values. The $\Delta R_{jj} > 0.7$ cut, which we have imposed in all our numerical simulations, clearly has a very small effect on the total cross section. As in Fig. 12, the solid line represents the exact result when m_{ZZ} is integrated over its full range. The ΔR_{jj} distribution in the resonance region (dashed curve) is dominated by the s -channel Higgs pole diagrams at large values, and by non-resonant diagrams at smaller ΔR_{jj} . This is illustrated by the dotted and dash-dotted lines which give the ΔR_{jj} spectrum in

the Higgs pole and ‘no-resonance’ approximations, respectively.

The jet activity in $qq \rightarrow qqZZ$ at the LHC and SSC is best reflected in the fraction of events which have 0, 1 and 2 jets with transverse momentum $p_{Tj} > p_{Tj}^{min}$ in either the ‘central’, $|\eta_j| < 2.5$, or the ‘forward’, $|\eta_j| > 2.5$, jet pseudorapidity regions. Tables 1 and 2 list these numbers for $m_H = 0.5$ TeV and $m_H = 1$ TeV with m_{ZZ} restricted to the resonance region, for two representative jet transverse momentum cuts, $p_{Tj}^{min} = 50$ GeV and $p_{Tj}^{min} = 100$ GeV.* The fraction of $qq \rightarrow qqZZ$ events having 1 or 2 jets with $p_{Tj} > p_{Tj}^{min}$ thus gives an indication of how many events resulting from vector boson fusion contain one or two observable high p_T jets.

We see that although a significant number of events have no jets passing the transverse momentum cuts, the majority of events do contain at least one jet in either the forward or central regions. This becomes more evident for heavier Higgs bosons and larger values of \sqrt{s} , especially for $p_{Tj}^{min} = 100$ GeV. The fraction of events with two high p_T jets depends sensitively on the value of p_{Tj}^{min} . For $p_{Tj}^{min} = 50$ GeV, 40 – 50% of the events contain two jets, most often with one in the central region and one in the forward region. This drops to 10 – 25% for $p_{Tj}^{min} = 100$ GeV. The division between forward and central regions is somewhat arbitrary, however, increasing or decreasing the defining rapidity cut (chosen in our case to be 2.5) only shifts events along the off-diagonal, conserving the total number of observed jets in the event.

It is also instructive to list the ‘inclusive’ fraction of events with 0, 1 or 2 jets in the central rapidity region. These numbers reflect the jet activity if hadronic calorimetry in supercollider experiments is not possible in the forward region. Even in this pessimistic case, a significant portion of the events (30 – 60%) contain at least one jet. Because of the smaller center of mass energy, the fraction of events with two jets in the central region is larger at the LHC than at the SSC. This is especially true for $m_H = 1$ TeV, where as many as 18% of the events contain two central jets with $p_{Tj} > 50$ GeV.

* It is expected that jets with $p_T > 50 - 100$ GeV can be separated from the underlying event structure in hadron supercolliders experiments.³⁷⁾

4. Searching for the Higgs Boson in $pp \rightarrow ZZ + n$ jets

4.1 THE $ZZjj$ BACKGROUND FROM MIXED QCD-ELECTROWEAK PROCESSES

From Tables 1 and 2 it is clear that a large portion of the $qq \rightarrow qqZZ$ cross section results in events with one or two high p_T jets in either the central or the forward pseudorapidity region. For these event topologies, ZZj and $ZZjj$ production via mixed QCD-electroweak processes provide a potentially dangerous background, especially when the Higgs boson is heavy and no clear resonance peak is observable. ZZj production was first considered in Ref. 12 and we shall come back to the single jet background in Section 4.2. However, we will first concentrate on Z boson pair production accompanied by two jets.

The mixed QCD-electroweak processes contributing to $ZZjj$ production are listed in (1.3) and (1.4). The matrix elements for these processes have been described in detail in Section 2 and it is straightforward to utilise them to compute the cross sections. In contrast to the pure electroweak $qq \rightarrow qqZZ$ amplitudes, the mixed QCD-electroweak matrix elements contain infrared and collinear divergences, thus becoming infinite in the limit $p_{Tj} \rightarrow 0$. A cut on the transverse momentum of the jets and the jet-jet separation is therefore necessary in order to obtain finite results. In the following, we shall impose a transverse momentum cut,

$$p_{Tj} > 100 \text{ GeV} , \quad (4.1)$$

on both jets and a separation cut of $\Delta R_{jj} > 0.7$. Furthermore, to approximately simulate detector response, we require $|y_Z| < 2.5$ and a Z -jet separation of $\Delta R_{Zj} > 0.7$. Since the opening angle of the charged lepton pair from the Z decay is quite small for large Higgs boson masses,³⁸⁾ ΔR_{Zj} approximately corresponds to a jet-lepton separation of the same magnitude.

In Fig. 14, we compare the invariant mass spectrum of the Z boson pair for $ZZjj$ production via electroweak interactions with $m_H = 1$ TeV (solid line) and via mixed QCD-electroweak processes (dashed line) at the LHC and the SSC. As expected from the discussion in the previous section, the contribution from the pure electroweak processes is much reduced by the p_{Tj} cut. This is particularly evident

in the Higgs resonance region. On the other hand, the mixed QCD-electroweak background is also much smaller than the $q\bar{q} \rightarrow ZZ$ background shown in Fig. 6. Nevertheless, the background is still larger than the electroweak signal over the whole range of m_{ZZ} . The $ZZjj$ background cross section is dominated by quark-gluon fusion processes, while quark initiated processes contribute about 30%, and gluon fusion about 5 – 10%.

Interference effects between pure electroweak and mixed QCD-electroweak processes are constructive, but rather small, amounting to less than 10% of the purely electroweak cross section. The reason for the smallness of the interference effects lies with the fact that, due to the colour structure of the matrix elements, the momenta of the final state quarks must be crossed in order to have interference effects. Furthermore, gluon fusion and quark-gluon initiated processes, which contribute the major part of the cross section do not interfere with the electroweak $qq \rightarrow qqZZ$ diagrams. In the Higgs resonance region, the final state Z bosons from the pure electroweak processes are mostly longitudinally polarised, whereas they are mostly transversely polarised in the mixed QCD-electroweak processes where the Higgs boson does not contribute. Since states with transversely and longitudinally polarised Z bosons in the final state do not interfere, interference effects between purely electroweak and mixed QCD-electroweak processes are particularly small in this region.

It is clear that the $ZZjj$ background from mixed QCD-electroweak processes must be reduced if this channel is to be useful in a Higgs boson search at hadron supercolliders. As we will now show, the rather different jet characteristics in electroweak $qq \rightarrow qqZZ$ production and the processes involving QCD offer several alternatives to improve the signal to background ratio.

Fig. 15 compares the normalised maximum and minimum jet pseudorapidity distributions for $ZZjj$ production via electroweak interactions with $m_H = 1$ TeV (solid line) with those from mixed QCD-electroweak processes (dashed line) at the SSC in the resonance region $m_H - \Gamma_H < m_{ZZ} < m_H + \Gamma_H$. In this region, the total background cross section is more than twice as large as the signal. The jets from the QCD processes are considerably more central than those produced in

purely electroweak interactions. The maxima of the jet rapidity spectra resulting from $ZZjj$ production via electroweak interactions are separated from the maxima resulting from the processes involving QCD by about 2 units in rapidity. From Fig. 15a, it is clear that restricting $|\eta_j^{Hi}|$ to the region above 2.5, which is equivalent to requiring at least one jet with $|\eta_j| > 2.5$, removes most of the background cross section ($\sim 80\%$), while the major part of the signal ($\sim 75\%$) is retained. This already improves the signal to background ratio to about 1.5:1. A cut of 2.5 on $|\eta_j^{Lo}|$, which corresponds to having two jets with $|\eta_j| > 2.5$ would almost completely eliminate the background, although at the cost of losing a substantial part of the signal as well (see Fig. 15b).

Alternatively, a minimum jet-jet invariant mass cut can be employed. Fig. 16 shows the m_{jj} distribution for $ZZjj$ production via electroweak interactions with a Higgs boson of mass 1 TeV (solid line) and for mixed QCD-electroweak processes (dashed line) at the SSC in the Higgs resonance region. Purely electroweak $ZZjj$ production results in a very broad m_{jj} distribution, which peaks at ~ 2.5 TeV and is essentially flat in the range $1 \text{ TeV} < m_{jj} < 5 \text{ TeV}$. For m_{jj} values larger than ~ 1.5 TeV, the electroweak processes dominate over processes involving QCD. A $m_{jj} > 1.5$ TeV cut would remove approximately 90% of the background cross section, while the signal would be reduced by only $\sim 30\%$. Since the two jets are typically back-to-back (see Figs. 13 and 17), this cut is roughly equivalent to the jet energy cut of $E_j > 1 \text{ TeV}$ described in Ref. 13.

A third possibility to suppress the QCD $ZZjj$ background is to require a large jet-jet separation. Fig. 17 compares the normalised ΔR_{jj} distribution from these processes (dashed line) with that for $ZZjj$ production via electroweak interactions with $m_H = 1 \text{ TeV}$ at the SSC in the Higgs resonance region (solid line). The ΔR_{jj} distribution from mixed QCD-electroweak processes peaks sharply at $\Delta R_{jj} \approx \pi$, indicating that most of the jets are back-to-back in azimuth, but have a small separation in rapidity. On the other hand, the ΔR_{jj} distribution peaks at a value of about 5 for electroweak $ZZjj$ production, reflecting the fact that jets resulting from this source are not only mostly back-to-back in azimuth but also have a rather large separation in rapidity. It is clear that a cut $\Delta R_{jj} > 4$ would strongly reduce the mixed QCD-electroweak background (by $\sim 90\%$) whereas most of the

signal ($\sim 70\%$) would be retained. It is also clear that the jet-jet separation just reflects the structure observed in the jet pseudorapidity distributions. A ΔR_{jj} cut, therefore, is roughly equivalent to a $|\eta_j|$ cut and vice versa.

Since the Higgs pole diagrams mostly contribute at very large values of $|\eta_j|$ and ΔR_{jj} (see Figs. 12 and 13), the jet rapidity and jet-jet separation cuts not only remove the background from mixed QCD-electroweak processes but also tend to suppress the contribution of the non-resonant electroweak diagrams with respect to the Higgs pole contribution in purely electroweak $ZZjj$ production. This is most welcome since the p_{Tj} cut tends to enhance the importance of the non-resonant diagrams as shown by Fig. 11 and by the lack of resonance structure (compared to Fig. 6) in Fig. 14.

4.2 HIGGS SIGNAL AND BACKGROUND IN $pp \rightarrow ZZ + n$ JETS

The results obtained in Section 3 and 4.1 can be summarized by listing the cross sections for $qq \rightarrow qqZZ$, both including the Higgs boson, σ_H , and for the perturbative ‘no-resonance’ background from non-resonant $qq \rightarrow qqZZ$ diagrams, σ_B , and the $\mathcal{O}(\alpha_W^2 \alpha_s^n)$ background in the $ZZ + n$ jet channel with $n = 0, 1, 2$ in the Higgs resonance region for different jet rapidity regions. As in Section 3, the perturbative ‘no-resonance’ background from the non-resonant diagrams is estimated by evaluating the exact $qq \rightarrow qqZZ$ matrix elements in the relevant m_{ZZ} range with a Higgs boson mass much less than m_{ZZ} , $m_H \ll m_{ZZ}$. These cross sections will also allow us to identify the channel with the most prominent Higgs boson signal. In the following, we shall discriminate between two cases. In the first case, we shall assume that jet identification at hadron supercolliders is only possible in the central pseudorapidity region, $|\eta_j| < 2.5$, while in the second, we shall analyse the more optimistic situation where jets can be also identified in the forward pseudorapidity region, $|\eta_j| > 2.5$. It is clear that jet identification in this region will be very difficult at hadron supercolliders.³⁹⁾

We first consider the situation where only central jets with $|\eta_j| < 2.5$ are observed. Tables 3 and 4 list the cross sections for $pp \rightarrow ZZ + n_C$ central jets, $n_C = 0, 1, 2$, with $p_{Tj} > 100$ GeV at the LHC and SSC for $m_H = 0.5$ TeV and

$m_H = 1$ TeV, with m_{ZZ} restricted to the resonance region. To present a coherent picture, we also include the $gg \rightarrow ZZ$ cross section.⁸⁾ The numbers in brackets represent the perturbative ‘no-resonance’ background from the non-resonant diagrams, σ_B , so that the difference, $\sigma_H - \sigma_B$, measures the size of the Higgs boson signal for a given process. There is no contribution to the mixed QCD-electroweak $\mathcal{O}(\alpha_W^2 \alpha_s^n)$ processes from the Higgs boson, so σ_H and σ_B coincide for these processes.

The cross sections for the purely electroweak process and the tree level $\mathcal{O}(\alpha_W^2 \alpha_s^2)$ reaction $pp \rightarrow ZZjj$ are calculated using the helicity amplitudes described in Section 2. For the $\mathcal{O}(\alpha_W^2 \alpha_s)$ reaction $pp \rightarrow ZZj$, we use the tree level matrix elements given in Ref. 40. To account for virtual and soft gluon corrections, we multiply the cross section for the $\mathcal{O}(\alpha_W^2)$ process $q\bar{q} \rightarrow ZZ$ by a K -factor,⁴¹⁾

$$K = 1 + \frac{8\pi}{9} \alpha_s(m_H^2) . \quad (4.2)$$

Finally, for the $\mathcal{O}(\alpha_s^2)$ gluon fusion process $gg \rightarrow ZZ$, we employ the analytical expressions of Ref. 8. No results are listed for the $\mathcal{O}(\alpha_s^3)$ and $\mathcal{O}(\alpha_s^4)$ processes. For the latter, the matrix elements do not exist, while for the $\mathcal{O}(\alpha_s^3)$ process, only the (unitarity violating) amplitudes for the s -channel Higgs resonance diagrams are known.⁴²⁾ Furthermore, the $\mathcal{O}(\alpha_s^3)$ K -factor has not been computed, and we make the conservative choice, $K = 1$ for the gluon fusion process.

The cross sections listed for the $\mathcal{O}(\alpha_W^2 \alpha_s^n)$ processes are only an estimate of the $ZZ + n_C$ central jet rates. Since the tree level $\mathcal{O}(\alpha_W^2 \alpha_s^n)$, $n \geq 1$, rates diverge for $p_{Tj} \rightarrow 0$, the fraction of $ZZ + n$ jet events from these sources containing m jets with $p_{Tj} > 100$ GeV and $n - m$ soft unidentified jets and which would therefore contribute to the $ZZ + m$ jet rate cannot be calculated. The $\mathcal{O}(\alpha_s)$ K -factor, which we use to account for these corrections, represents an approximate treatment of these contributions for the $ZZ + 0$ jet case. For a more reliable prediction, it is necessary to compute the full $\mathcal{O}(\alpha_W^2 \alpha_s^n)$ $pp \rightarrow ZZ + X$ rate including n -loop virtual corrections and to combine them with the soft and collinear singularities present in the tree level (and m -loop, $m < n$) matrix elements. Finally, we have also disregarded the small contributions to the $ZZ + 0, 1$ central jet rates arising from $\mathcal{O}(\alpha_W^2 \alpha_s)$ and $\mathcal{O}(\alpha_W^2 \alpha_s^2)$ processes with one or more jets in the $|\eta_j| > 2.5$ region.

Table 3 demonstrates that the perturbative ‘no-resonance’ background from the non-resonant diagrams is small, for a Higgs boson with $m_H = 0.5$ TeV, for both gluon fusion and $qq \rightarrow qqZZ$. Furthermore, the $q\bar{q} \rightarrow ZZ$ background doesn’t pose a serious problem. The size of the Higgs boson signal, $\sigma_H - \sigma_B$, from $qq \rightarrow qqZZ$ decreases with increasing number of central jets. As expected from Fig. 11, the electroweak signal to background ratio $(\sigma_H - \sigma_B)/\sigma_B$ decreases from 10.7 (12.2) to 3.6 (3.5) to 0.7 (0.5) as n_C increases from 0 to 1 to 2 at the LHC (SSC). On the other hand, the $\mathcal{O}(\alpha_W^2 \alpha_s^n)$ background decreases fairly linearly with increasing n_C . Finally, we note that cross sections at the LHC are significantly smaller than at the SSC.

The size of the various background cross sections increases substantially with m_H , due mainly to the large width of the Higgs boson which dilutes the peak and spreads the signal over a large m_{ZZ} range. This is illustrated for $m_H = 1$ TeV in Table 4. The situation is particularly unfavourable for the LHC, where the total background cross section for the $ZZ + 0$ jet channel in the resonance region is about a factor 9 larger than the combined signal from gluon and vector boson fusion. We also see that the $\mathcal{O}(\alpha_W^4)$ $ZZ + 2$ central jet cross section is completely dominated by the non-resonant diagrams at both the LHC and the SSC.

The cross section of the gluon fusion process depends significantly on the top quark mass. For the value used in Tables 3 and 4, $m_t = 120$ GeV, gluon fusion is the dominant source of Higgs bosons in the $ZZ + 0$ jet channel for $m_H = 0.5$ TeV. Vector boson fusion, however, gains in importance with increasing m_H , and becomes competitive with gluon fusion at $m_H \approx 1$ TeV (see Fig. 6). It is worth noting that for heavy Higgs bosons, the size of the Higgs boson signal, $\sigma_H - \sigma_B$, in $gg \rightarrow ZZ$ turns out to be about a factor 2 – 3 larger than the rate one would obtain from the s -channel Higgs exchange graph $gg \rightarrow H \rightarrow ZZ$ alone. This indicates that the net interference effects between the non-resonant diagrams and the s -channel Higgs pole graph are strong and positive.⁸⁾ Although the box and triangle contributions interfere destructively when $m_{ZZ} \gg m_H$, for $m_{ZZ} \leq m_H$, where the cross section is largest, the interference is constructive.

In the range of Higgs boson masses we are considering, $m_H \geq 0.5$ TeV, the

$gg \rightarrow ZZ$ cross section grows with m_t in the resonance region. For $m_t < 120$ GeV, $qq \rightarrow qqZZ$ would play a more important role, and, for top quark masses close the present lower limit of $m_t \approx 80$ GeV, would be the dominant source of Higgs bosons with mass of $\mathcal{O}(1 \text{ TeV})$. On the other hand, if m_t is significantly larger than 120 GeV, gluon fusion would dominate Higgs boson production for all masses m_H up to $\mathcal{O}(1 \text{ TeV})$. The cross sections of the $\mathcal{O}(\alpha_s^3)$ and $\mathcal{O}(\alpha_s^4)$ processes cannot be calculated at present, but from naive α_s power counting one would expect that they are larger than the ZZj and $ZZjj$ rates from the $\mathcal{O}(\alpha_W^4)$ reaction $qq \rightarrow qqZZ$.

Tables 3 and 4 show that the $pp \rightarrow ZZ + 0 \text{ jet}$ channel is the most promising one to search for the Higgs boson if jet identification in the forward rapidity region $|\eta_j| > 2.5$ is not feasible. Given the projected luminosities for the LHC and SSC, it should be possible to find a Higgs boson of mass $m_H = 0.5 \text{ TeV}$ in the $ZZ + 0 \text{ jet}$ channel with both Z bosons decaying into electrons or muons. For $m_H = 1 \text{ TeV}$, small rates and the relatively larger background present serious problems. It is here where jet identification in the forward jet rapidity region $|\eta_j| > 2.5$ might be useful, since a large fraction of $qq \rightarrow qqZZ$ events with 0 jets in the central region actually contain one or two jets in the forward rapidity region with a large transverse momentum (see Table 2).

Table 5 lists the cross sections for Z pair production in association with 0, 1 and 2 jets with transverse momentum $p_{Tj} > 50 \text{ GeV}$ (100 GeV) in the forward region ($n_F = 0, 1 \text{ or } 2$), and no jets in the central region ($n_C = 0$), for a Higgs boson with $m_H = 1 \text{ TeV}$ in the resonance region at the LHC and the SSC. It is clear that the perturbative background from non-resonant $qq \rightarrow qqZZ$ diagrams, as well as the background from QCD processes, is small for $(n_C, n_F) = (0, 1)$ or $(0, 2)$. This result is, of course, expected from Figs. 11 and 15: the non-resonant $qq \rightarrow qqZZ$ diagrams and the mixed QCD-electroweak processes result in a more central η_j distribution than s -channel Higgs pole diagrams do.

Cross sections for jets in the forward rapidity region at the LHC are about one order of magnitude smaller than at SSC energies. On the other hand, the ratio of the Higgs signal to the background from processes involving QCD is considerably more favourable at the LHC, due to the smaller rapidity range covered. It is

also clear that the cross sections for observing at least one jet with a transverse momentum $p_{Tj} > 100$ GeV are very small, in particular for the LHC. For a lower threshold of $p_{Tj} > 50$ GeV, rates are significantly higher and may be observable. In particular, when the (0,1) and (0,2) channels, which show the most favourable signal to background ratio, are combined, a statistically significant Higgs boson signal may arise. Provided, of course, that a $p_{Tj} > 50$ GeV cut is sufficient to eliminate the ‘spill-in’ from the underlying event. Existing studies,³⁷⁾ indicate that this is so, especially since jets originating from $qq \rightarrow qqZZ$ are typically almost back-to-back and very energetic. Such jets will, therefore, be very localized in the azimuthal direction ϕ , in contrast to the energy deposited by the underlying event.³⁷⁾

If jet identification in the rapidity range $|\eta_j| > 2.5$ is possible at the LHC or SSC, the cleanest signal of a Higgs boson with $m_H \approx 1$ TeV is expected in the $(n_C, n_F) = (0, 1)$ and $(0, 2)$ channels.* Although the rates are small, the Higgs boson signal in these channels may well be more significant than in the $ZZ + 0$ jet case with jet identification in the central region, due to the smallness of the background from $\mathcal{O}(\alpha_W^2 \alpha_s^n)$ processes. Higgs boson events in the (0,1) and (0,2) channels, although rare, would be quite spectacular: Two charged lepton pairs in the central detector with an invariant mass close to M_Z , accompanied by one or two, almost back-to-back, very energetic jets with large rapidities.

4.3 DOUBLE PARTON SCATTERING AND EVENT PILEUP

Since the cross sections for $(n_C, n_F) = (0, 1)$ and $(0, 2)$ are rather small, very high luminosities are required to accumulate a sufficient number of events. These large luminosities pose special problems. First of all, detectors have to be built which can survive the high radiation level present in this case. Secondly, new backgrounds from double parton scattering and event pileup arise. We now study these backgrounds for $pp \rightarrow ZZjj$ for $m_H = 1$ TeV with both jets in the forward

* The rapidity distribution of the jets in the $\mathcal{O}(\alpha_s^{2+n})$ processes should be similar to that for the $\mathcal{O}(\alpha_W^2 \alpha_s^n)$ reactions. Contributions from these processes to the Higgs boson signal in the (0,1) and (0,2) channels are thus expected to be small and, in any case, would improve the situation.

rapidity region. This channel has the smallest cross section, which makes it the most sensitive to additional background sources.

There are three processes which could result in $ZZjj$ through double parton scattering or event pileup: $Z \oplus Zjj$, $Zj \oplus Zj$ and $ZZ \oplus jj$ production. In the first process, $Z \oplus Zjj$, a single Z -boson and a Zjj event are generated during one beam crossing. Since the singly produced Z typically has a small p_T , it is difficult for this process to mimick a $ZZjj$ event resulting from a Higgs boson decay where both Z 's usually have a large transverse momentum (see Fig. 8). The same is also the case for $Zj \oplus Zj$. Here the transverse momentum of each Z is balanced by one of the jets, which, in general, is not the case for $ZZjj$ events originating from Higgs boson decay. $ZZ \oplus jj$, on the other hand, can more easily be misinterpreted as a Higgs boson event: the two jets are back-to-back, and so are the Z bosons. The same configuration tends to occur in Higgs boson events, although there the Z pair has a $p_T \sim \mathcal{O}(M_W)$, whereas p_{TZZ} should be small in $ZZ \oplus jj$ pileup events.

In the following we, therefore, focus on the $ZZ \oplus jj$ process. The cross sections for double scattering, σ_{DS} , is given in a simple order of magnitude estimate by,⁴³⁾

$$\sigma_{DS}(ZZ \oplus jj) \sim \frac{1}{\sigma_0} \sigma(ZZ) \sigma(jj) , \quad (4.3)$$

where σ_0 is a flux factor for two partons inside the same nucleon which is of the order of the total inelastic cross section. For $|y_Z| < 2.5$, $m_H - \Gamma_H < m_{ZZ} < m_H + \Gamma_H$, $|\eta_j| > 2.5$ and $p_{Tj} > 50$ GeV, and $\sigma_0 = 40$ mb, we find $\sigma_{DS}(ZZ \oplus jj) = 3.6 \cdot 10^{-5}$ pb ($7.8 \cdot 10^{-4}$ pb) at the LHC (SSC), about two orders of magnitude smaller than the Higgs boson signal cross section (see Table 5). If the p_{Tj} cut is increased to 100 GeV, σ_{DS} drops by about a factor 20.

The background cross section from event pileup depends explicitly on the luminosity and the time spacing Δt between bunches, and $1/\sigma_0$ in (4.3) should be replaced by the luminosity per bunch crossing. If we assume a luminosity of $\mathcal{L} = 10^{33} \text{ cm}^{-2}\text{s}^{-1}$ and $\Delta t = 25$ ns for the SSC,⁴⁴⁾ we find a $ZZ \oplus jj$ cross section from event pileup which is slightly larger than the numbers quoted above. For the LHC, a high luminosity option with $\mathcal{L} = 4 \cdot 10^{34} \text{ cm}^{-2}\text{s}^{-1}$ and $\Delta t = 15$ ns⁴⁴⁾ is

seriously considered. With these parameters, we obtain a cross section of $9 \cdot 10^{-4}$ pb for $ZZ \oplus jj$ from the pileup of ZZ and 2-jet events, which is about 20% of the Higgs boson signal (see Table 5). In view of the large uncertainties associated with our estimate, we conclude that the pileup of events might be a non-negligible background at the LHC which needs to be studied more thoroughly.

5. Summary and Conclusions

In this paper, we have presented the results of a complete perturbative calculation of Z boson pair production via the $\mathcal{O}(\alpha_W^4)$ electroweak process $qq \rightarrow qqZZ$, including the $\mathcal{O}(\alpha_W^2 \alpha_s^2)$ background reactions. Compact analytic expressions for the helicity amplitudes, including the subsequent decay of the Z bosons into massless fermions, were derived. Those amplitudes were then used for a detailed study of the event characteristics and jet activity in $qq \rightarrow qqZZ$, particularly in the Higgs boson resonance region. The results obtained with the exact matrix elements were compared with the effective W approximation and the Higgs pole approximation.

The effective W approximation turns out to accurately describe the Z pair invariant mass distribution in the Higgs boson resonance region. However, due to ambiguities in the Q^2 scale used in the transversely polarised vector boson structure function, the prediction for the m_{ZZ} distribution outside the resonance region is not reliable (see Fig. 5). Furthermore, since the original $2 \rightarrow 4$ reaction is replaced by a $2 \rightarrow 2$ vector boson scattering process many interesting quantities, like the jet transverse momentum, cannot be predicted in this approximation. On the other hand, the effective W approximation may be useful in estimating cross sections in models where the electroweak sector is strongly interacting, and where the dominant contribution comes from the scattering of longitudinally polarised vector bosons.

The Higgs pole approximation was found to be of quite limited use only, especially for a heavy Higgs boson with $m_H \approx 1$ TeV where $qq \rightarrow qqZZ$ is most important as a Higgs boson source. It shows a ‘bad’ high energy behaviour and, in general, does not faithfully describe the quantities characterizing $qq \rightarrow qqZZ$ events. In particular, the m_{ZZ} distribution in the resonance region is significantly different from the exact result for heavy Higgs bosons (see Fig. 4). Of course,

the main reason for this discrepancy is the cancellation of the unitarity violating contributions of the Higgs pole diagrams by the non-resonant diagrams. We have tried to estimate the remaining non-resonant contribution using the perturbative ‘no-resonance’ approximation, in which the exact matrix elements are used with $m_H \sim 0$. This corresponds to a weakly interacting electroweak sector and, in many ways, represents the minimum possible $qq \rightarrow qqZZ$ cross section.

Our results indicate that $qq \rightarrow qqZZ$ events have a rather large jet activity and, depending on the jet definition, frequently result in one or two high p_T jets in either the central or the forward rapidity region, although a sizeable fraction of events contain no jets. For these event topologies, $ZZ + n$ jet production, where $n = 0, 1, 2$, via $\mathcal{O}(\alpha_W^2 \alpha_s^n)$ mixed QCD-electroweak processes provides a potentially dangerous background. We have studied the $ZZ + 2$ jet background in detail and found that a jet pseudorapidity cut of $|\eta_j| > 2.5$, a jet-jet invariant mass cut of $m_{jj} > 1.5$ TeV, or a jet-jet separation cut of $\Delta R_{jj} > 4$ can drastically reduce this background compared to the signal.

We can also ask whether or not being able to identify jets improves the Higgs boson signal. This is, of course, most important for heavy Higgs bosons where the $qq \rightarrow qqZZ$ process is relatively more important. First of all, if jet identification is only possible in the central region, then for $m_H = 500$ GeV (and $m_t = 120$ GeV), we expect ^{*} 2146 (208) no-jet ‘gold-plated’ $pp \rightarrow ZZ \rightarrow \ell^+ \ell^- \ell'^+ \ell'^-$ events in the Higgs resonance region at the LHC (SSC) compared to 1005 (68) in the absence of the Higgs boson (see Table 3). From this we conclude that it should be possible to observe a 500 GeV Higgs boson at either the SSC or LHC, even if the proposed high luminosity option is not possible at the LHC.

On the other hand, for the illustrative case of $m_H = 1$ TeV, we expect 1244 (102) no-jet ‘gold-plated’ $pp \rightarrow ZZ \rightarrow \ell^+ \ell^- \ell'^+ \ell'^-$ events in the resonance region at the LHC (SSC) compared to 1118 (80) without the Higgs (see Table 4). Clearly, to observe the Higgs boson in this channel requires a very precise knowledge of the

^{*} We assume a yearly integrated luminosity of $4 \cdot 10^5$ pb⁻¹ at the LHC and 10^4 pb⁻¹ at the SSC and a running time of one year. Furthermore, we assume each Z decays into either muons or electrons with a branching ratio of 0.066 and that the leptons are identified with 100% efficiency.

background, especially at the LHC. With increasing numbers of jets in the central region, the signal to background gets worse, although we should point out that the $\mathcal{O}(\alpha_s^3)$ and $\mathcal{O}(\alpha_s^4)$ signal and background rates have not been computed and could conceivably change this conclusion.

Finally, if jets can be identified in the forward region, $|\eta_j| > 2.5$, then for $p_{Tj} > 50$ GeV, we expect 61 (12) $qq \rightarrow qqZZ \rightarrow qq\ell^+\ell^-\ell'^+\ell'^-$ events containing one or more forward jets and no jets in the central region in the presence of a 1 TeV Higgs boson at the LHC (SSC) compared to 40 (7) events otherwise (see Table. 5). The signal to background is much improved, however, by restricting ourselves to jets in the forward region, the signal is also reduced, primarily because the gluon fusion contribution has not been computed in this region. As shown in Table 2, if no jets are observed in the central region, requiring one or two jets in the forward region only reduces the signal by 32%. Lowering the jet p_T cut can reduce the amount of signal lost, however, this would then lead to greater difficulty in disentangling the jet from the underlying event.

It has to be emphasised that, although the event rate in this channel is small, the events are spectacular: One or two, almost back-to-back, very energetic jets at large rapidities accompanied by the leptonic decay products of two Z bosons in the central region. It is also clear that it is vital to have as high a luminosity as possible to have any chance of observing an $\mathcal{O}(1$ TeV) Higgs boson in this channel. However, such a high luminosity may also have adverse effects, such as event pile-up and double parton scattering. Our simple estimates of these effects indicate that this is not a severe problem for the $ZZjj$ channel, however, further investigations into the feasibility of doing experiments in a high luminosity environment are certainly warranted.

ACKNOWLEDGEMENTS

We would like to thank W. Giele, M. Golden, F. Halzen and D. Morris for stimulating discussions. We are grateful to T. Han for his help in comparing our results with Ref. 18. We also thank W. Long for his support in enabling our FORTRAN program to run on a UNIX workstation. This research was supported in part by the University of Wisconsin Research Committee with funds granted by the Wisconsin Alumni Research Foundation, and in part by the U. S. Department of Energy under contract DE-AC02-76ER00881.

REFERENCES

1. D. Decamp *et al.* (ALEPH Collaboration), CERN-EP/90-16 preprint (January 1990) and Phys. Lett. **236B**, 233 (1990);
M. Z. Akrawy *et al.* (OPAL Collaboration), Phys. Lett. **236B**, 224 (1990).
2. For a review see *e.g.* : J. F. Gunion, H. E. Haber, G. L. Kane and S. Dawson, UCD-89-4, SCIPP-89/13, BNL-41644 preprint (June 1989).
3. M. Drees *et al.* , Proceedings of the Workshop *Z* Physics at LEP 1, CERN 89-08, Vol. 2, p. 58 (1989), and references therein.
4. See *e.g.* S. L. Wu *et al.* in *Proceedings of the ECFA Workshop on LEP200*, Volume II, Aachen, Germany, 29 September - 1 October 1986, CERN 87-08, p. 312 and references therein.
5. J. F. Gunion, G. L. Kane and J. Wudka, Nucl. Phys. **B299**, 231 (1988).
6. H. Georgi, S. L. Glashow, M. E. Mahacek and D. V. Nanopoulos, Phys. Rev. Lett. **40**, 692 (1978).
7. D. A. Dicus, C. Kao and W. W. Repko, Phys. Rev. **D36**, 1570 (1987);
8. E. W. N. Glover and J. J. van der Bij, Phys. Lett. **219B**, 488 (1989), and Nucl. Phys. **B321**, 561 (1989).
9. R. N. Cahn and S. Dawson, Phys. Lett. **136B**, 196 (1984), Phys. Lett. **138B**, 464(E) (1984);
S. Dawson, Nucl. Phys. **B249**, 42 (1984);
G. L. Kane, W. W. Repko and W. B. Rolnick, Phys. Lett. **148B**, 367 (1984).
10. A. Abbasabadi and W. W. Repko, Nucl. Phys. **B292**, 461 (1987), and Phys. Rev. **D37**, 2668 (1988).
11. F. Abe *et al.* (CDF Collaboration), Phys. Rev. Lett. **64**, 142 (1990);
F. Abe *et al.* (CDF Collaboration), Phys. Rev. Lett. **64**, 147 (1990).
12. R. N. Cahn, S. D. Ellis, R. Kleiss and W. J. Stirling, Phys. Rev. **D35**, 1626 (1987).
13. R. Kleiss and W. J. Stirling, Phys. Lett. **200B**, 193 (1988).

14. V. Barger, T. Han and R. J. N. Phillips, Phys. Rev. **D37**, 2005 (1988).
15. V. Barger, T. Han and R. J. N. Phillips, Phys. Lett. **206B**, 339 (1988), and Phys. Rev. **D36**, 295 (1987).
16. G. Altarelli, B. Mele and F. Pitolli, Nucl. Phys. **B287**, 205 (1987).
17. R. Kleiss and W. J. Stirling, Phys. Lett. **182B**, 75 (1986).
18. V. Barger, T. Han, J. Ohnemus and D. Zeppenfeld, Phys. Rev. **D41**, 2782 (1990).
19. D. A. Dicus, S. L. Wilson and R. Vega, Phys. Lett. **192B**, 231 (1987).
20. R. Kleiss and W. J. Stirling, Nucl. Phys. **B262**, 235 (1985);
J. F. Gunion and Z. Kunszt, Phys. Lett. **161B**, 333 (1985).
21. Particle Data Group, Phys. Lett. **204B**, 1 (1988).
22. G. S. Abrams *et al.* (MARK II Collaboration), Phys. Rev. Lett. **63**, 724 (1989).
23. B. Adeva *et al.* (L3 Collaboration), Phys. Lett. **231B**, 509 (1989);
D. Decamp *et al.* (ALEPH Collaboration), Phys. Lett. **231B**, 519 (1989);
M. Z. Akrawy *et al.* (OPAL Collaboration), Phys. Lett. **231B**, 530 (1989);
P. Aarnio *et al.* (DELPHI Collaboration), Phys. Lett. **231B**, 539 (1989).
24. F. Abe *et al.* (CDF Collaboration), Phys. Rev. Lett. **63**, 720 (1989).
25. D. Duke and J. Owens, Phys. Rev. **D30**, 49 (1984).
26. M. S. Chanowitz and M. K. Gaillard, Nucl. Phys. **B261**, 379 (1985).
27. J. Lindfors, Z. Phys. **C28**, 427 (1985).
28. W. B. Rolnick, Nucl. Phys. **B274**, 171 (1986).
29. A. Abbasabadi and W. W. Repko, Phys. Rev. **D36**, 289 (1987).
30. R. M. Godbole and S. D. Rindani, Phys. Lett. **190B**, 192 (1987), and Z. Phys. **C36**, 395 (1987).
31. P. W. Johnson, F. I. Olness and W.-K. Tung, Phys. Rev. **D36**, 291 (1987).
32. Z. Kunszt and D. E. Soper, Nucl. Phys. **B296**, 253 (1988).

33. A. Abbasabadi and W. W. Repko, in *Proceedings of the Summer Study on High Energy Physics in the 1990's*, Snowmass, Colorado, 1988, p. 154.
34. B. W. Lee, C. Quigg and H. B. Thacker, Phys. Rev. **D16**, 1519 (1977), and Phys. Rev. Lett. **38**, 883 (1977).
35. A. Abbasabadi, W. W. Repko, D. A. Dicus and R. Vega, Phys. Rev. **D38**, 2770 (1988).
36. M. J. Duncan, Phys. Lett. **179B**, 393 (1986).
37. W. J. Stirling, CERN 88-02 report (1988) ed. J. H. Mulvey, p. 67.
38. M. J. Duncan, G. Kane and W. W. Repko, Nucl. Phys. **B272**, 517 (1986).
39. T. Åkesson *et al.*, CERN 88-02 report (1988) ed. J. H. Mulvey, p. 1.
40. U. Baur, E. W. N. Glover and J. J. van der Bij, Nucl. Phys. **B318**, 106 (1989).
41. V. Barger, J. L. Lopez and W. Putikka, Int. J. Mod. Phys. **A3**, 2181 (1988).
42. R. K. Ellis, I. Hinchliffe, M. Soldate and J. J. van der Bij, Nucl. Phys. **B297**, 221 (1988);
U. Baur and E. W. N. Glover, FERMILAB-PUB-89/243-T, MAD/PH/547 preprint, (December 1989), Nucl. Phys. B in print.
43. N. Paver and D. Treleani, Z. Phys. **C28**, 187 (1985);
R. M. Godbole, S. Gupta and J. Lindfors, HU-TFT-89-36 preprint (October 1989).
44. B. Richter, in *Proceedings of the XXIV Int. Conf. on High Energy Physics*, Munich, August 4 – 10, 1988, R. Kotthaus and J. H. Kühn (Eds.), p. 422.

TABLE 1

Fraction of events with $m_H - \Gamma_H < m_{ZZ} < m_H + \Gamma_H$ in $qq \rightarrow qqZZ$ for $m_H = 0.5$ TeV at (a) the LHC and (b) the SSC having 0, 1 and 2 jets with a transverse momentum $p_{Tj} > 50$ GeV ($p_{Tj} > 100$ GeV) in either the central ($|\eta_j| < 2.5$) or the forward ($|\eta_j| > 2.5$) jet pseudorapidity region. The last row shows the inclusive fraction of events with 0, 1 and 2 jets in the central pseudorapidity region. A Z boson rapidity cut of $|y_Z| < 2.5$ and a jet-jet separation cut $\Delta R_{jj} > 0.7$ is imposed.

a) LHC ($\sqrt{s} = 16$ TeV)

	number of jets	$ \eta_j < 2.5$		
		0	1	2
$ \eta_j > 2.5$	0	0.16 (0.51)	0.25 (0.25)	0.11 (0.048)
	1	0.20 (0.13)	0.21 (0.053)	–
	2	0.084 (0.009)	–	–
inclusive		0.44 (0.65)	0.45 (0.31)	0.11 (0.048)

b) SSC ($\sqrt{s} = 40$ TeV)

	number of jets	$ \eta_j < 2.5$		
		0	1	2
$ \eta_j > 2.5$	0	0.14 (0.47)	0.19 (0.21)	0.065 (0.031)
	1	0.24 (0.20)	0.23 (0.073)	–
	2	0.14 (0.026)	–	–
inclusive		0.52 (0.69)	0.42 (0.28)	0.065 (0.031)

TABLE 2

Fraction of events with $m_H - \Gamma_H < m_{ZZ} < m_H + \Gamma_H$ in $qq \rightarrow qqZZ$ for $m_H = 1$ TeV at (a) the LHC and (b) the SSC having 0, 1 and 2 jets with a transverse momentum $p_{Tj} > 50$ GeV ($p_{Tj} > 100$ GeV) in either the central ($|\eta_j| < 2.5$) or the forward ($|\eta_j| > 2.5$) jet pseudorapidity region. The last row shows the inclusive fraction of events with 0, 1 and 2 jets in the central pseudorapidity region. A Z boson rapidity cut of $|y_Z| < 2.5$ and a jet-jet separation cut $\Delta R_{jj} > 0.7$ is imposed.

a) LHC ($\sqrt{s} = 16$ TeV)

	number of jets	$ \eta_j < 2.5$		
		0	1	2
$ \eta_j > 2.5$	0	0.12 (0.39)	0.21 (0.25)	0.18 (0.12)
	1	0.16 (0.14)	0.24 (0.10)	–
	2	0.095 (0.014)	–	–
inclusive		0.37 (0.54)	0.45 (0.35)	0.18 (0.12)

b) SSC ($\sqrt{s} = 40$ TeV)

	number of jets	$ \eta_j < 2.5$		
		0	1	2
$ \eta_j > 2.5$	0	0.10 (0.36)	0.14 (0.19)	0.10 (0.067)
	1	0.21 (0.20)	0.26 (0.13)	–
	2	0.18 (0.050)	–	–
inclusive		0.49 (0.61)	0.40 (0.32)	0.10 (0.067)

TABLE 3

Cross sections for Z pair production in association with n_C central ($|\eta_j| < 2.5$) jets with a transverse momentum $p_{Tj} > 100$ GeV from various sources for a Higgs boson with mass $m_H = 0.5$ TeV in the resonance region ($m_H - \Gamma_H < m_{ZZ} < m_H + \Gamma_H$) at the LHC and the SSC. The perturbative ‘no-resonance’ cross section is given in brackets. Both Z bosons are required to have a rapidity $|y_Z| < 2.5$. Furthermore, a Z -jet separation cut $\Delta R_{Zj} > 0.7$ and a jet-jet separation cut $\Delta R_{jj} > 0.7$ is imposed wherever applicable. For the top quark mass we used $m_t = 120$ GeV.

a) LHC ($\sqrt{s} = 16$ TeV, σ [pb])

n_C	$\mathcal{O}(\alpha_s^{2+n})$	$\mathcal{O}(\alpha_W^4)$	$\mathcal{O}(\alpha_W^2 \alpha_s^n)$
0	0.66 (0.080)	0.082 (0.007)	0.49 (0.49)
1	–	0.037 (0.008)	0.086 (0.086)
2	–	0.005 (0.003)	0.021 (0.021)

b) SSC ($\sqrt{s} = 40$ TeV, σ [pb])

n_C	$\mathcal{O}(\alpha_s^{2+n})$	$\mathcal{O}(\alpha_W^4)$	$\mathcal{O}(\alpha_W^2 \alpha_s^n)$
0	3.17 (0.37)	0.45 (0.034)	1.15 (1.15)
1	–	0.18 (0.040)	0.32 (0.32)
2	–	0.018 (0.012)	0.10 (0.10)

TABLE 4

Cross sections for Z pair production in association with n_C central ($|\eta_j| < 2.5$) jets with a transverse momentum $p_{Tj} > 100$ GeV from various sources for a Higgs boson with mass $m_H = 1$ TeV in the resonance region ($m_H - \Gamma_H < m_{ZZ} < m_H + \Gamma_H$) at the LHC and the SSC. The perturbative ‘no-resonance’ cross section is given in brackets. Both Z bosons are required to have a rapidity $|y_Z| < 2.5$. Furthermore, a Z -jet separation cut $\Delta R_{Zj} > 0.7$ and a jet-jet separation cut $\Delta R_{jj} > 0.7$ is imposed wherever applicable. For the top quark mass we used $m_t = 120$ GeV.

a) LHC ($\sqrt{s} = 16$ TeV, σ [pb])

n_C	$\mathcal{O}(\alpha_s^{2+n})$	$\mathcal{O}(\alpha_W^4)$	$\mathcal{O}(\alpha_W^2 \alpha_s^n)$
0	0.12 (0.071)	0.034 (0.011)	0.56 (0.56)
1	–	0.021 (0.013)	0.12 (0.12)
2	–	0.0064 (0.0059)	0.033 (0.033)

b) SSC ($\sqrt{s} = 40$ TeV, σ [pb])

n_C	$\mathcal{O}(\alpha_s^{2+n})$	$\mathcal{O}(\alpha_W^4)$	$\mathcal{O}(\alpha_W^2 \alpha_s^n)$
0	0.70 (0.38)	0.26 (0.069)	1.39 (1.39)
1	–	0.13 (0.079)	0.51 (0.51)
2	–	0.025 (0.023)	0.18 (0.18)

TABLE 5

Cross sections for Z pair production in association with n_F jets of transverse momentum $p_{Tj} > 50$ GeV (100 GeV) in the forward region ($|\eta_j| > 2.5$) and no jets in the central region ($|\eta_j| < 2.5$), $n_C = 0$, from various sources for a Higgs boson with mass $m_H = 1$ TeV in the resonance region ($m_H - \Gamma_H < m_{ZZ} < m_H + \Gamma_H$) at the LHC and the SSC. The perturbative ‘no-resonance’ cross section is given in brackets. Both Z bosons are required to have a rapidity $|y_Z| < 2.5$. Furthermore, a jet-jet separation cut $\Delta R_{jj} > 0.7$ is imposed if 2 jets are observed.

a) LHC ($\sqrt{s} = 16$ TeV, σ [pb])

	$p_{Tj} > 50$ GeV		$p_{Tj} > 100$ GeV	
(n_C, n_F)	$\mathcal{O}(\alpha_W^4)$	$\mathcal{O}(\alpha_W^2 \alpha_s^n)$	$\mathcal{O}(\alpha_W^4)$	$\mathcal{O}(\alpha_W^2 \alpha_s^n)$
(0,0)	0.007 (0.001)	0.56 (0.56)	0.024 (0.007)	0.56 (0.56)
(0,1)	0.010 (0.002)	0.018 (0.018)	0.0085 (0.0035)	0.0054 (0.0054)
(0,2)	0.006 (0.002)	0.001 (0.001)	0.0009 (0.0005)	0.0001 (0.0001)

b) SSC ($\sqrt{s} = 40$ TeV), σ [pb])

	$p_{Tj} > 50$ GeV		$p_{Tj} > 100$ GeV	
(n_C, n_F)	$\mathcal{O}(\alpha_W^4)$	$\mathcal{O}(\alpha_W^2 \alpha_s^n)$	$\mathcal{O}(\alpha_W^4)$	$\mathcal{O}(\alpha_W^2 \alpha_s^n)$
(0,0)	0.042 (0.004)	1.39 (1.39)	0.151 (0.026)	1.39 (1.39)
(0,1)	0.090 (0.016)	0.105 (0.105)	0.086 (0.030)	0.049 (0.049)
(0,2)	0.075 (0.027)	0.011 (0.011)	0.021 (0.013)	0.003 (0.003)

FIGURE CAPTIONS

1. Topologically distinct Feynman diagrams contributing to the process $qq \rightarrow qqZZ$, including the subsequent decay of the Z bosons into massless fermion-antifermion final states. Photon and gluon exchange only contribute in diagrams (a) and (b), while the Z boson can be exchanged in diagrams (a), (b) and (c). W exchange contributes to all diagram topologies.
2. Topologically distinct Feynman graphs contributing to $gg \rightarrow q\bar{q}ZZ$, including the subsequent decay of the Z bosons into massless fermion-antifermion final states.
3. Jet-jet invariant mass distribution, $d\sigma/dm_{jj}$, for $Z + \gamma$ exchange graphs (solid line) and W exchange diagrams (dashed line) in $qq \rightarrow qqZZ$ for pp collisions at $\sqrt{s} = 40$ TeV. Both final state Z bosons are required to have rapidity $|y_Z| < 2.5$, while a separation cut of $\Delta R_{jj} > 0.7$ is imposed on the jets.
4. Invariant mass distribution, $d\sigma/dm_{ZZ}$, of the Z boson pair in $qq \rightarrow qqZZ$ for a Higgs boson of mass (a) $m_H = 0.5$ TeV, (b) $m_H = 1$ TeV at the LHC, and (c) $m_H = 0.5$ TeV and (d) $m_H = 1$ TeV at the SSC. Both Z bosons are required to have rapidity $|y_Z| < 2.5$ and a separation cut of $\Delta R_{jj} > 0.7$ is imposed on the jets. The solid line shows the full electroweak result, while the dashed curve represents the contribution of $Z + \gamma$ exchange diagrams. The dotted line gives the result obtained from the s -channel Higgs pole diagrams, while the dash-dotted curve shows the ZZ invariant mass distribution obtained in the effective W approximation in the Higgs resonance region.
5. Z boson pair invariant mass spectrum, $d\sigma/dm_{ZZ}$, for Higgs boson production in pp collisions at $\sqrt{s} = 40$ TeV in the effective W approximation when both exchanged vector bosons are longitudinally polarised (LL), and when at least one is transversely polarised (TT+TL). A rapidity cut of $|y_Z| < 2.5$ is imposed on the Z bosons. The Higgs boson mass is $m_H = 0.5$ TeV. The solid (dotted) lines show the cross section for $Q^2 = m_{ZZ}^2$ ($Q^2 = m_{ZZ}^2/4$).
6. Z boson pair invariant mass spectrum, $d\sigma/dm_{ZZ}$, for $qq \rightarrow qqZZ$ (solid line), $gg \rightarrow ZZ$ (dash-dotted line) and $q\bar{q} \rightarrow ZZ$ (dotted line) at (a) the LHC and

(b) the SSC, for $m_H = 1$ TeV. A rapidity cut of $|y_Z| < 2.5$ is imposed on the final state Z bosons. The top quark mass used to compute the $gg \rightarrow ZZ$ cross section is $m_t = 120$ GeV. A $\Delta R_{jj} > 0.7$ cut is applied in the $qq \rightarrow qqZZ$ case.

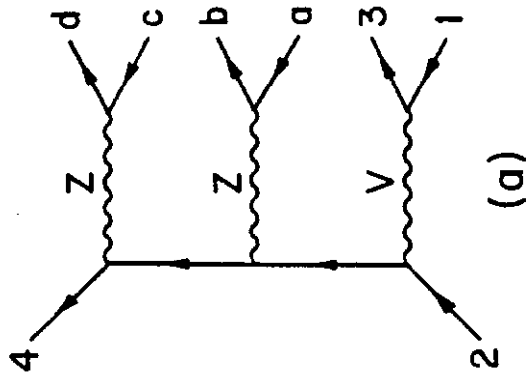
7. Transverse momentum spectrum, $d\sigma/dp_{TZZ}$, of the Z boson pair in $qq \rightarrow qqZZ$ for $m_H = 1$ TeV at the SSC. The solid curve shows the exact result integrated over the full m_{ZZ} range, while the dashed curve gives $d\sigma/dp_{TZZ}$ for the resonance region, $m_H - \Gamma_H < m_{ZZ} < m_H + \Gamma_H$. The dotted line represents the ZZ transverse momentum distribution for the Higgs pole approximation in the resonance region. Finally, the dash-dotted curve shows the analytic approximate form of the p_{TZZ} distribution derived in Ref. 12. A rapidity cut of $|y_Z| < 2.5$ is imposed on the Z bosons, while the jets are required to have a separation $\Delta R_{jj} > 0.7$.
8. Distributions of (a) the maximum and (b) the minimum transverse momentum of the Z bosons in $qq \rightarrow qqZZ$ for $m_H = 0.5$ TeV at the SSC. The solid and short-dashed line show the exact result integrated over the full m_{ZZ} range and the resonance region, respectively. The long-dashed line gives the result in the ‘no-resonance’ approximation, while the dotted and dash-dotted lines represent the result obtained for the Higgs pole and effective W approximations in the resonance region. A rapidity cut of $|y_Z| < 2.5$ is imposed on the Z bosons and the jets are required to have a separation $\Delta R_{jj} > 0.7$.
9. Distribution of the maximum Z boson rapidity, $d\sigma/d|y_Z^H|$, for $m_H = 1$ TeV at the SSC. The solid and short-dashed line show the exact result integrated over the full m_{ZZ} range and the resonance region, respectively. The long-dashed line gives the result in the ‘no-resonance’ approximation, while the dotted and dash-dotted lines represent the result obtained for the Higgs pole and effective W approximations in the resonance region. A rapidity cut of $|y_Z| < 2.5$ is imposed on the Z bosons and the jets are required to have a separation $\Delta R_{jj} > 0.7$.
10. Normalised distribution $(1/\sigma) \cdot (d\sigma/d\cos\theta^*)$ of the polar angle of the charged decay lepton from Z decay in $qq \rightarrow qqZZ$ for $m_H = 0.5$ TeV at the SSC. See

text for definition of θ^* . The solid and dashed curve represent the results of the exact calculation with m_{ZZ} integrated over the full range and the resonance region, respectively. The dotted line shows the $\cos \theta^*$ distribution in the Higgs pole approximation, while the dash-dotted line is the result obtained in the ‘no-resonance’ approximation, both in the resonance region. Both Z bosons are required to have rapidity $|y_Z| < 2.5$ and a separation cut of $\Delta R_{jj} > 0.7$ is imposed on the jets.

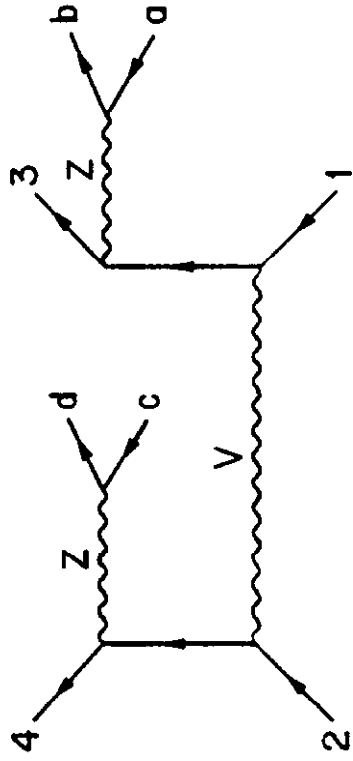
11. Distributions of (a) the maximum and (b) the minimum jet transverse momentum in $qq \rightarrow qqZZ$ for $m_H = 1$ TeV at the SSC. The solid and dashed line show the exact result integrated over the full m_{ZZ} range and the resonance region, respectively. The dash-dotted line gives the result in the ‘no-resonance’ approximation, while the dotted line represents the result obtained in the Higgs pole approximation, both in the resonance region. A rapidity cut of $|y_Z| < 2.5$ is imposed on the Z bosons and the jets are required to have a separation $\Delta R_{jj} > 0.7$.
12. Distributions of (a) the maximum and (b) the minimum jet pseudorapidity for $m_H = 1$ TeV at the SSC. The solid and dashed line show the exact result integrated over the full m_{ZZ} range and the resonance region, respectively. The dash-dotted line gives the result in the ‘no-resonance’ approximation, while the dotted line represents the result obtained in the Higgs pole approximation, both in the resonance region. A rapidity cut of $|y_Z| < 2.5$ is imposed on the Z bosons and the jets are required to have a separation $\Delta R_{jj} > 0.7$.
13. Distribution of the jet-jet separation, ΔR_{jj} , in $qq \rightarrow qqZZ$ for $m_H = 1$ TeV at the SSC. The solid and dashed line show the exact result integrated over the full m_{ZZ} range and the resonance region, respectively. The dash-dotted line gives the result in the ‘no-resonance’ approximation, while the dotted line represents the result obtained in the Higgs pole approximation, both in the resonance region. A rapidity cut of $|y_Z| < 2.5$ is imposed on the Z bosons and the jets are required to have a separation $\Delta R_{jj} > 0.7$.
14. Invariant mass distribution, $d\sigma/dm_{ZZ}$, of the Z boson pair in $pp \rightarrow ZZjj$ at (a) the LHC and (b) the SSC. Both Z bosons are required to have rapidity,

$|y_Z| < 2.5$, while a transverse momentum cut, $p_{Tj} > 100$ GeV, is imposed on the jets. A jet-jet and Z -jet separation of ΔR_{jj} , $\Delta R_{Zj} > 0.7$ is required. The solid line shows the m_{ZZ} spectrum from pure electroweak processes ('vector boson fusion') with $m_H = 1$ TeV, while the dashed line represents the result from mixed QCD-electroweak processes.

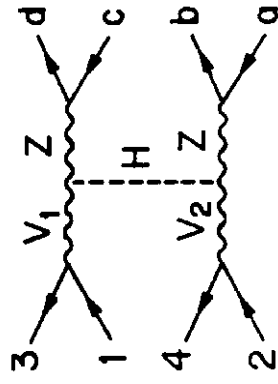
15. Normalised jet pseudorapidity distributions, $(1/\sigma) \cdot (d\sigma/d|\eta_j|)$, in $pp \rightarrow ZZjj$ for (a) the maximum and (b) the minimum jet pseudorapidity at the SSC. Both Z bosons are required to have rapidity, $|y_Z| < 2.5$, while a transverse momentum cut, $p_{Tj} > 100$ GeV, is imposed on the jets. A jet-jet and Z -jet separation of ΔR_{jj} , $\Delta R_{Zj} > 0.7$ is required. The Z pair invariant mass is restricted to the Higgs resonance region, $m_H - \Gamma_H < m_{ZZ} < m_H + \Gamma_H$. The solid line shows the pseudorapidity distribution from pure electroweak processes ('vector boson fusion') with $m_H = 1$ TeV, while the dashed line represents the result from mixed QCD-electroweak processes.
16. Jet-jet invariant mass distribution, $d\sigma/dm_{jj}$, in $pp \rightarrow ZZjj$ at the SSC. Both Z bosons are required to have rapidity, $|y_Z| < 2.5$, while a transverse momentum cut, $p_{Tj} > 100$ GeV is imposed on the jets. A jet-jet and Z -jet separation of ΔR_{jj} , $\Delta R_{Zj} > 0.7$ is required. The Z pair invariant mass is restricted to the Higgs resonance region $m_H - \Gamma_H < m_{ZZ} < m_H + \Gamma_H$. The solid line shows the m_{jj} spectrum from pure electroweak processes ('vector boson fusion') with $m_H = 1$ TeV, while the dashed line represents the result from mixed QCD-electroweak processes.
17. Normalised distribution, $(1/\sigma) \cdot (d\sigma/d\Delta R_{jj})$, of the jet-jet separation ΔR_{jj} in $pp \rightarrow ZZjj$ at the SSC. Both Z bosons are required to have rapidity, $|y_Z| < 2.5$, while a transverse momentum cut, $p_{Tj} > 100$ GeV, is imposed on the jets. A jet-jet and Z -jet separation of ΔR_{jj} , $\Delta R_{Zj} > 0.7$ is required. The Z pair invariant mass is restricted to the Higgs resonance region $m_H - \Gamma_H < m_{ZZ} < m_H + \Gamma_H$. The solid line shows the ΔR_{jj} spectrum from pure electroweak processes ('vector boson fusion') with $m_H = 1$ TeV, while the dashed line represents the result from mixed QCD-electroweak processes.



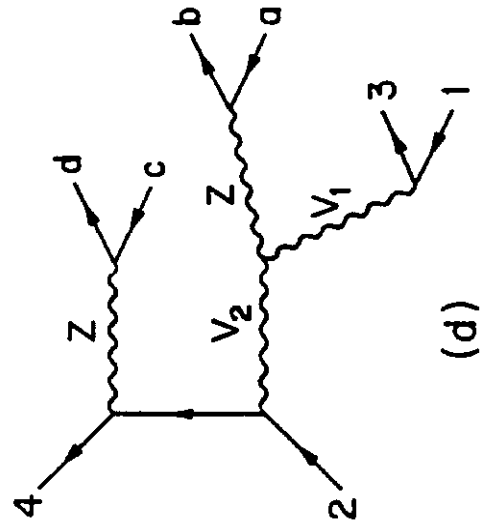
(a)



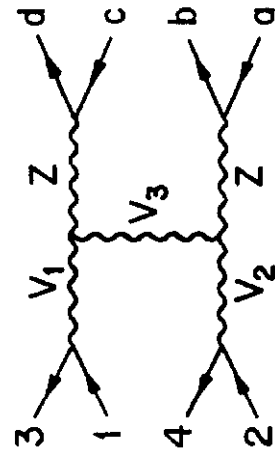
(b)



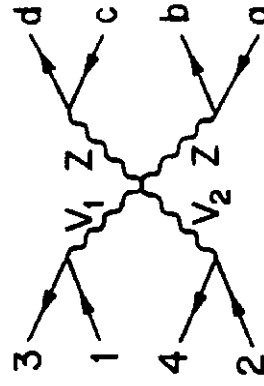
(c)



(d)



(e)



(f)

Fig. 1

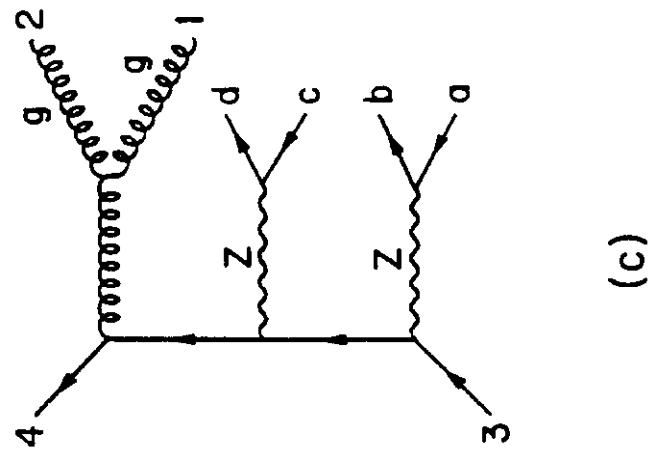
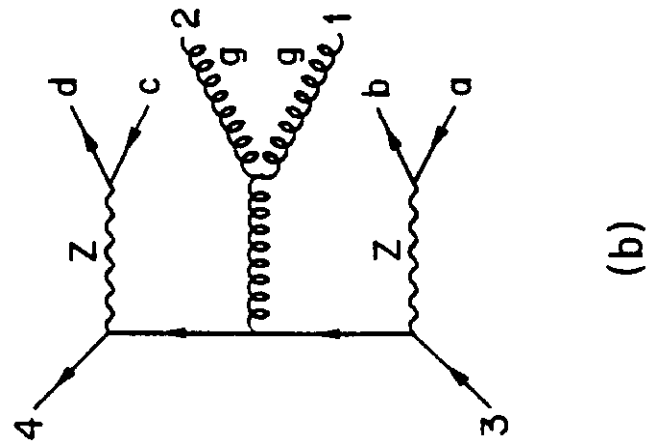
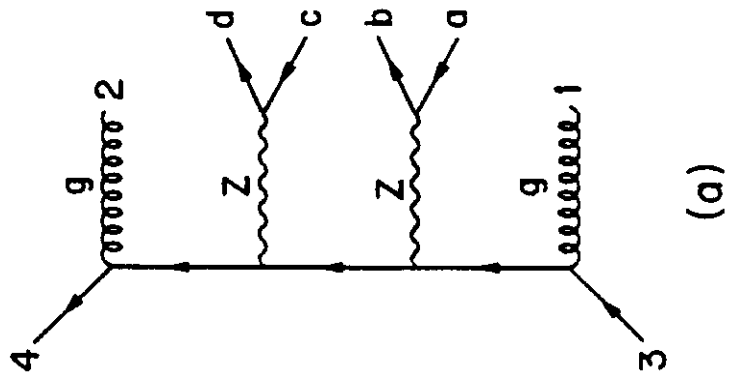


Fig. 2

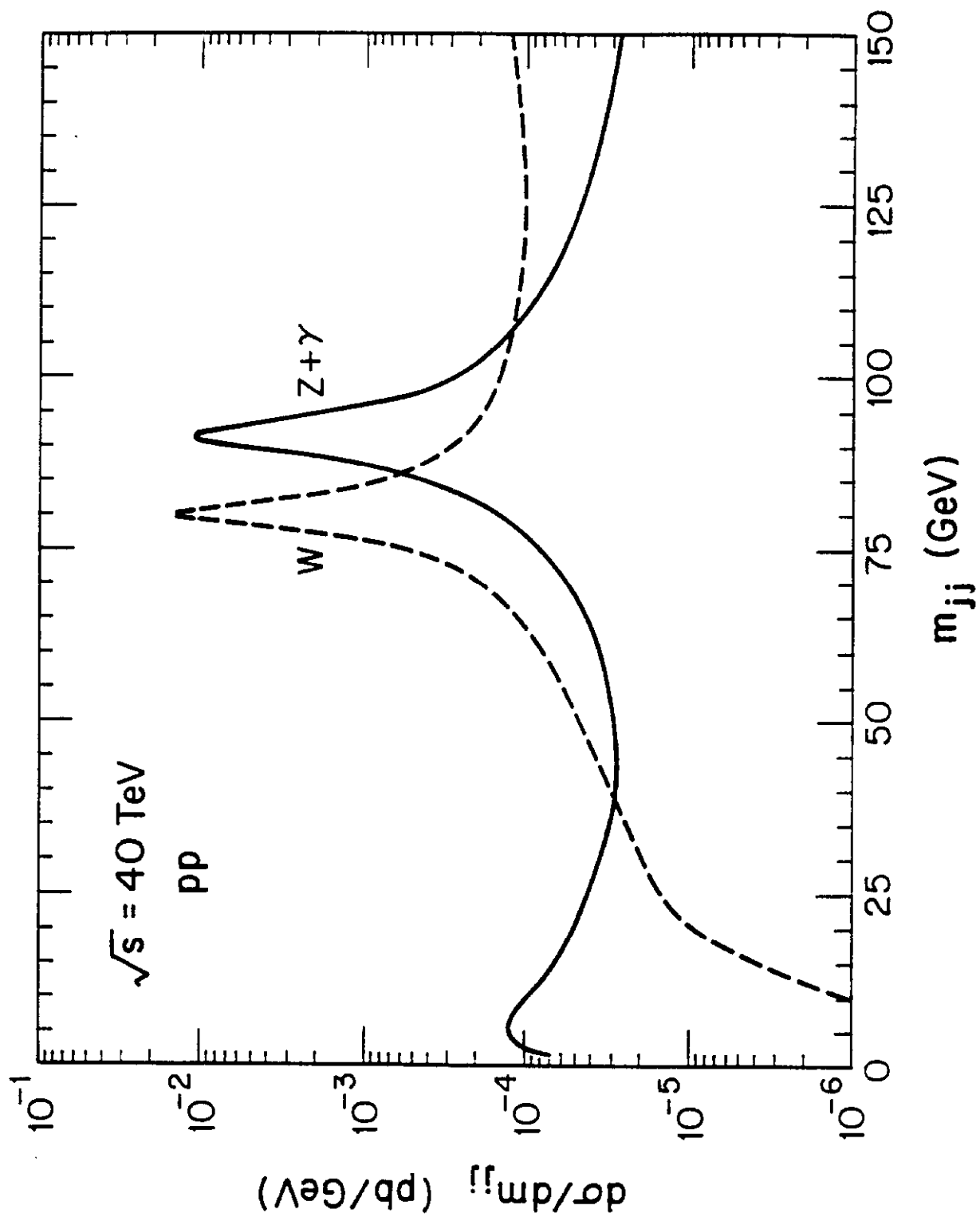


Fig. 3

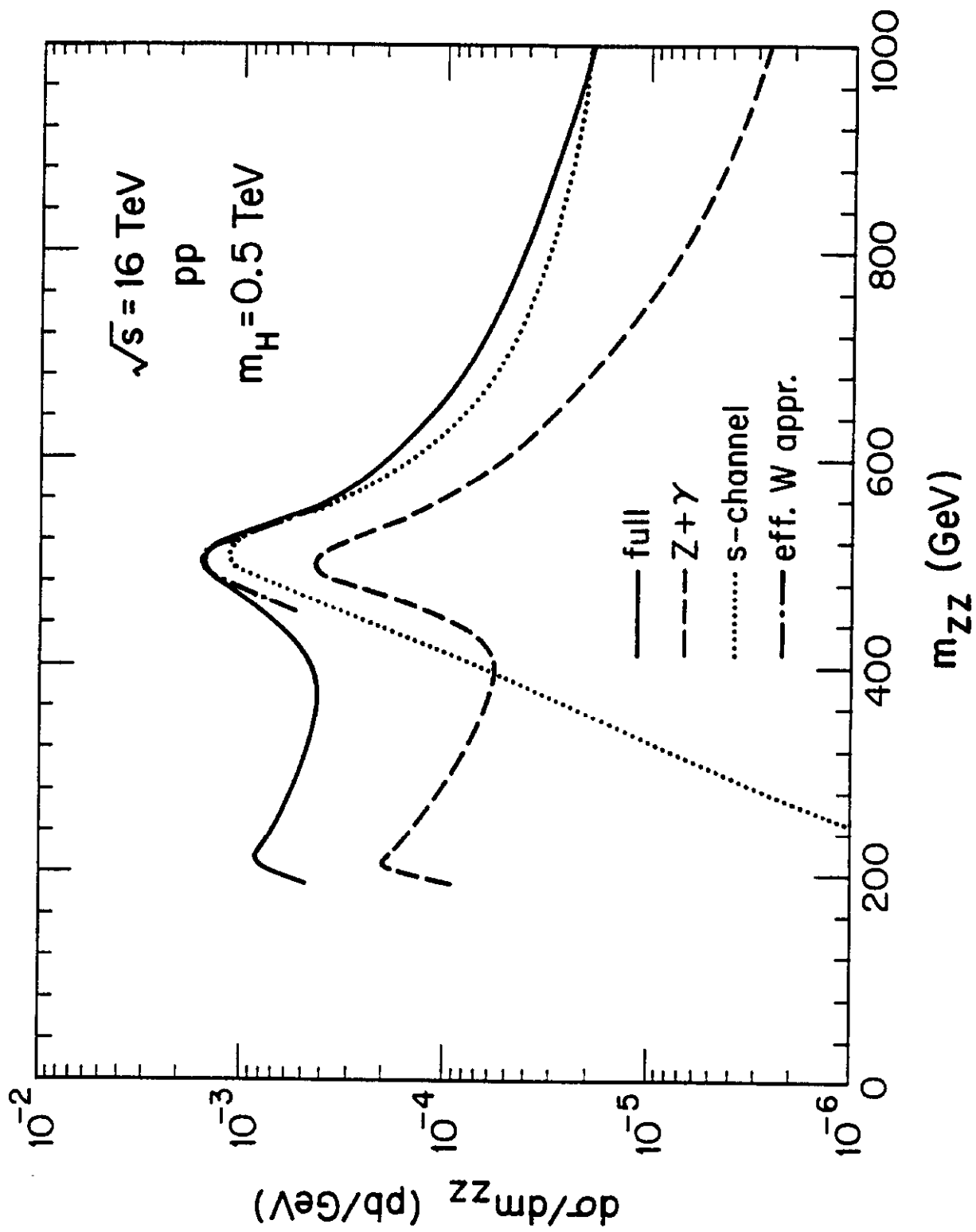


Fig. 4a

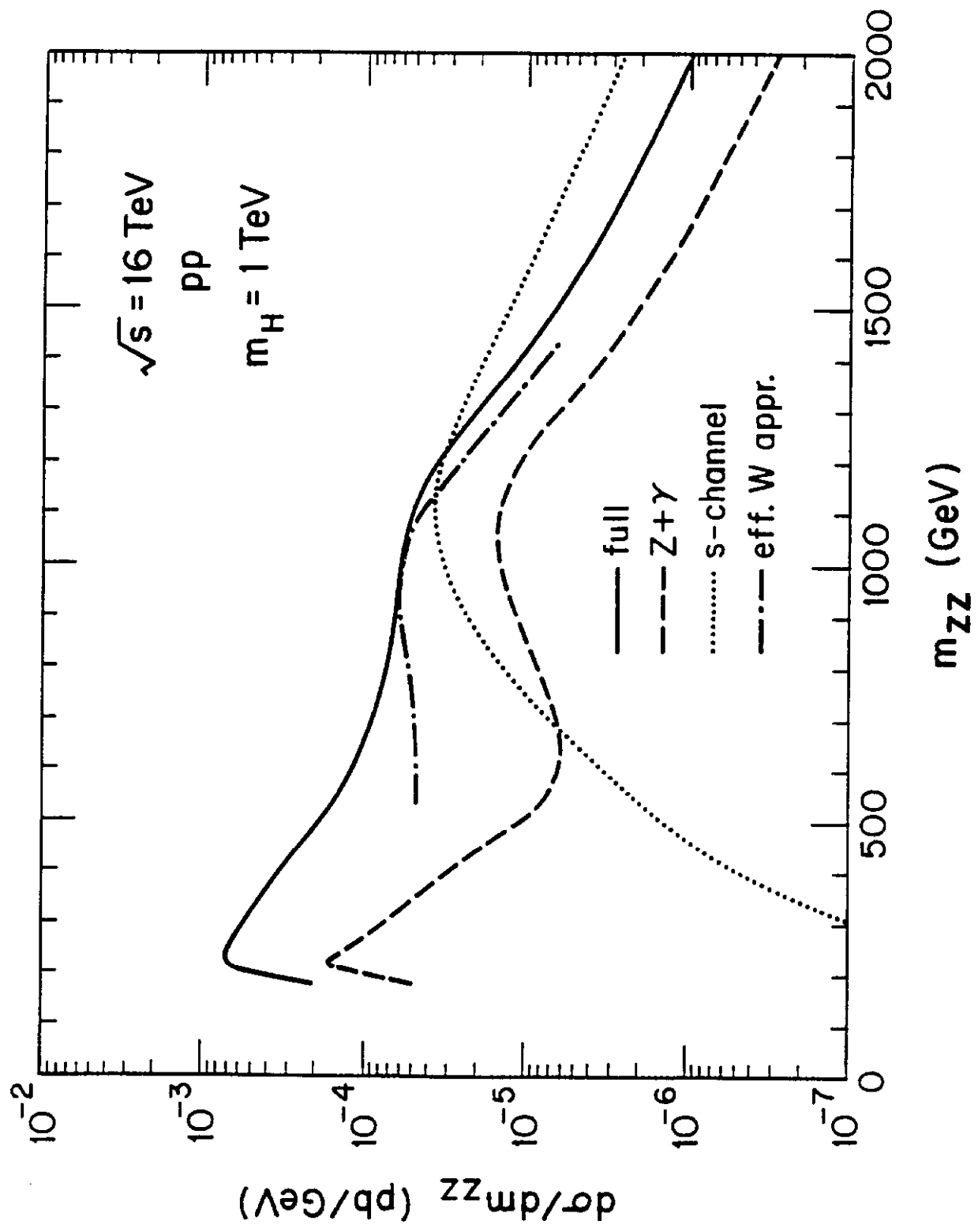


Fig. 4b

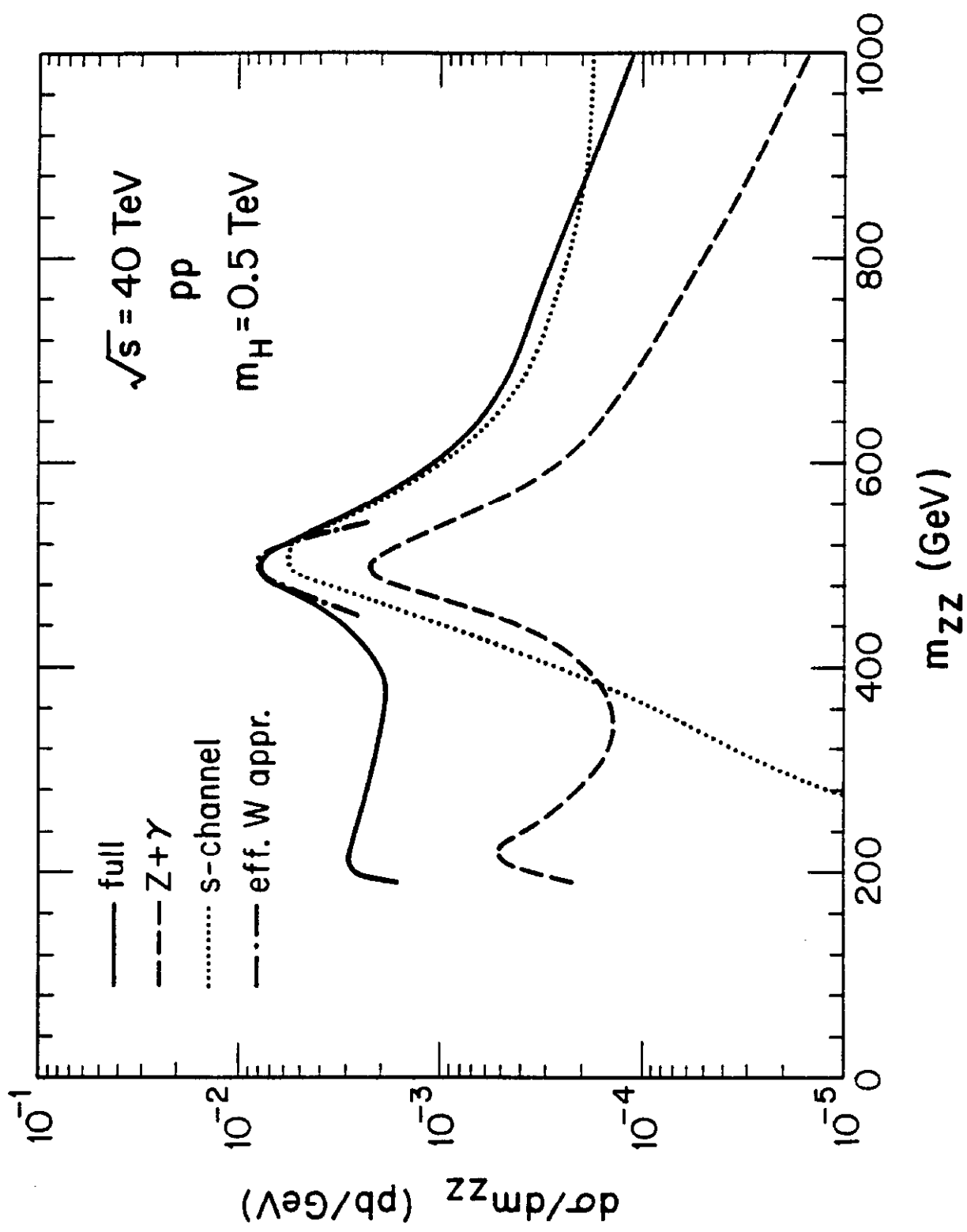


Fig. 4c

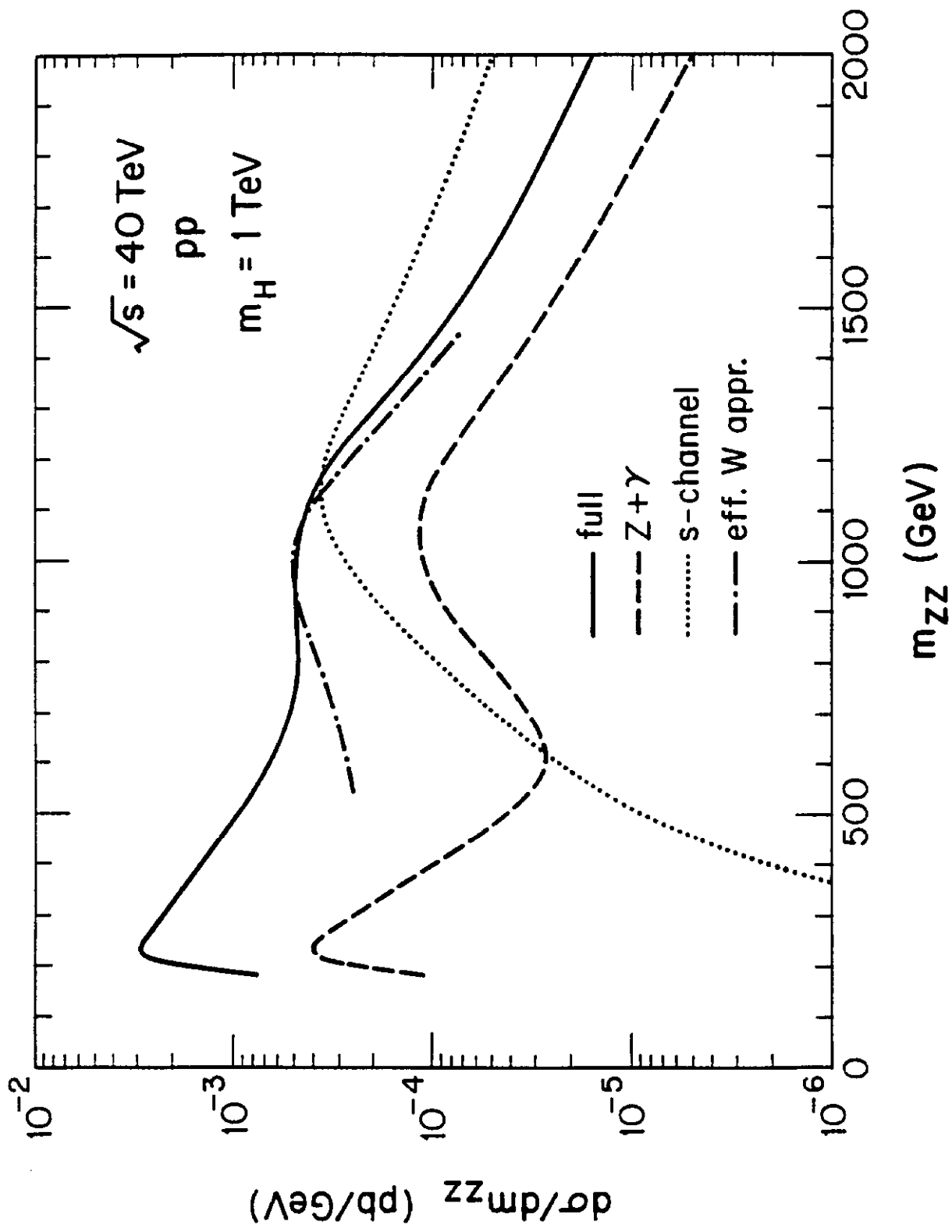


Fig. 4d

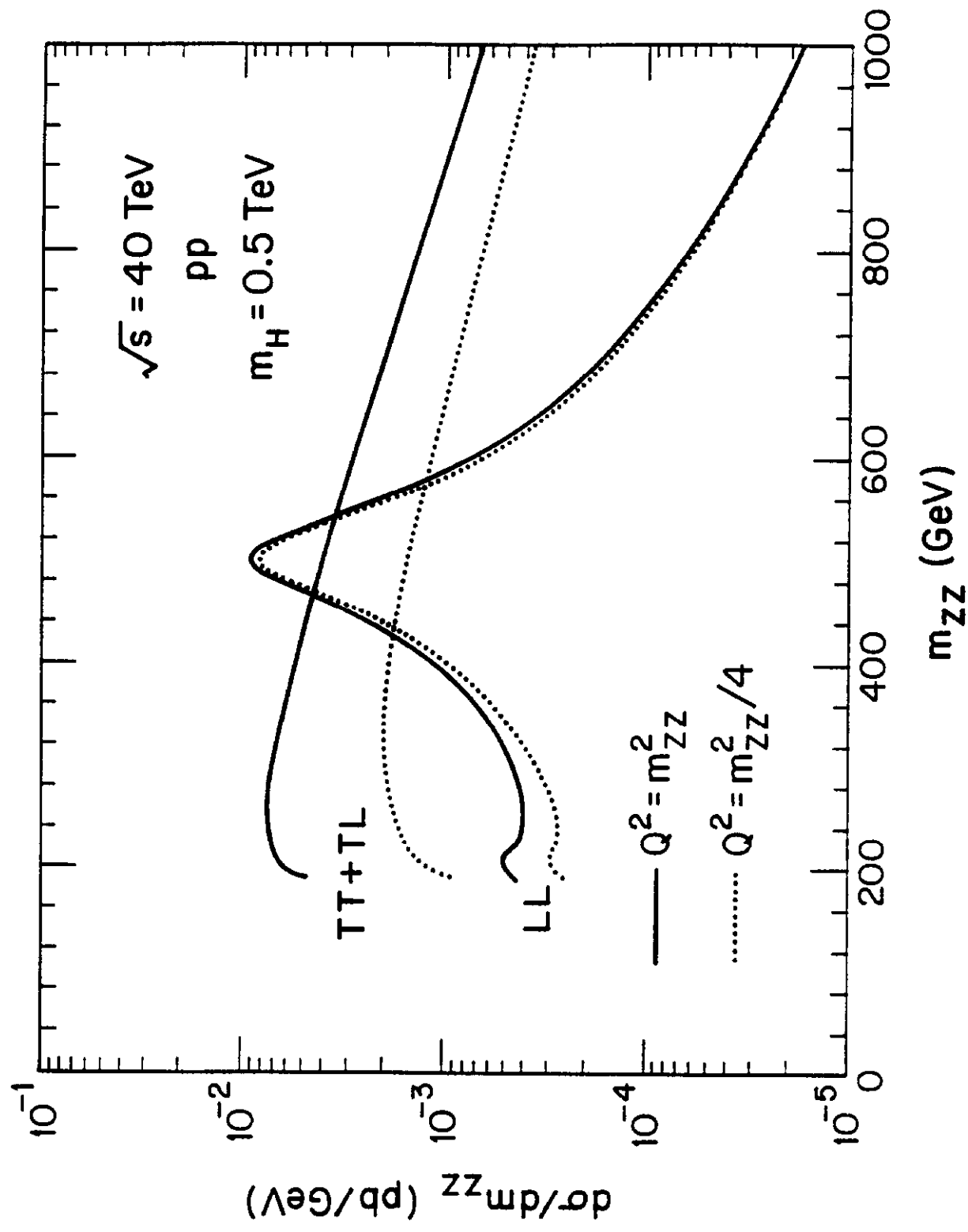


Fig. 5

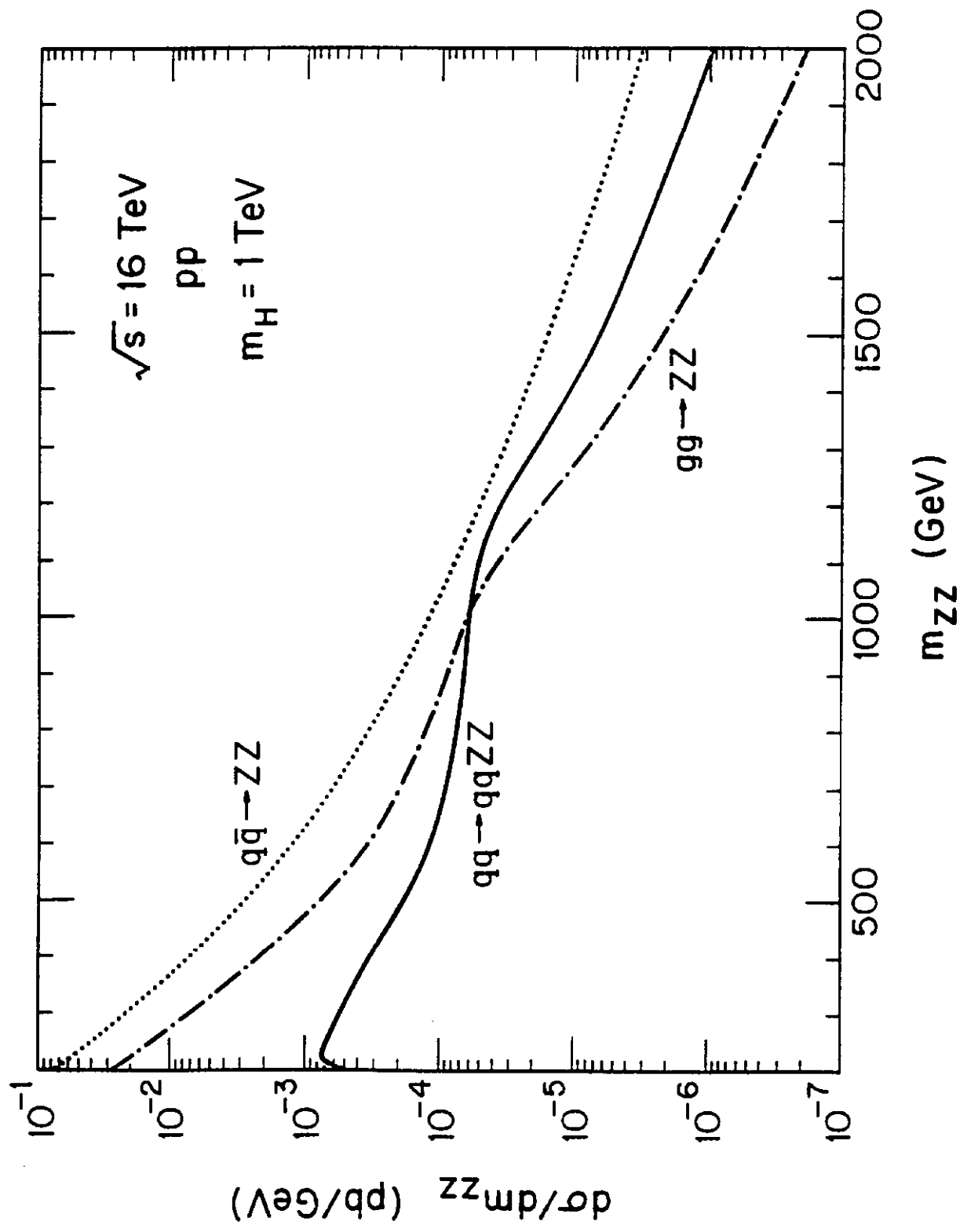


Fig. 6a

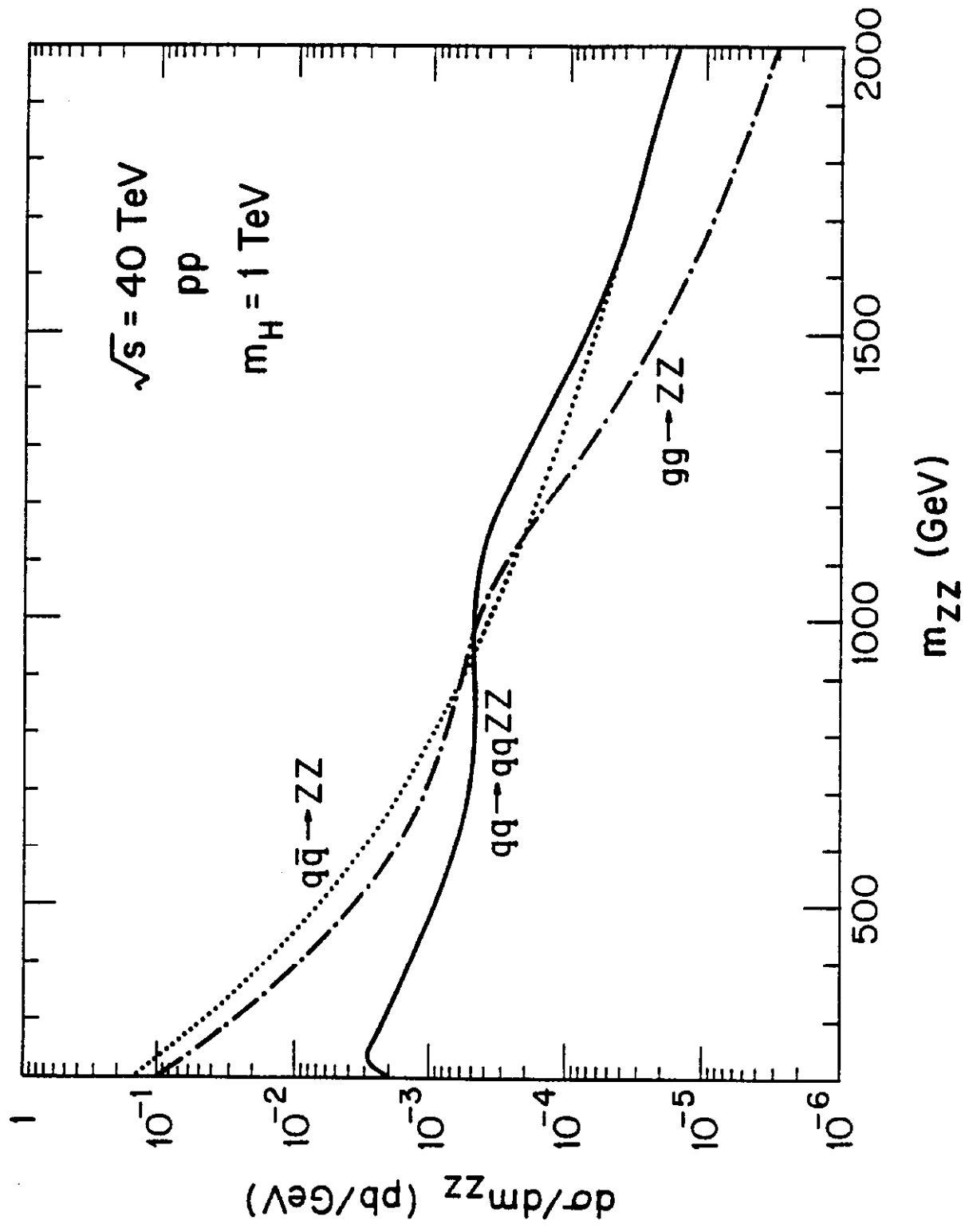


Fig. 6b

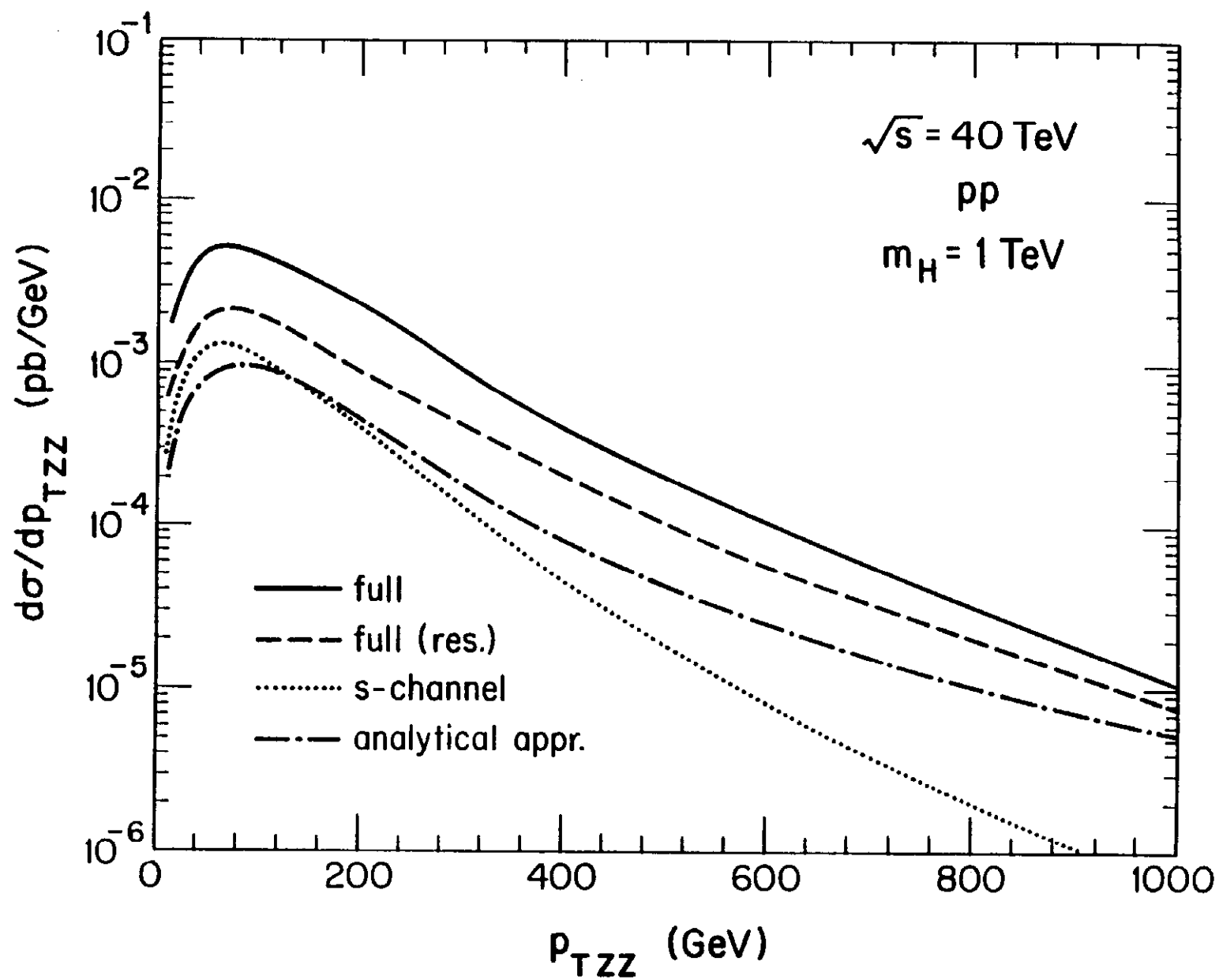


Fig. 7

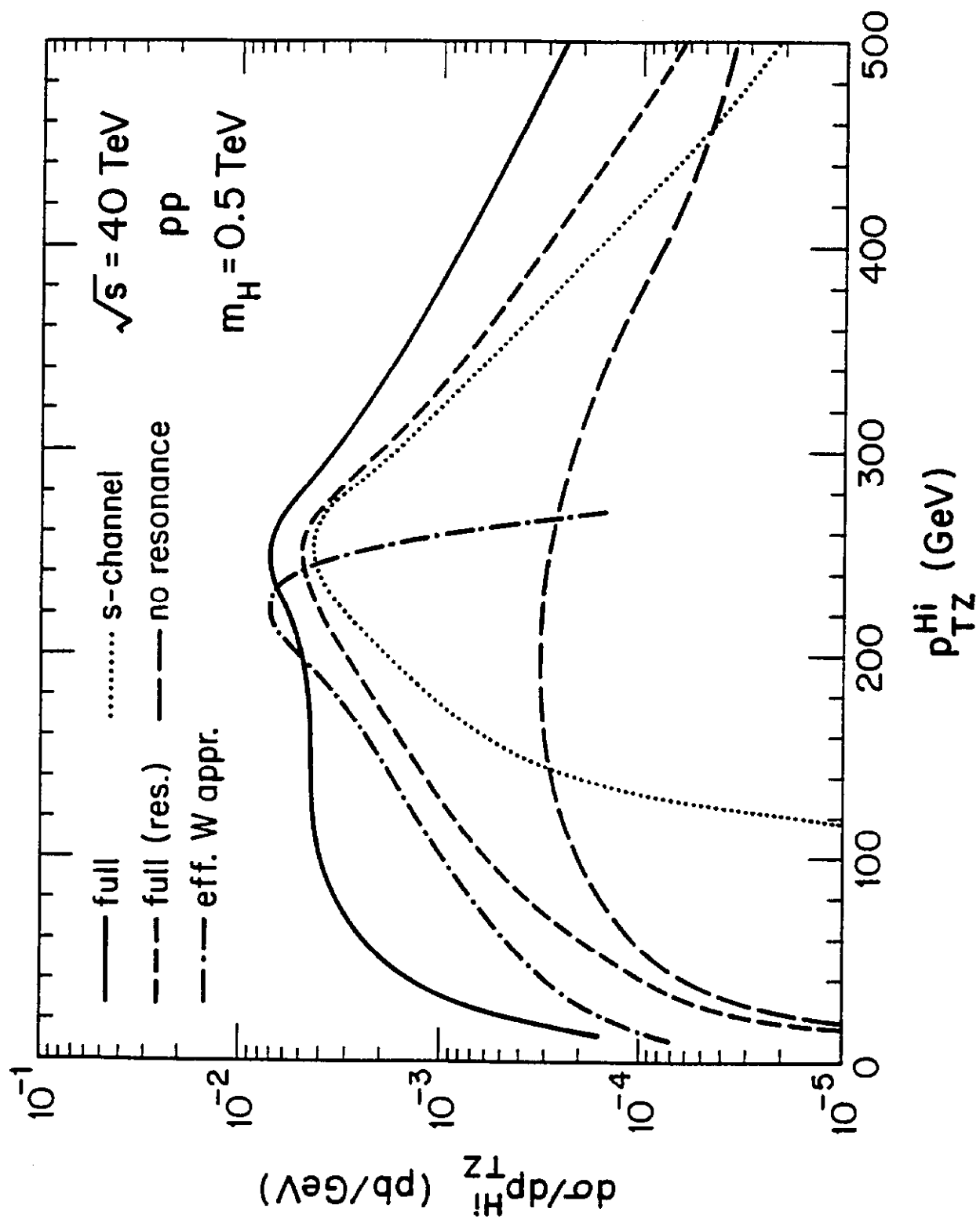


Fig. 8a

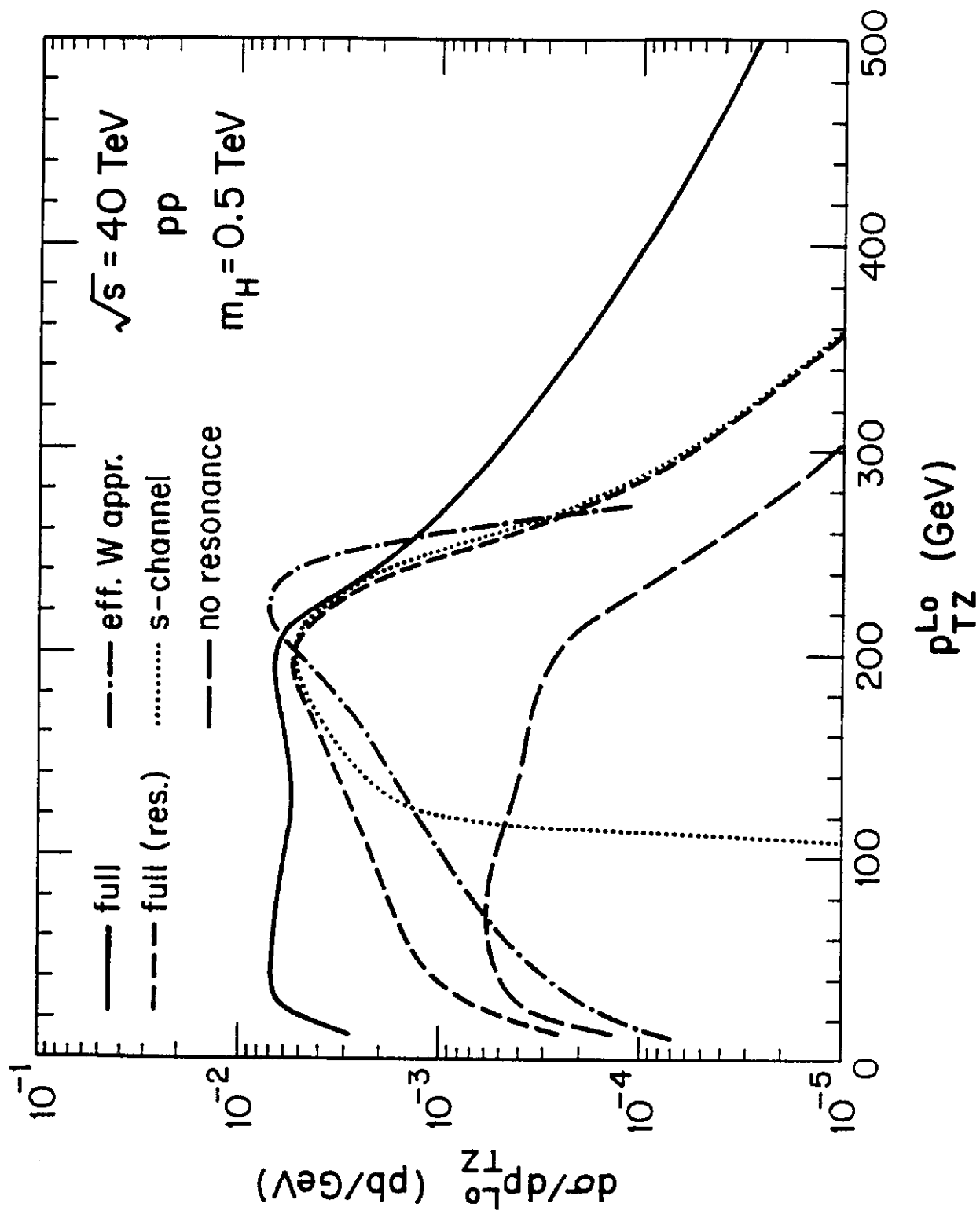


Fig. 8b

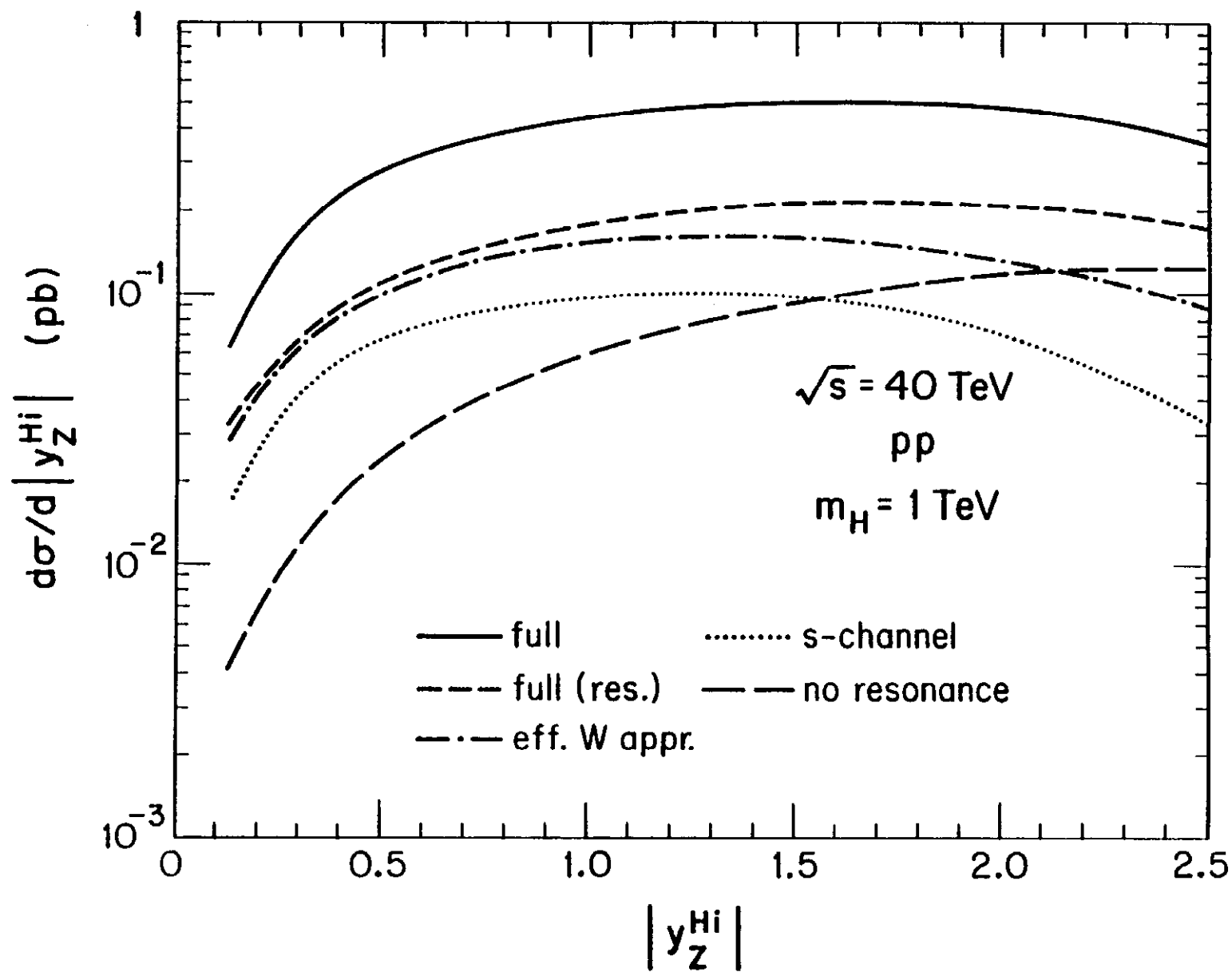


Fig. 9

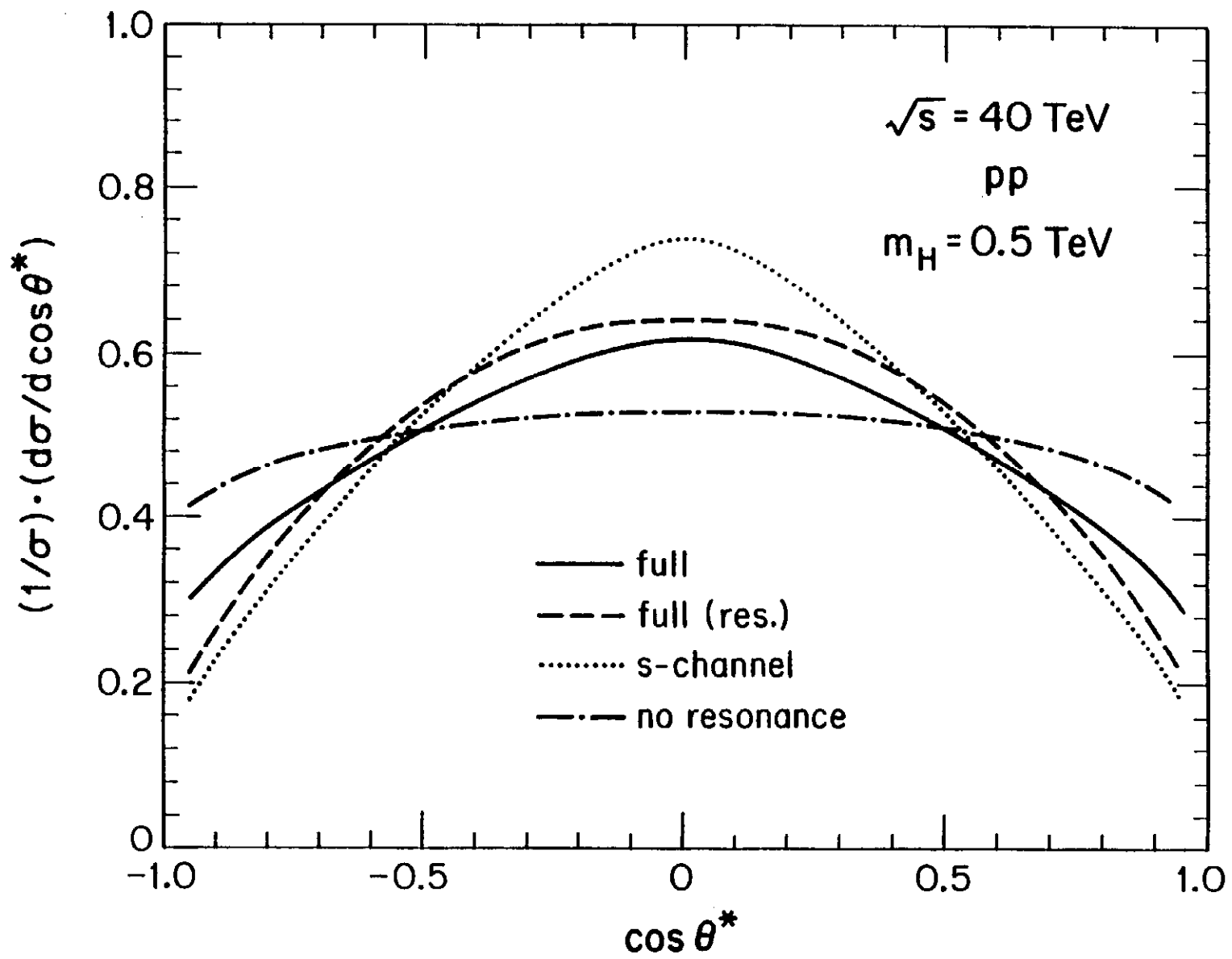


Fig. 10

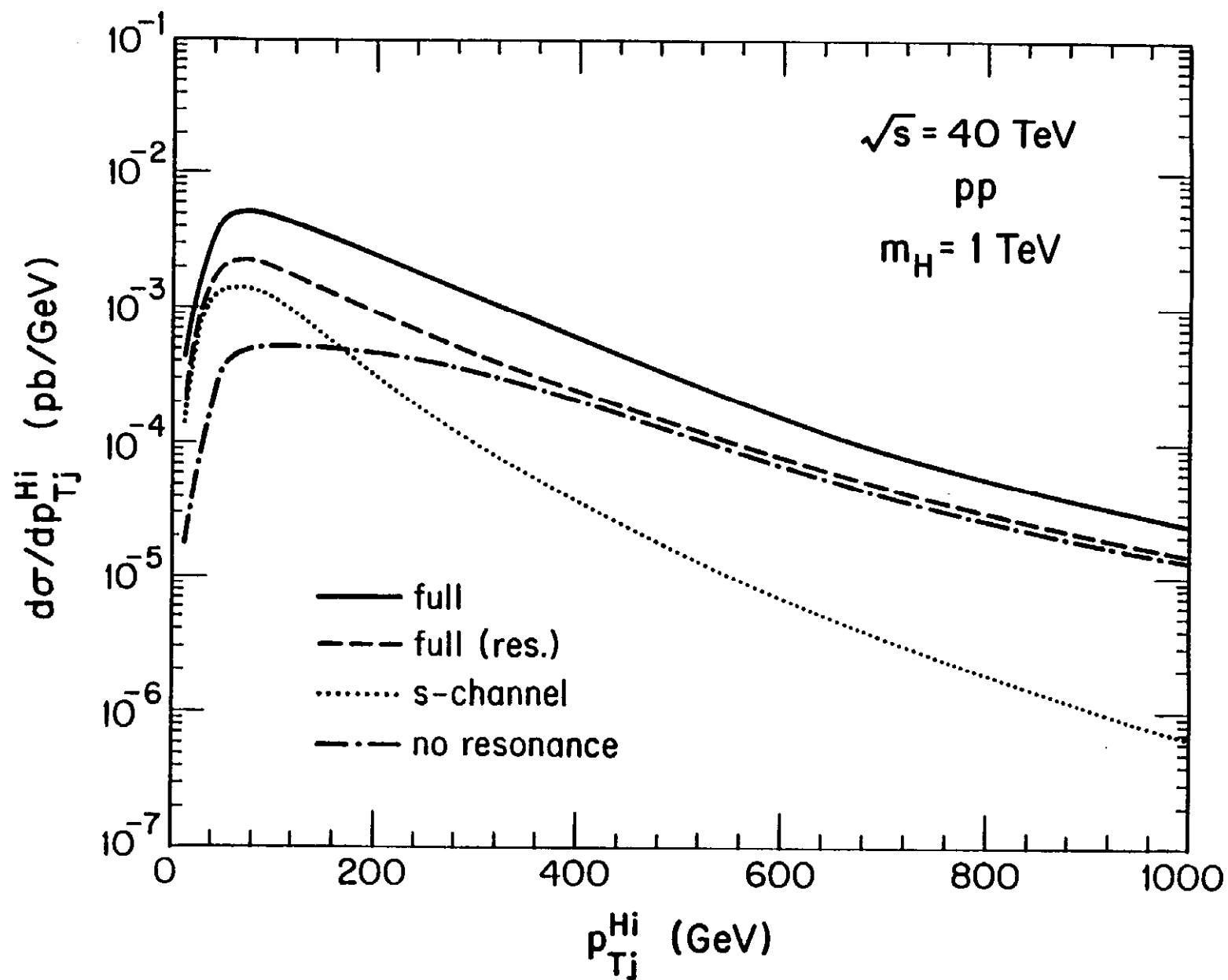


Fig. 11a

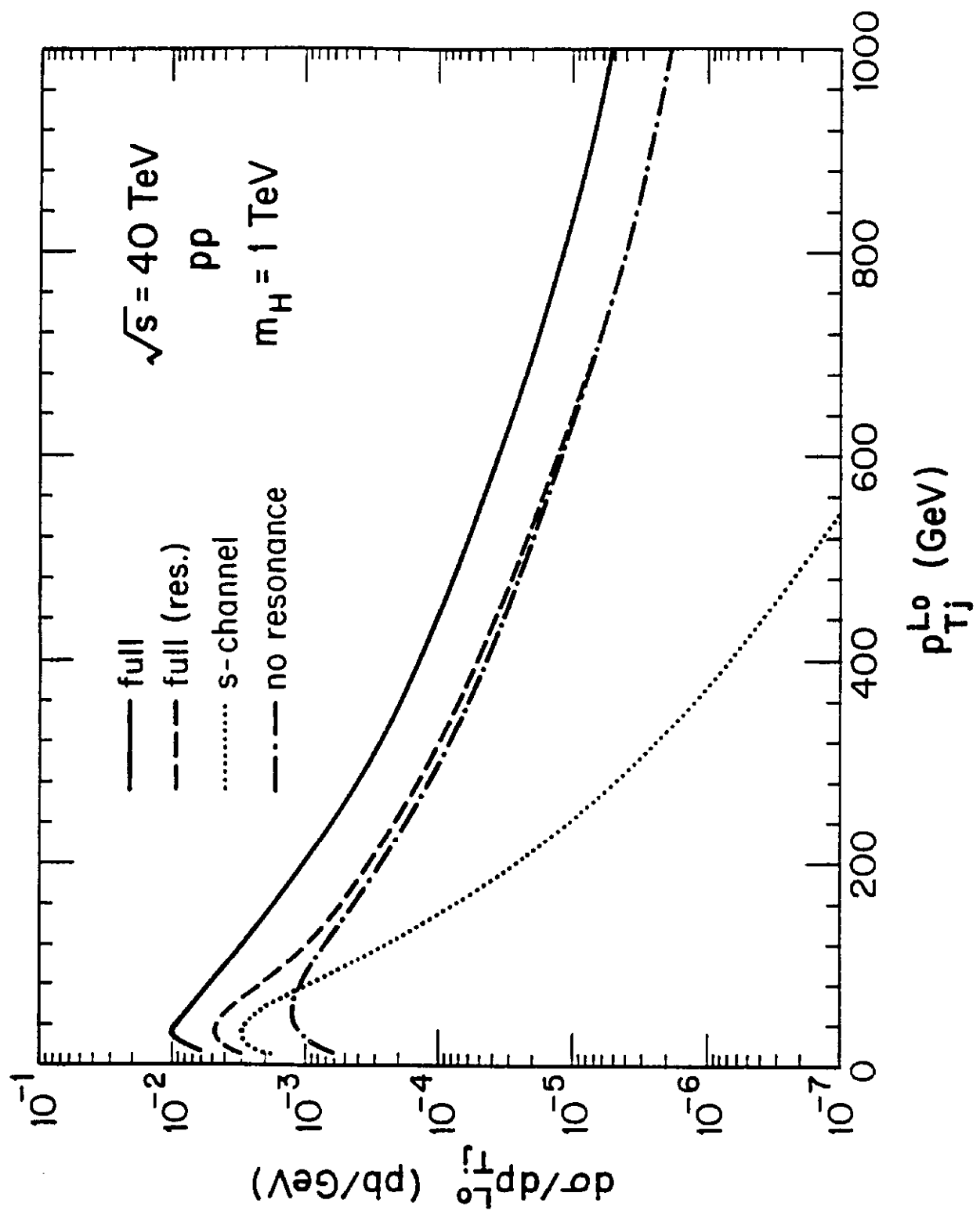


Fig. 11b

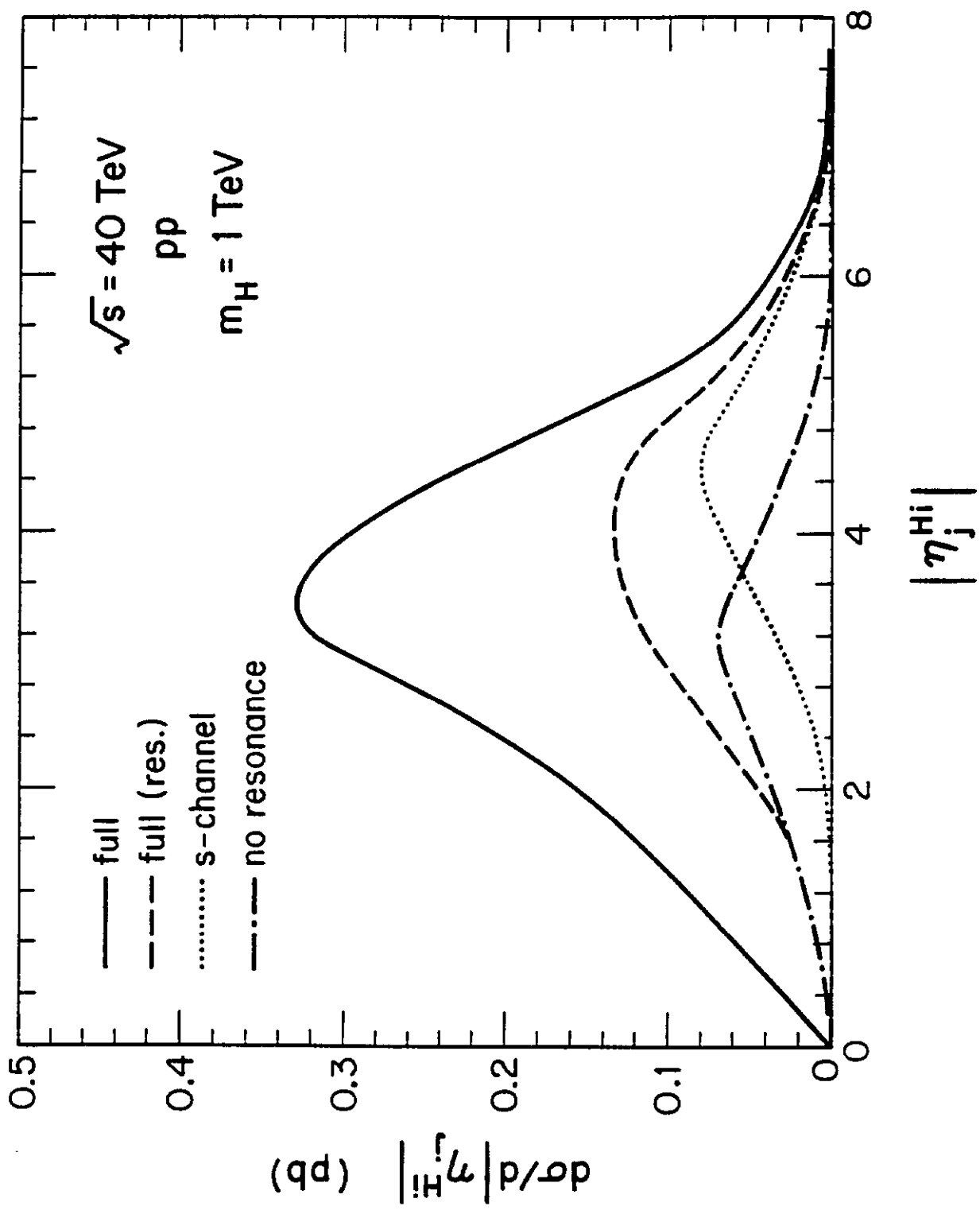


Fig. 12a

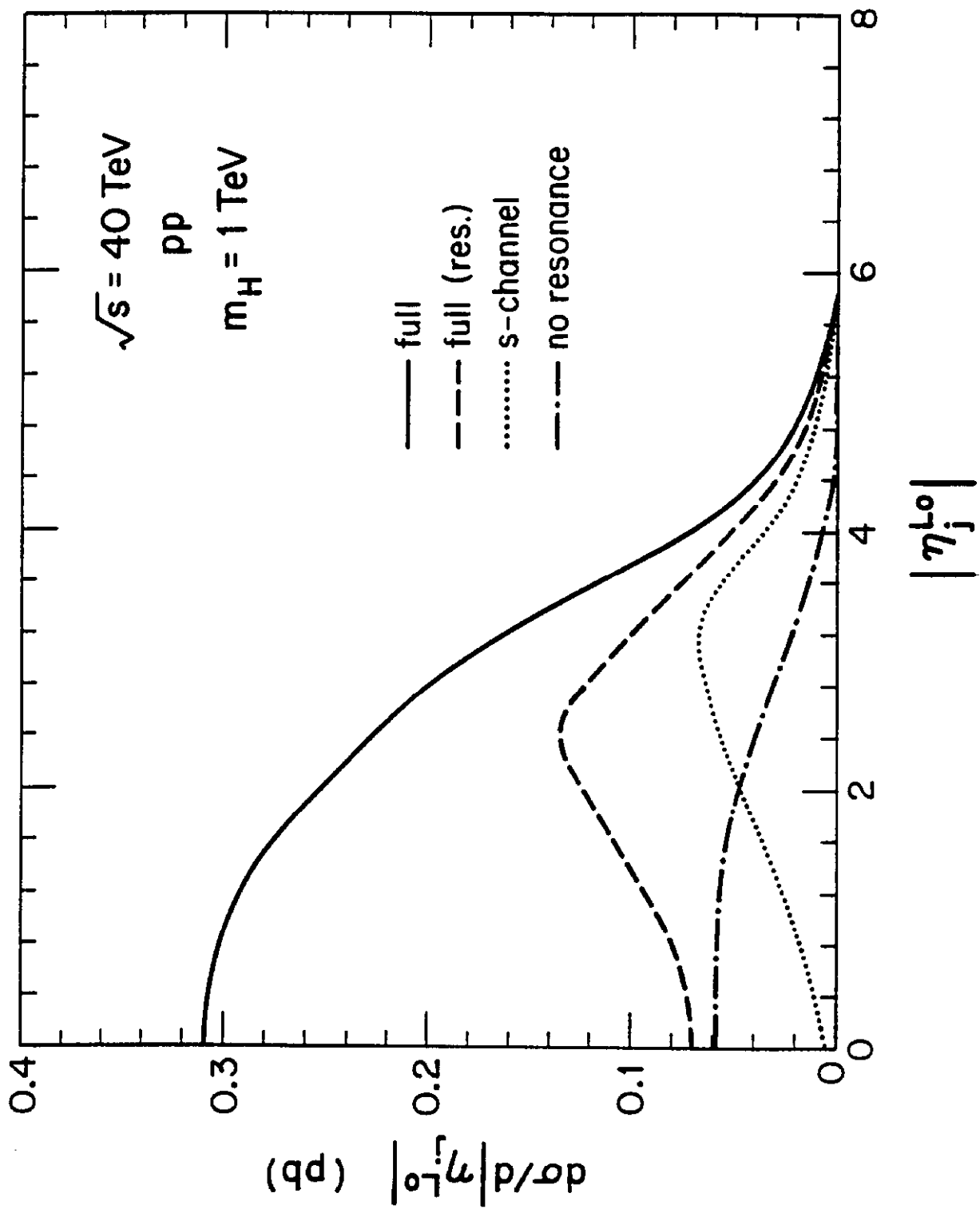


Fig. 12b

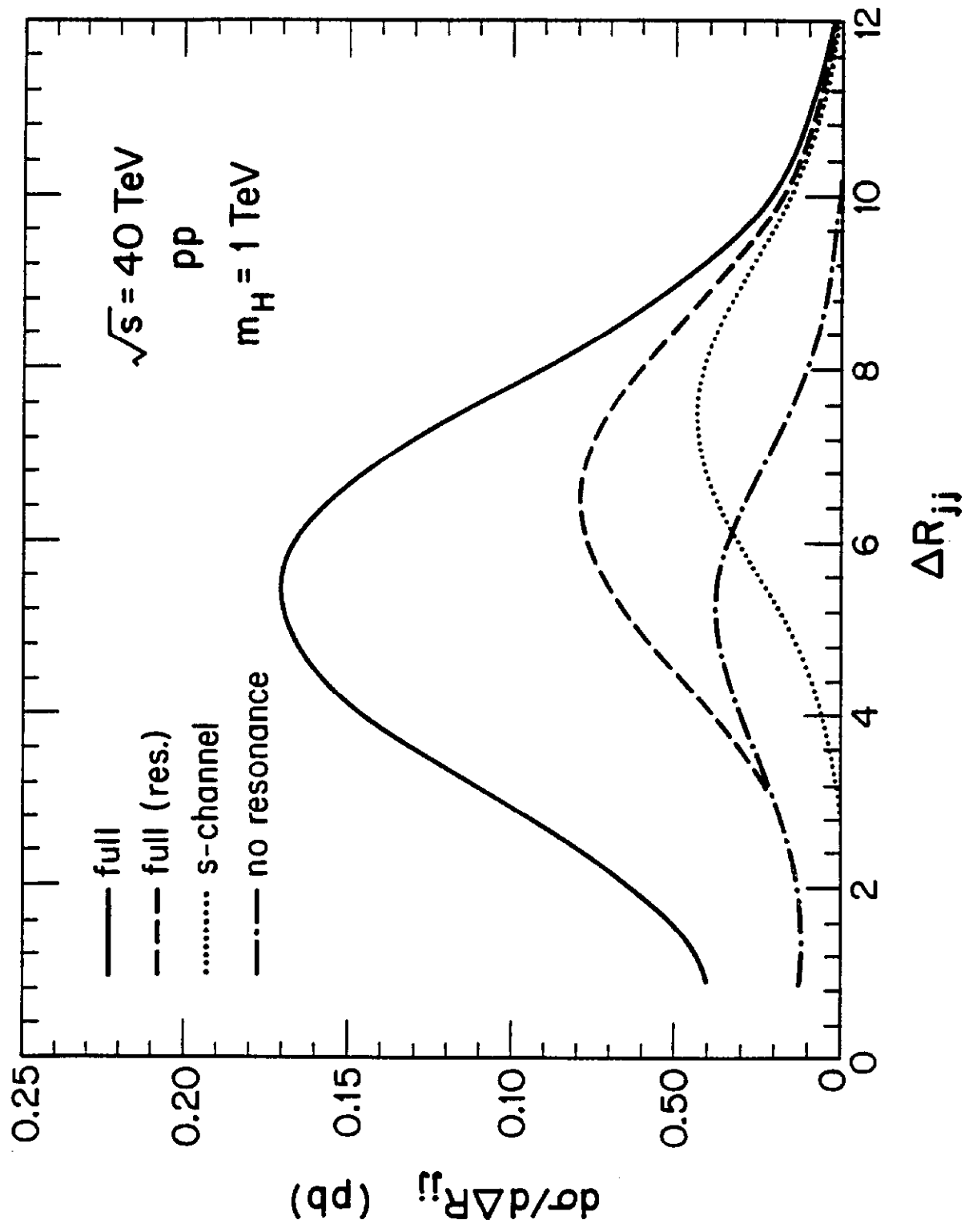


Fig. 13

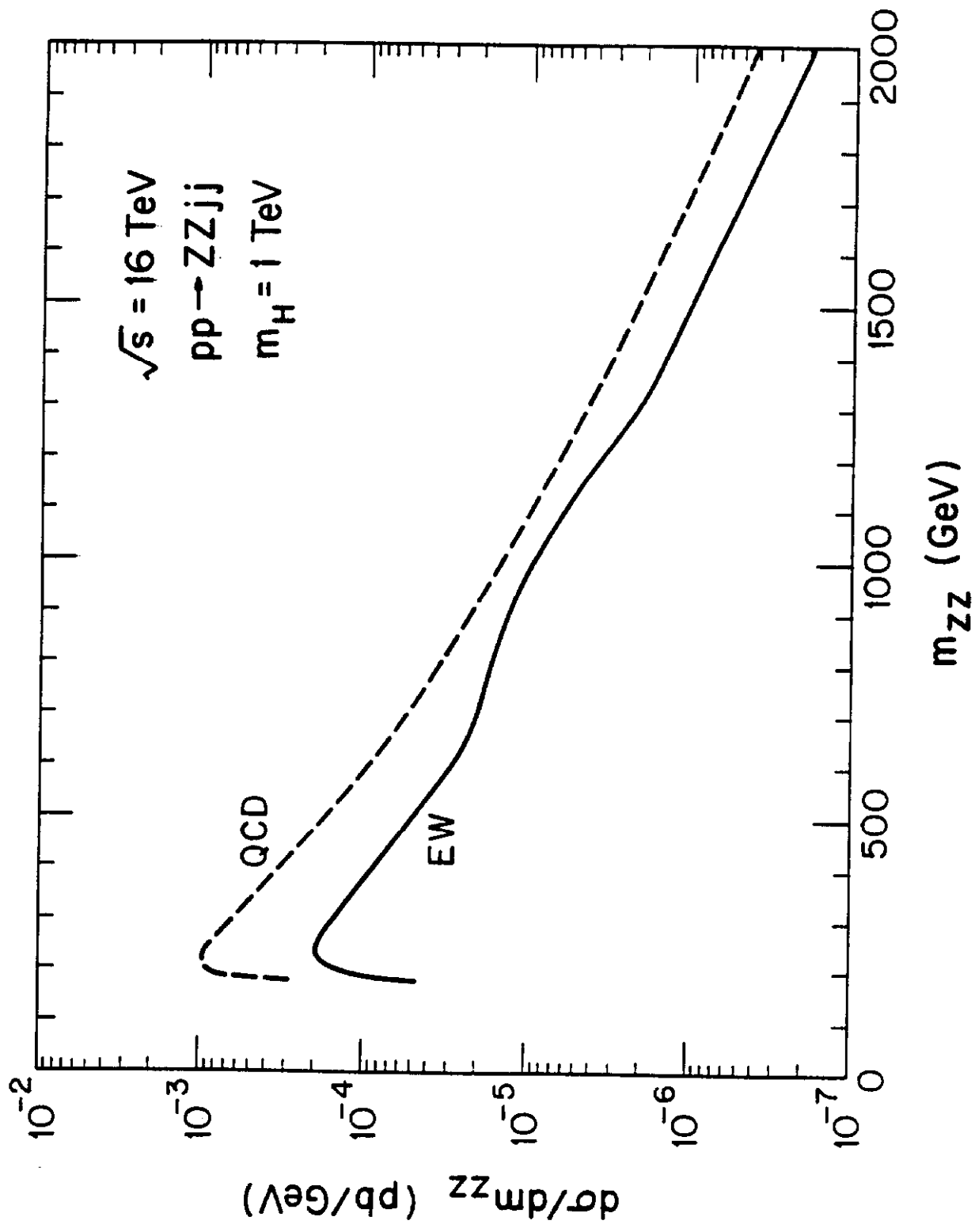


Fig. 14a

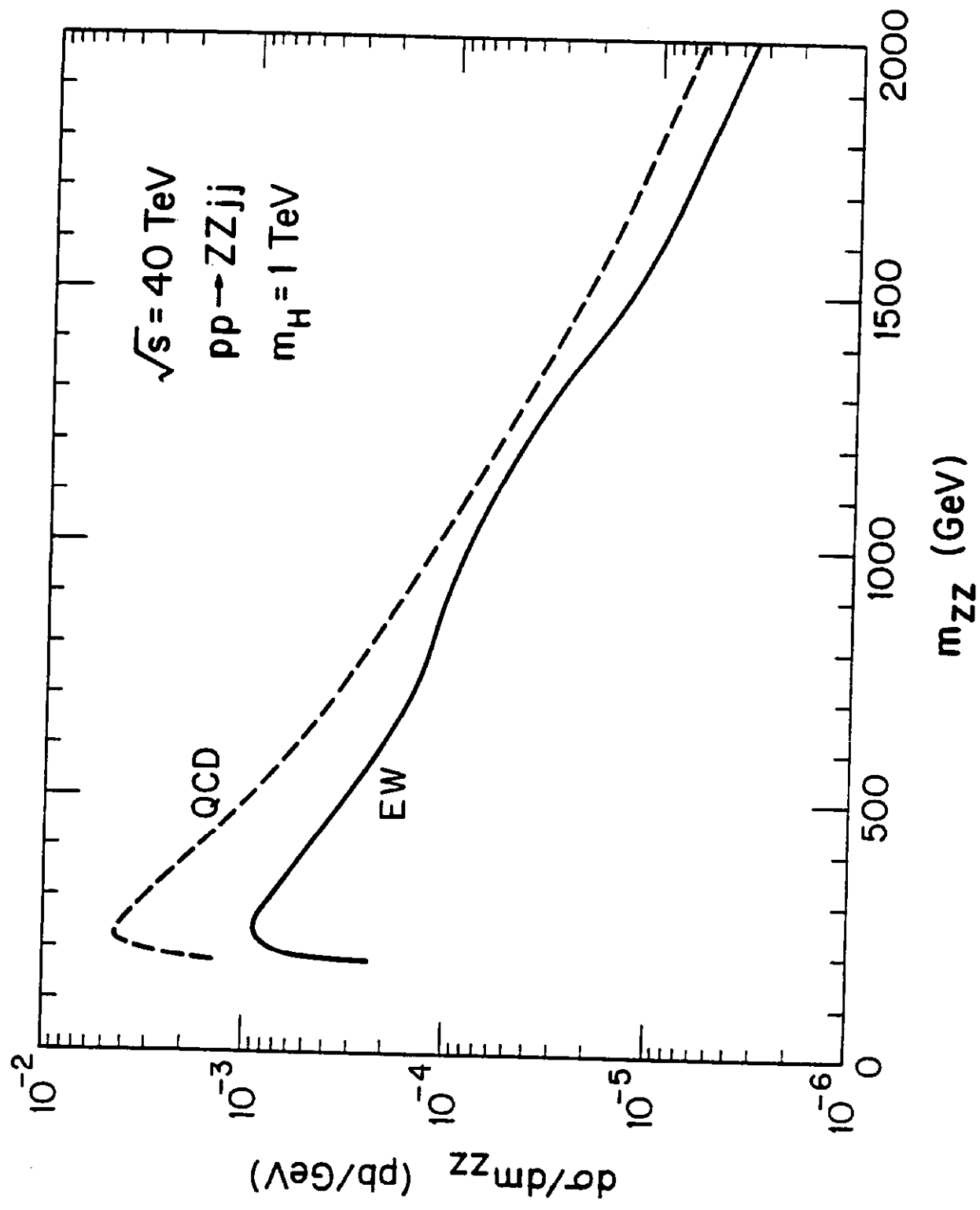


Fig. 14b

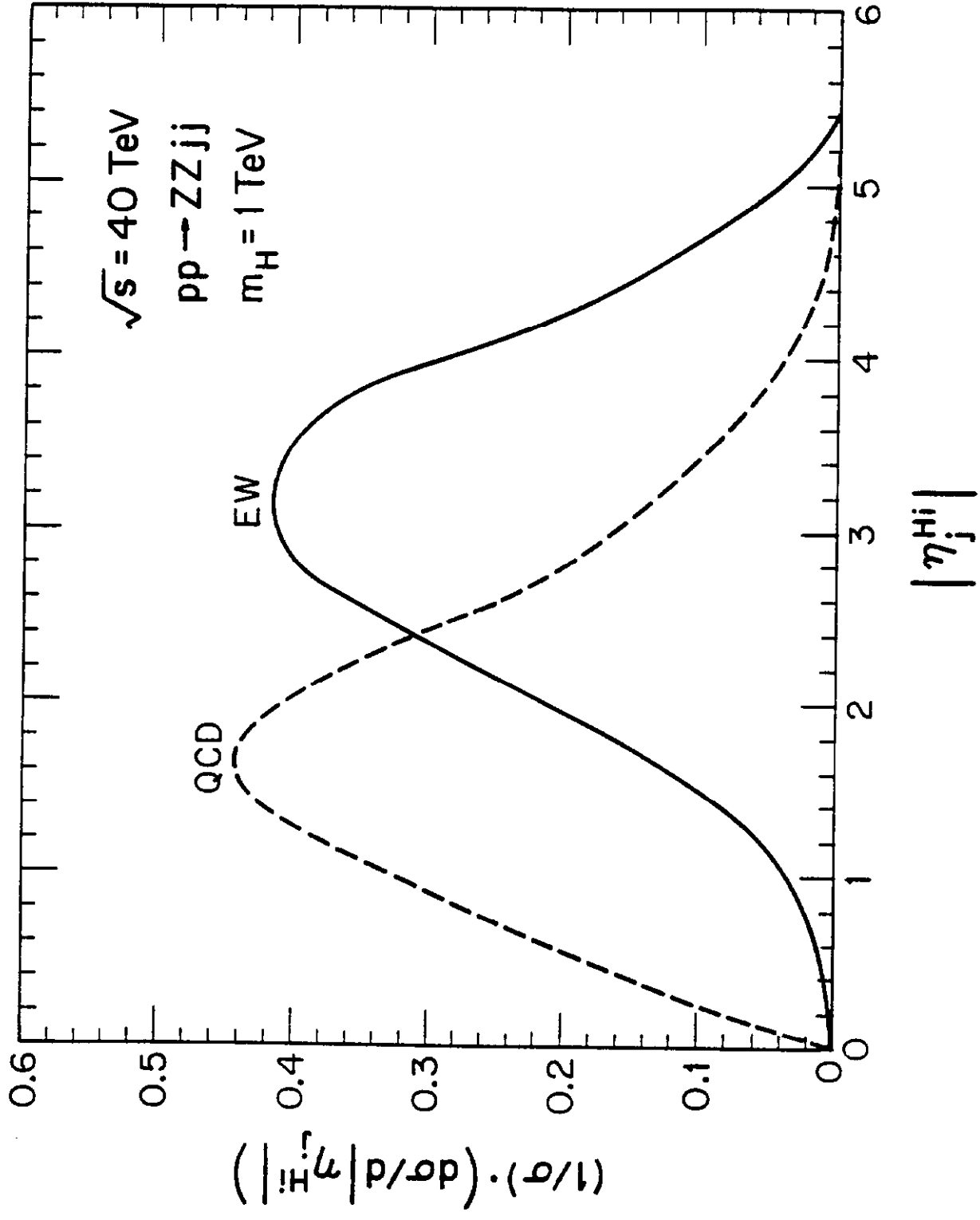


Fig. 15a

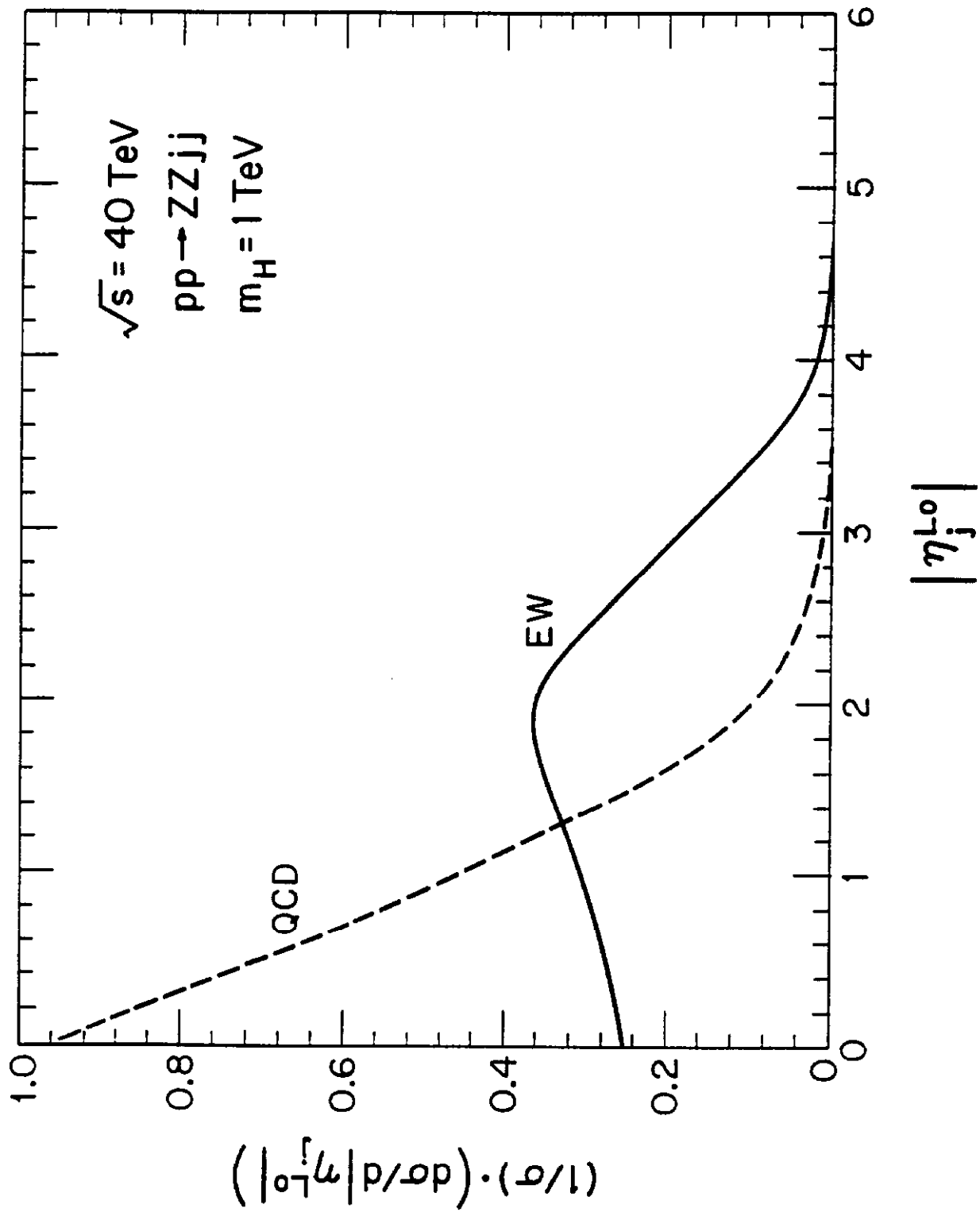


Fig. 15b

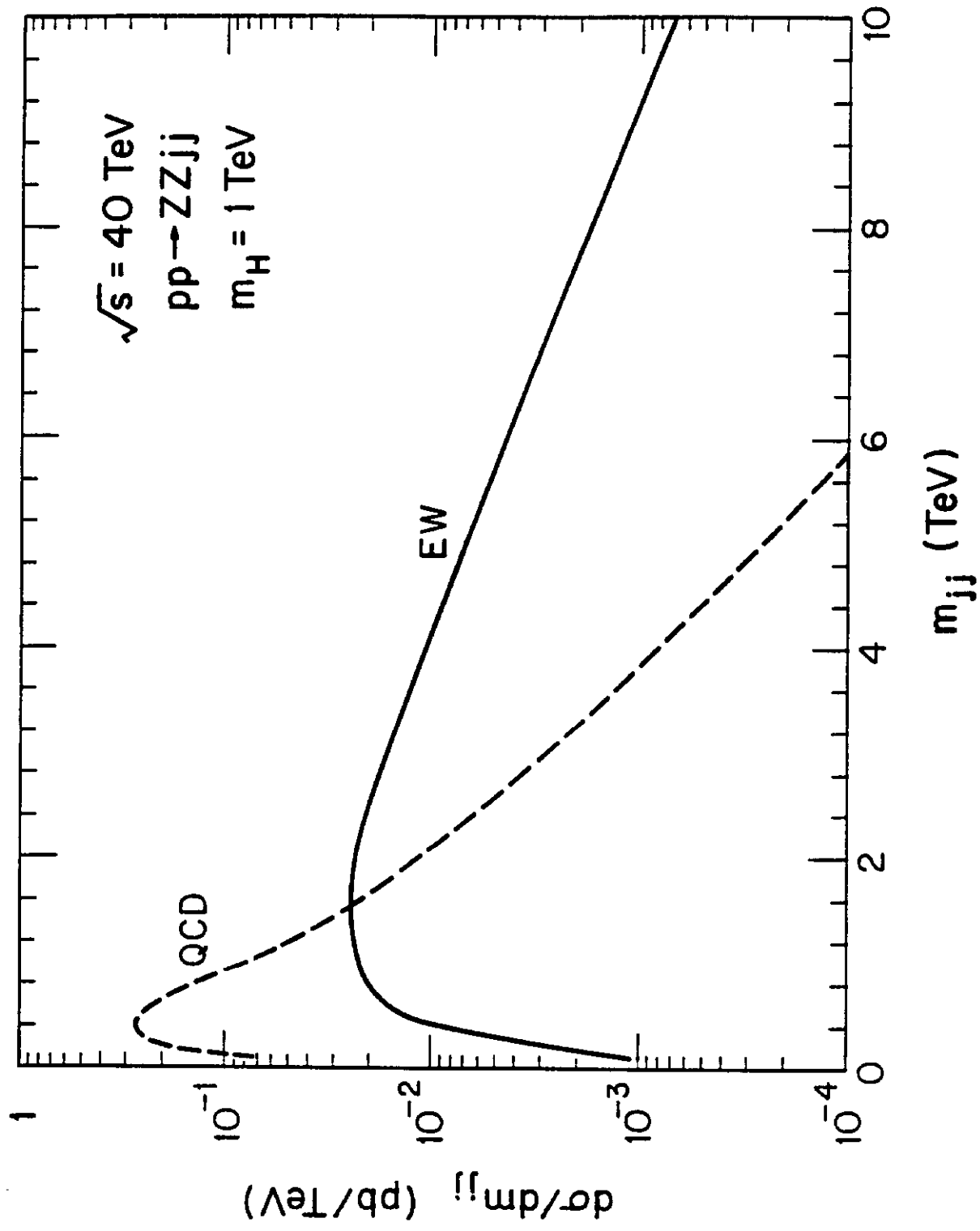


Fig. 16

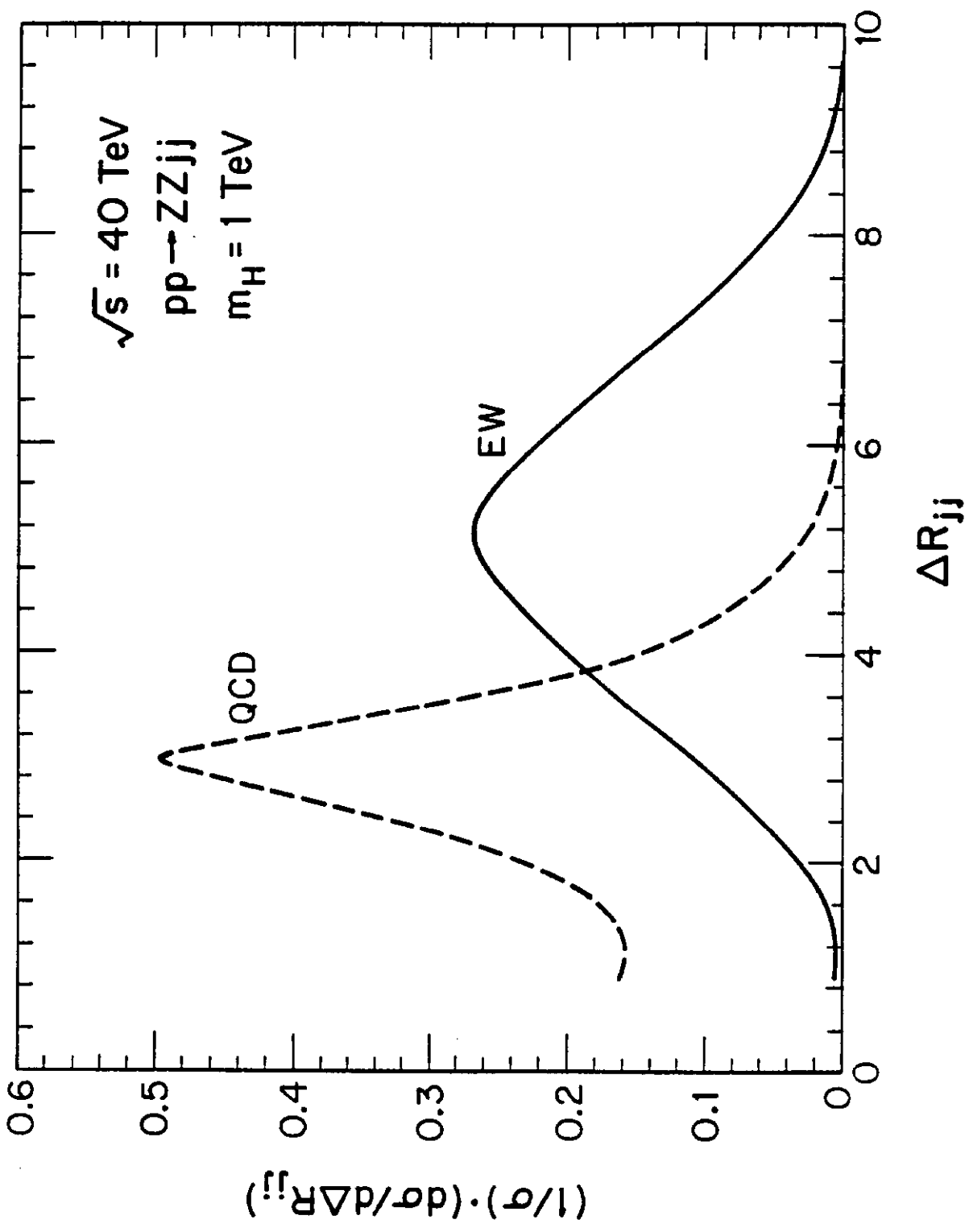


Fig. 17